Markus Hirber, BSc

Modification of Nanoporous Gold with Self-Assembled-Monolayers Intended for Enzyme Immobilization: Electrochemical Analysis of Point of Zero Charge and Protonation

MASTER'S THESIS

to achieve the university degree of

Diplom-Ingenieur

Master's degree programme: Technical Physics

submitted to

Graz University of Technology

Supervisor

Univ.-Prof. Dipl.-Phys. Dr.rer.nat. Roland Würschum

Co-Supervisor

Dipl.-Ing. Dr.techn. Eva-Maria Steyskal

Institute of Materials Physics

Graz, August 2020

Affidavit

I declare that I have authored this thesis independently, that I have not used other than the declared sources/resources, and that I have explicitly marked all material which has been quoted either literally or by content from the used sources. The text document uploaded to TUGRAZonline is identical to the present master's thesis.

Date

Signature

Abstract

The interest in nanoporous gold (npAu) as a conducting substrate for enzyme immobilization has grown strongly in the last decade. Self-assembled monolayers (SAMs), a monolayer of atoms or molecules that forms spontaneously from solution or vapor phase on a substrate, can be used to modify the surface of npAu leading to an improved stability of the enzymes. In this master's thesis, the influence of SAMs on the electrochemical properties of npAu is investigated. Special focus lies on the control of the surface charge of the sample which can be used in further research to electrostatically bind and orient enzymes containing a polar group. To investigate the differences arising from different chain lengths and functionalized groups, the long-chained 16-mercaptohexadecanoic acid (MHDA) and the short chained 3-mercaptopropionic acid (MPA), both functionalized with a carboxyl group, and sodium 2-mercaptoethanesulfonate (MESA) functionalized with a sulfonic acid group were used to create the SAMs.

For untreated npAu and npAu modified with different SAMs the point of zero charge (PZC) was determined in 10 mM $HClO_4$ via the capacitance in the double layer regime. The capacitance was obtained by electrochemical impedance spectroscopy (EIS). The PZC of untreated npAu could not be determined due to its heterogeneous surface structure with a high number of surface defects. For npAu modified with MPA a potential regime with lower capacitance was observed around +150 mV to +250 mV and for npAu modified with MESA around +500 mV. For npAu modified with MHDA a minimum was found at +100 mV. The more anodic PZC of npAu modified with MESA is caused by the higher dipole moment due to the deprotonation of the sulfonic acid group. To further improve the control of the surface charge, the protonation/deprotonation reaction of the carboxyl groups of MHDA and MPA was investigated with cyclic voltammetry (CV) at different pH values. Peaks corresponding to the protonation and the deprotonation reaction could be observed on npAu modified with MHDA. The protonation peak was inspected in more detail. It shifted towards more cathodic potentials with increasing pH and it was highest at a pH of 8.6. Much larger protonation and deprotonation peaks with less separation between them were observed for MPA. Fast desorption of MPA inhibited the determination of the influence of pH on the reaction. The protonation/deprotonation reaction of MDHA was further investigated with EIS which confirmed the results of the CVs.

Kurzfassung

Das Interesse an nanoporösem Gold (npAu) als leitendem Substrat für Enzymimmobilisierung hat im letzten Jahrzehnt stark zugenommen. Selbstorganisierte Monoschichten (SAMs), Monoschichten aus Atomen oder Molekülen, die sich spontan aus der Lösungs- oder Dampfphase auf einem Substrat bilden, können verwendet werden, um die Oberfläche von npAu zu modifizieren. Das führt zu einer verbesserten Stabilität der Enzyme. In dieser Masterarbeit wird der Einfluss von SAMs auf die elektrochemischen Eigenschaften von npAu untersucht. Der Schwerpunkt liegt auf der Kontrolle der Oberflächenladung der Probe, um diese in weiterführender Forschung zur elektrostatischen Bindung und Orientierung von Enzymen mit einer polaren Gruppe verwenden zu können. Um die Unterschiede zu untersuchen, die sich aus unterschiedlichen Kettenlängen der SAM-Moleküle ergeben, wurden die langkettige 16-Mercaptohexadecansäure (MHDA) und die kurzkettige 3-Mercaptopropionsäure (MPA) verwendet, um SAMs zu erzeugen. Beide sind mit einer Carboxylgruppe funktionalisiert. Zusätzlich wurde Natrium-2-mercaptoethansulfonat (MESA) verwendet, welches mit einer Sulfonsäuregruppe funktionalisiert ist, um den Einfluss der unterschiedlichen funktionellen Gruppen zu untersuchen.

Für unbehandeltes npAu und npAu, das mit unterschiedlichen SAMs modifiziert wurde, wurde der "Point of Zero Charge" (PZC) in 10 mM $HClO_4$ über die Kapazität im Doppelschichtbereich bestimmt. Die Kapazität wurde mit elektrochemischer Impedanzspektroskopie (EIS) gemessen. Der PZC von unbehandeltem npAu konnte aufgrund der heterogenen Oberflächenstruktur mit einer hohen Anzahl von Oberflächendefekten nicht bestimmt werden. Für mit MPA-SAM modifiziertes npAu wurde ein Potenzialbereich mit niedrigerer Kapazität um +150 mV bis +250 mV beobachtet. Für mit MESA-SAM modifiziertes npAu war die Kapazität bei Potenzialen um +500 mV am geringsten. Ein Minimum konnte für mit MHDA-SAM modifiziertes npAu bei +100 mV gefunden werden. Die stärker anodische Lage des PZC von mit MESA-SAM modifiziertem npAu wird durch das höhere Dipolmoment verursacht, das von der Deprotonierung der Sulfonsäuregruppe erzeugt wird. Um die Kontrolle der Oberflächenladung weiter zu verbessern, wurde die Protonierungs-/Deprotonierungsreaktion der Carboxylgruppen von MHDA und MPA mit Zyclovoltammetrie bei verschiedenen pH-Werten untersucht. Peaks, die der Protonierungs- und der Deprotonierungsreaktion entsprechen, konnten für mit MHDA-SAM modifiziertes npAu beobachtet werden. Der Protonierungspeak wurde genauer untersucht. Er verschob sich mit zunehmendem pH-Wert zu kathodischeren Potentialen und war bei einem pH-Wert von 8.6 am stärksten. Für MPA wurden deutlich größere Protonierungs- und Deprotonierungspeaks mit geringerem Abstand zwischen ihnen beobachtet. Die schnelle Desorption von MPA verhinderte die Bestimmung des Einflusses des pH auf die Reaktion. Die Protonierungs-/Deprotonierungsreaktion von MHDA wurde mit EIS weiter untersucht, was die Ergebnisse der Zyclovoltammetrie bestätigte.

Contents

1 Introduction

In bioelectrochemistry, immobilization of enzymes on a conducting substrate is needed for many applications including biofuel cells[1] and biosensors[2]. Immobilization can be achieved by physisorption, entrapment, or a covalent bond. Nanoporous gold (npAu), a porous gold structure with pore sizes in the nanometer regime, is a very promising conducting substrate material due to its capability of entrapment and physisorption of enzymes. Self-assembled monolayers (SAMs), a monolayer of atoms or molecules that forms spontaneously from solution or vapor phase on a substrate, can be used on the surface of npAu to improve immobilization and orientation of the enzymes and to enable charge transfer between the Au surface and the enzymes without decreasing the physiological activity of the enzymes[3].

In the last few decades, various organic molecules on flat metal surfaces have been extensively studied as SAMs due to their ability of modifying the surface properties of the metal[4]. One part of the molecules must create a strong bond to the metal substrate to build a monolayer. The newly created surface can be modified with different functional groups depending on the application. Relating to enzyme immobilization, SAMs functionalized with a carboxyl group have been used on planar surfaces. Depending on the pH of the surrounding medium (electrolyte) a fraction of the carboxyl groups is in the deprotonated state (a H^+ ion has dissociated from the carboxyl group) and the surface is negatively charged. This can be used to electrostatically bind enzymes to the surface[5]. The degree of dissociation of the carboxyl groups and with it the strength of the bond can be adjusted by changing the pH and immobilization can be switched on and off.

Considerably less research has been done on the behavior of SAMs on porous metal substrates. It is, however, a very promising system for biochemical applications and has several advantages compared to flat Au surfaces. The high surface-to-volume ratio leads to a high density of functionalized SAM molecules in a small volume and the nanostructured surface of npAu creates a more stable bond between the SAM and the Au surface[6]. Additionally, enzymes can be geometrically entrapped in npAu and electrostatically bound to the SAM which leads to improved binding and stability[1]. Covalently immobilizing enzymes is also possible with SAMs. For certain sensor applications it can be useful that the pore size of npAu can be adjusted by thermal or electrochemical treatments[7] which can be used to keep large molecules out of the system while small molecules can enter and be detected[3].

In this thesis the influence of modification of npAu with different SAMs on the electrochemical properties is analyzed. Two SAMs of different length functionalized with carboxylic acid (COOH) and one SAM functionalized with sulfonic acid (SO_2OH) are used. Controlling the charge at the surface of the samples is an important aspect for enzyme immobilization. Therefore, first the point of zero charge of the different samples is determined. That is the applied potential at which no excess charge accumulates at the interface between the sample and an electrolyte. Then, the deprotonation and protonation of the carboxylic acid is investigated by varying the applied potential at different pH values to gain insight in the behavior of the carboxylic acid in different environments. This is done in view of the aim of influencing the surface charge by controlling the state of the carboxylic acid with an externally applied potential for further applications in enzyme immobilization.

Cyclic voltammetry (CV) and electrochemical impedance spectroscopy (EIS) are used for the characterization of the samples. The former is a well-known technique at the Institute of Material Physics whereas the latter was only recently implemented at the institute in a master thesis written by Philipp Brunner where the properties of nanoporous gold and palladium were analyzed. EIS measurements have not been performed on nanoporous samples modified with SAMs at the institute previously to the present work. Analysis of SAMs on nanoporous samples is more complicated than on planar samples due the influence of the very irregular surface of the nanoporous sample and slow diffusion of the electrolyte in the pores especially when modified with long SAMs. Therefore, measurements have to be conducted slower than on planar samples. The present thesis is conducted in the framework of the lead project “Porous Materials @ Work“.

2 Fundamentals

2.1 Self-Assembled Monolayers

In the last few decades, the modification of surfaces with Self-Assembled Monolayers (SAMs) has been extensively studied[4]. SAMs are a very promising tool in surface science because they can be easily prepared and used in many different fields. They are the simplest form of a self-assembled system and consist of atoms or molecules adsorbed on a solid surface. The arrangement of the atoms or molecules forms spontaneously from solution or vapor phase[8]. Applications range from electrochemical sensors[9], modulation of the work function of metals[10] [11], corrosion inhibition[12], building blocks for biomolecule carriers and many others[8].

Molecules used for the formation of SAMs usually consist of three different parts: The head, the backbone and the specific terminal group[8]. The head group is responsible for the connection of the molecules to the substrate. A strong bond between the substrate and head group of the molecule in solution or vapor phase must be created to form a SAM. The head group must therefore have high affinity for the substrate. A very well studied combination of head group and substrate is the binding of thiols on gold[13]. The backbone consists of hydrocarbon chains which interact through van der Waals and hydrophobic forces which get stronger for longer chains[8]. These interactions are important for the stabilization of the structure and dense packing. The terminal group is the part of the SAM which forms the new surface of the sample. Different chemical structures of the terminal group can be used to change the properties of the surface for example from hydrophobic to hydrophilic or to form a bond with a different molecule. With this, it is possible to use the bonds at the head group and the terminal group of a SAM for the connection of metals or semiconductors to organic molecules[8].

The formation of SAMs consisting of thiol molecules on a metal substrate can occur from a solution or gas phase and consists of several steps, which are schematically

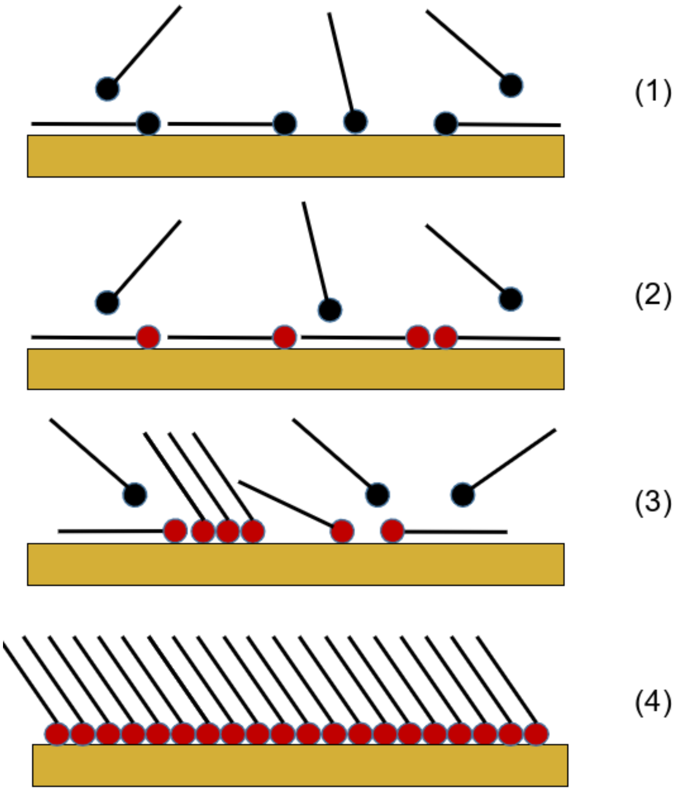

Figure 2.1: Formation of a SAM from molecules in solution: Unbound and physisorbed head groups are shown as black circles and chemisorbed head groups as red circles: (1) beginning of physisorption, (2) chemisorption in lying down phase, (3) nucleation of standing up phase, (4) SAM in standing up phase, redrawn after[8].

shown in figure 2.1. Deposition from liquid environments is more common due to its simplicity. Thiols on Au will be used as an example system in this paragraph because it is very commonly studied and is also used in our experiments. At the beginning of the adsorption process the molecules reach a physisorbed state on the metal followed by chemisorption through the formation of a covalent bond between the sulfur headgroup and the metal. These processes can be described for alkanethiol molecules by[8]:

$$\mathrm{RSH} + \mathrm{Au} \longrightarrow (\mathrm{RSH})_{\mathrm{phys}}\mathrm{Au}, \tag{2.1}$$

$$(\mathrm{RSH})_{\mathrm{phys}}\mathrm{Au} \longrightarrow \mathrm{RS{-}Au} + \frac{1}{2}\,\mathrm{H}_2. \tag{2.2}$$

The H-atom created in this reaction can either form a H_2-molecule with the H-atom of the chemisorption process of another thiol or adsorb on the metal surface[14]. At the beginning the chemisorbed molecules are in the lying down phase where the backbone is parallel to the surface of the metal. At longer adsorption times the nucleation of the standing up phase begins. The standing up phase is favorable at higher coverages due the Van der Waals interactions between the backbones of neighboring adsorbed molecules and the increase of thiolate bonds. The result is a closely packed SAM of alkanethiols. The surface coverage in this phase on a flat metal surface is $\Theta \approx 1/3$ and can be up $\Theta \approx 2/3$ on gold nanoparticles. The duration of this process depends on the length of the hydrocarbon backbone and ranges from hours to days.[8]

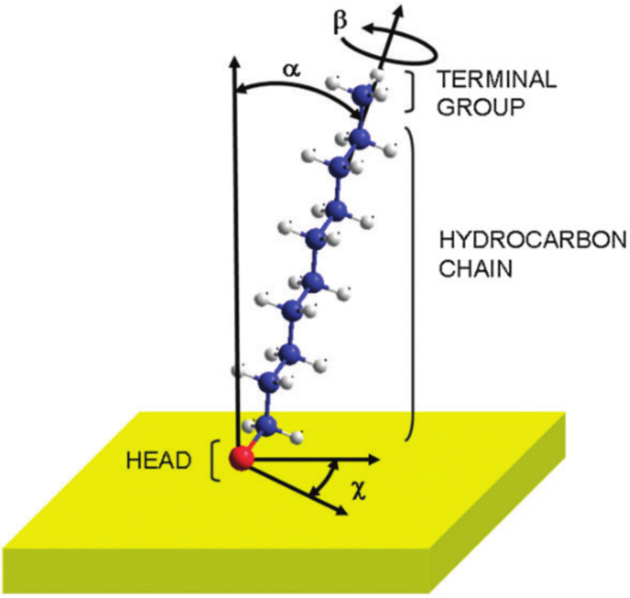

Figure 2.2: Decanethiol adsorbed on Au(111) in the standing-up phase: tilt angle α, twist angle β and angle of precession χ. Reprinted with permission from[8]. Copyright 2010 The Royal Society of Chemistry.

The orientation of the molecules in the SAM relative to the metal substrate depends on the Van der Waals interactions between the backbones and the molecule-metal interactions. The three angles shown in figure 2.2 are used to describe the orientation: The tilt angle α between the backbone and the surface normal of the metal, the twist angle β which gives the rotation of the axis of the molecule and the precession angle χ of the projection of the molecule on the substrate. For molecules with long backbones α is small (0-37°), whereas for short molecules the interaction between molecules and substrate are more important and the angle increases further.[14]

The stability of the SAM depends on the molecules that build the SAM and the surface of the metal. Increasing the length of the hydrocarbon backbone leads to more stable SAMs due to the increase in Van der Waals interactions between neighboring SAM molecules by approximately 0.1 eV per additional C-atom[14]. The binding energy of the covalent S-Au bond depends on the surface orientation and the electronic states of Au. It is in the range of 2 eV and it is about 0.4 eV higher on nanostructured surfaces compared to flat Au(111)[6]. Surface reconstruction of the Au surface can be induced by the formation of the SAM which also influences the surface energy. Additionally, defects on the surface of Au such as steps and adatoms increase the stability of the SAM[15].

Degradation of SAMs can occur due to chemical or thermal influences or when a potential is applied to the metal substrate. Thermal and chemical desorption processes can be described by[8]:

$$2\,\mathrm{RS} - \mathrm{Au} \longrightarrow \mathrm{RSSR} + 2\,\mathrm{Au}, \tag{2.3}$$

$$\mathrm{RS} - \mathrm{Au} + \mathrm{H_2O} + \mathrm{O_3} \longrightarrow \mathrm{RSO_3H} + \mathrm{HO{-}Au}. \tag{2.4}$$

Reaction 2.3 can occur in liquid environments and at high temperatures and leads to the creation of disulfides. During reaction 2.4 sulfonates are created which can happen in liquid or ambient environments. Disulfides and sulfonates are not adsorbed on the Au surface. Again, longer backbones of the molecules lead to more stable SAMs and SAMs on nanostructured surfaces are more stable due to the surface defects. Significant degradation was measured for thiols on flat Au surfaces during storage for two weeks at ambient conditions or in ethanol, whereas almost no degradation was observed when the SAM was formed on a nanostructured surface[8]. When a negative potential is applied reductive desorption can occur according to:

$$\mathrm{RS} - \mathrm{Au} + \mathrm{e^-} \longrightarrow \mathrm{RS^-} + \mathrm{Au}. \tag{2.5}$$

Reductive desorption can be used to estimate the amount of thiol adsorbed on Au and to compare the stability of different SAMs by comparing the potential at which they desorb.[8]

Even without degradation there can be different kinds of defects present in well-ordered SAMs which can have strong influence on some applications. Steps on the surface of the Au sample can still be visible when the surface is covered with SAMs which causes some disorder in the SAMs (top of figure 2.3). Pinholes appear in SAMs when some molecules are missing (bottom of figure 2.3). They are much more likely on short SAMs whereas long molecules form closely packed SAMs[16]. For short alkanethiols it is also possible that rows of molecules are missing[8]. Similar defects are formed when the hydrocarbon chains of some molecules are not fully extended. Another source of defects are domain boundaries (middle of figure 2.3). Within a single domain all molecules have the same orientation and packing but at boundaries between domains of different Au surface structures there are defective regions. Domain boundaries can also appear on terraces with only one Au surface orientation when the distance between nucleation centers is smaller than the terrace and different symmetry-equivalent orientations are possible on the substrate. Domains with different precession angle χ can then grow and create domain boundaries. Defects generally improve the charge transfer across the SAM because there is a direct pathway for an electrolyte or metal deposit through the SAM.[8]

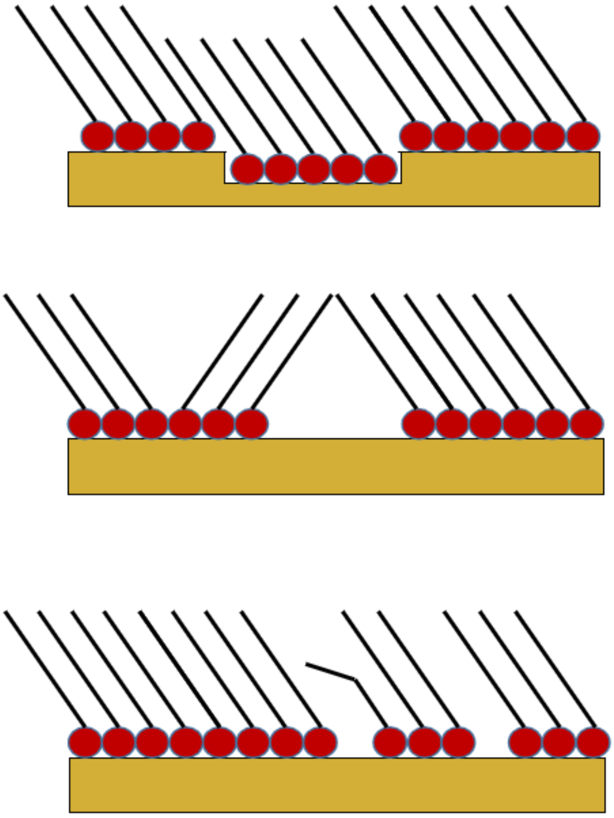

Figure 2.3: Schematic representation of the defects in a SAM consisting of a sulfur head group (red) and a backbone (black) on a gold surface, redrawn after[8].

Modifying the terminal group of SAMs with a functional group can strongly influence the properties of the sample. This creates a lot of possible applications in different fields. Examples for functional groups are methyl groups ($-CH_3$), trifluoromethyl groups ($-CF_3$), carboxyl groups ($-COOH$), amino groups ($-NH_2$), and hydroxyl groups

(−OH) but many others can also be used. $-CH_3$ and $-CF_3$ create a hydrophobic and anti-adherent surface, whereas −COOH, $-NH_2$, −OH make the surface hydrophilic and suitable to bind metals or proteins[8]. −COOH can be used to immobilize enzymes on a metallic substrate to create a biosensor[17]. Changing the pH or applying a potential influences the amount of hydrogen dissociated from the −COOH groups which enables the control of the surface charge of the samples. Modifying the surface charge influences the interactions of the sample with charged molecules[18]. This effect can, for example, be applied to detect dopamine in the presence of ascorbic acid due to the different charge distributions on the molecules[9].

2.2 Nanoporous Gold

Nanoporous gold (npAu) has a very high surface-to-mass and surface-to-volume ratio which is important in many areas of applications. NpAu has good catalytic properties for the oxidation of CO[19] and selectively oxidizing methanol to methyl[20]. It can also be used as an actuator[21] or sensor[22], because the surface chemistry influences the surface stress. Due to the high surface area this leads to macroscopic strain effects of the sample[20]. Another field of application is biosensing, where npAu is used as a carrier for enzymes which can detect specific molecules[23] [24].

NpAu can easily be generated by electrochemical dealloying of an alloy consisting of Au and a less noble metal. Ag and Cu are commonly used as the less noble component to create the alloy. An AgAu alloy will be used as an example in this paragraph and it is also the alloy used in the present work. Dealloying is done by immersing the alloy in an electrolyte and applying a potential above a critical potential V_C which depends on the composition of the alloy and the electrolyte. Above V_C the Ag atoms are removed from the alloy at less stable sites like steps and edges and Au atoms diffuse to passivate these sites. Then the Ag atoms dissolve from the more stable terraces and vacancies are created (figure 2.4a). The Au atoms remaining as adatoms on the alloy diffuse to high-concentration areas and expose the underlying less noble atoms to the electrolyte and dealloying continues (figure 2.4b). Pores and ligaments are formed as more Ag dissolves. Below V_C a full layer of Au atoms is formed which leads to passivation of the surface and stops the dealloying process. A certain concentration X_P of Ag must be present in the initial alloy so that the Ag atoms are connected. Otherwise dealloying is stopped without dissolving most of the Ag due to passivation with Au. The threshold is about 60 at% Ag.[7]

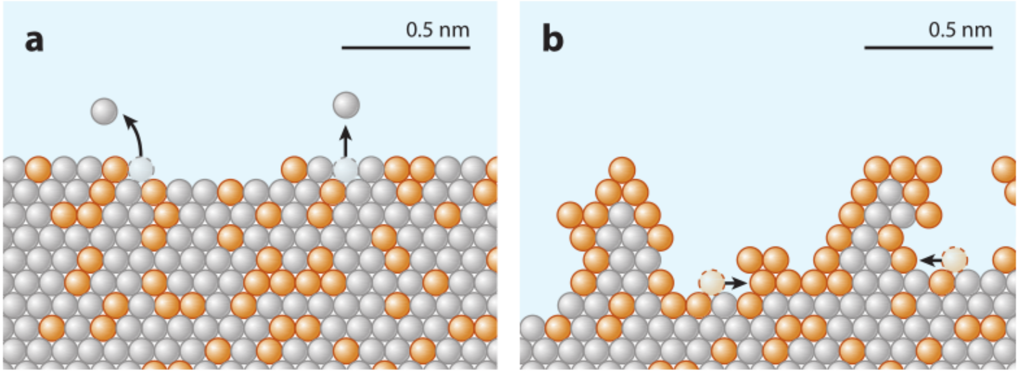

Figure 2.4: Schematic representation of the dealloying process. Reprinted with permission from[7]. Copyright 2016 Annual Reviews.

Surface area, pore diameter and ligament size are important properties of npAu. They depend on the alloy and the paramters during dealloying such as potential, temperature and electrolyte. For npAu dealloyed from an 75at%Ag-25at%Au alloy in $HClO_4$, as used in this work, a pore diameter between 10 and 20 nm is reported in literature[25]. The ligament and pore size can be increased by coarsening npAu at elevated temperatures because Au atoms start to diffuse to reduce the surface energy.[7]

2.3 Electrode-Electrolyte Interface and Point of Zero Charge

The investigation of the interfacial properties between an electrode and an electrolyte is crucial for enzyme immobilization. The charge accumulating at the interface is of special interest since it can be used for enzyme immobilization via electrostatic bonds. Knowledge about the charge accumulating at the electrode-electrolyte interface and other interfacial properties can be gained with electrochemical measurements.

For electrochemical measurements and other electrochemical processes, such as dealloying, an electrochemical cell is used. A very simple electrochemical cell is the three-electrode configuration, which consists of a working electrode (WE), a reference electrode (RE) and a counter electrode (CE) immersed in an electrolyte. The setup is schematically shown in figure 2.5. The WE is the sample which is modified or

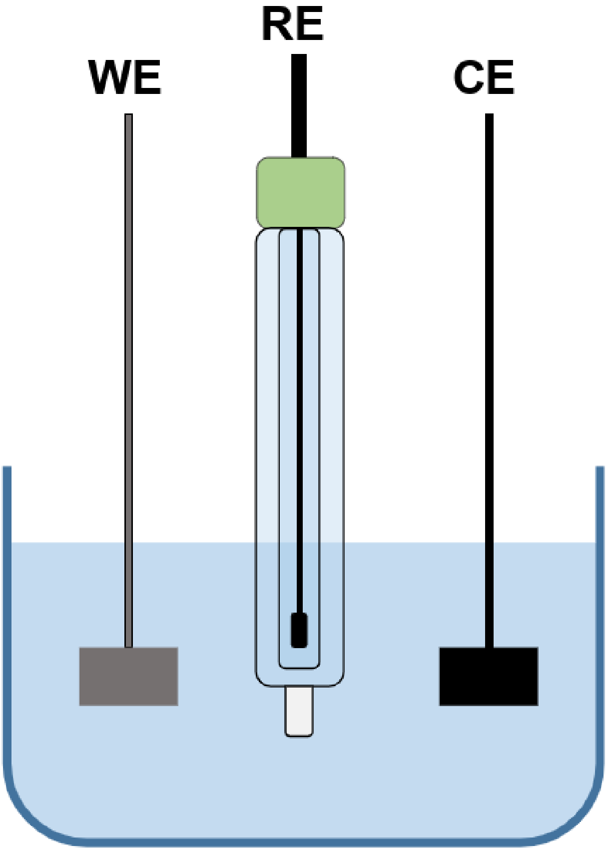

Figure 2.5: Schematic representation of a three-electrode configuration with working electrode (WE), reference electrode (RE) and counter electrode (CE).

investigated and the potential of the WE is given versus the stable and well-known potential of the RE. The potentials of all reference electrodes are given versus the potential of the standard hydrogen electrode (SHE), which is set to zero. Reference electrodes of the second type, which are connected to the electrolyte with a salt bridge, are used in most electrochemical setups because they are easier to handle than a SHE. An example of such a reference electrode is the Ag/AgCl electrode, which is also used in this work and has a potential of +197 mV versus the SHE potential. The CE is used to close the electrical circuit and to allow current to flow, since there should be no current between WE and RE.[26]

In electrochemistry, the processes at the interface between an electrode and an electrolyte are studied. This interface is particularly interesting because it separates two chemical phases, an electronic conductor (electrode) and an ionic conductor (electrolyte). Generally, an electrode and an electrolyte do not have the same chemical potential for electrons μ_{e^-}. When they are in contact this difference must be balanced to reach equilibrium. This occurs by accumulation of charge within the electrode which are balanced by ions in the electrolyte which render the whole interface electrically neutral. If $\mu_{\mathrm{e^-},\mathrm{metal}} > \mu_{\mathrm{e^-},\mathrm{electrolyte}}$, the metal gets negatively and the electrolyte positively charged, whereas if $\mu_{\mathrm{e^-},\mathrm{metal}} < \mu_{\mathrm{e^-},\mathrm{electrolyte}}$, the metal is positively and the electrolyte negatively charged. A potential difference arises between the two phases which stops the reaction when equilibrium of the electrochemical potential is reached. The electrochemical potential for electrons is defined as:[26]

$$\mu^*_{\mathrm{e^-}} = \mu^0_{\mathrm{e^-}} + RT\ln(a_{\mathrm{e^-}}) - F\phi, \tag{2.6}$$

where $\mu^0_{\mathrm{e^-}}$ is the chemical potential of the pure phase, R the gas constant, T the temperature, $a_{\mathrm{e^-}}$ the activity of the electrons, F Faraday's constant and ϕ the Galvani potential. If there is no electroactive species present in the electrolyte which can be oxidized or reduced by the arising voltage the current across the interface is purely capacitive without any charge transfer across the interface.

If there is a redox couple in the electrolyte that can be reduced (oxidized) by the arising potential difference, charge transfer across the interface occurs. For the case of a negatively charged electrode, the electrode acts as an electron donor which reduces the oxidized species in the electrolyte. If the electrode is positively charged it can accept electrons and oxidize the reduced species in the electrolyte. This reaction can balance the electrochemical potential in equation 2.6 of the electrons. In a metal electrode the activity is taken as $a_{\mathrm{e^-},\mathrm{metal}} = 1$ and in the electrolyte it can be calculated via $a_{\mathrm{e^-},\mathrm{electrolyte}} = (K_\mathrm{a}\frac{a_\mathrm{red}}{a_\mathrm{ox}})^{\frac{1}{n}}$, where K_a is the reaction constant for the redox reaction and n is the number of transferred electrons. The equilibrium Galvani potential can be calculated to:[26]

$$\Delta\phi_0 = \Delta\phi_{00} + \frac{RT}{nF}\ln\frac{a_\mathrm{ox}}{a_\mathrm{red}}, \tag{2.7}$$

where $\Delta\phi_{00}$ is the standard Galvani potential, R the gas constant, T the temperature, n the number of electrons involved in one reaction, F Faraday's constant and a_ox and a_red the activities of oxidized and reduced species, respectively. If the potential is related to a definable reference potential this equation is called Nernst equation. Since it is experimentally impossible to measure the potential difference between an electrode and an electrolyte, reference electrodes are used as shown in the electrochemical setup

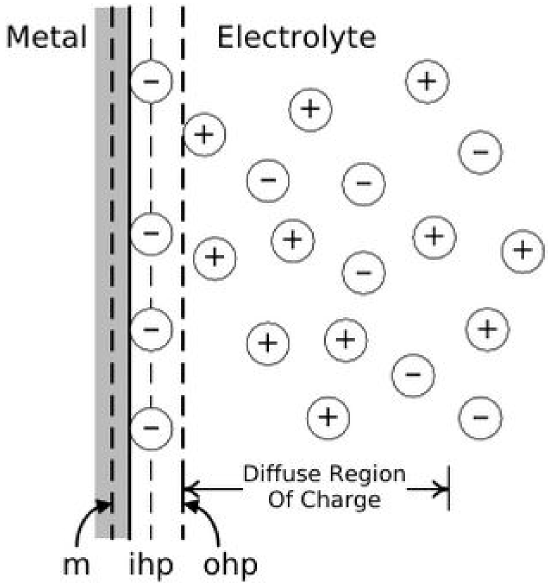

Figure 2.6: Model of the electrode-electrolyte interface with electric double layer. Reprinted with permission from[27]. Copyright 2017 John Wiley and Sons.

in figure 2.5.[26]

The charge present at the interface creates an electrical double layer. One representation of the electrode-electrolyte interface is shown in figure 2.6. The electrode is usually a good conductor so that the charge in the electrode lays close to the surface in the plane m. On the electrolyte side of the interface, ions of the opposite charge as the electrode are attracted and accumulate close to the interface in a diffuse layer. If they stay in their solvated state they can approach the interface to half the diameter of the solvation shell plus the size of solvent molecules adsorbed at the interface. The plane of closest approach of these solvated ions is the outer Helmholtz plane (ohp). Further away from the interface the excess charge concentration decreases with increasing distance. Some molecules or ions might be present in the electrolyte that have a tendency to specifically adsorb on the metal surface. Specific adsorption can originate from van der Waals interactions or from Coulomb interactions between the molecules in the solution and the electrons, which are present slightly outside the lattice of metal cations. The potential of the electrode can support or oppose adsorption. Often, anions tend to adsorb due to van der Waals interactions and can be present even if the electrode is negatively charged. The inner Helmholtz plane (ihp) cuts through the center of these adsorbed molecules. In equilibrium the charge accumulating in the metal is balanced by the charge in the solution. The electrode potential at which no excess charge are present in the metal and on the electrolyte side (including adsorbed

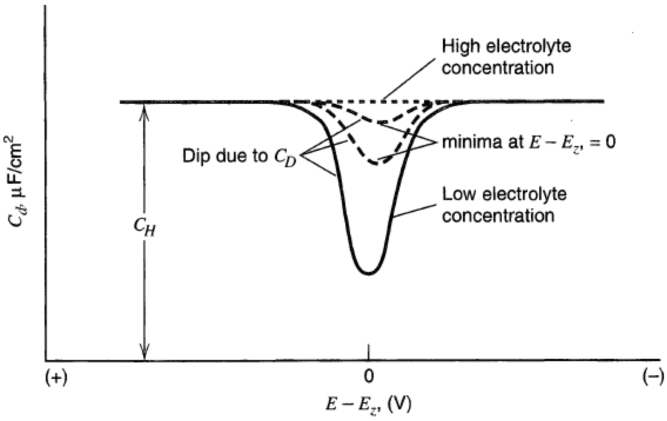

Figure 2.7: Expected behaviour of the differential capacitance C_d versus potential E at different electrolyte concentrations according to the GCS model. $E_{\mathrm{Z}'}$ is the point of zero charge. Reprinted with permission from[28]. Copyright 2000 John Wiley and Sons.

ions and ions in the diffuse layer) is called the point of zero charge (PZC).[26]

A model commonly used to describe the interface is defined by the Gouy-Chapman-Stern-Theory (GCS) which includes ions at the ohp and ions in the truly diffuse layer, but does not account for specifically adsorbed ions. With this model an expression for the differential interfacial capacitance C can be derived. C is defined as:

$$C = \frac{d\sigma_\mathrm{M}}{d\phi_\mathrm{M}}, \tag{2.8}$$

where σ_M is the charge density in the electrode and ϕ_M the electrode potential. It can be separated into two capacitors connected in series, one for the ions at the ohp and one for the truly diffuse ions[28] :

$$\frac{1}{C} = \frac{1}{C_\mathrm{H}} + \frac{1}{C_\mathrm{D}}. \tag{2.9}$$

Only the diffuse part C_D depends on the potential, $C_\mathrm{H} = \frac{x_2}{\epsilon\epsilon_0}$ can be considered as a plate capacitor where x_2 is the difference between the surface of the electrode and the ohp. The total interfacial capacitance is dominated by the smaller one of the two terms. When the electrolyte concentration is high, the diffuse layer will be compact and C_D larger than C_H. In this case C_H will dominate C, which is then independent of potential. At low electrolyte concentrations the diffuse layer is wide and C_D much smaller and it can become the dominant term of the equation. C_D and also C will then have a

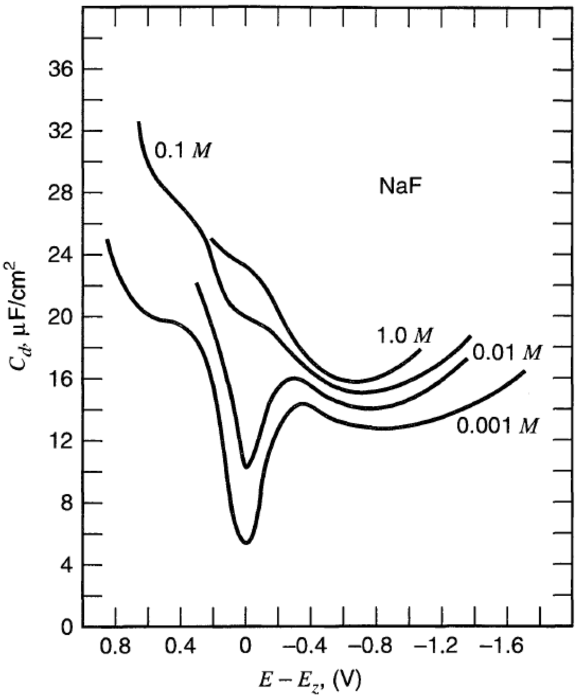

Figure 2.8: Differential capacitance C_d versus potential E of the interface between a mercury electrode and NaF solutions with different concentrations. $E_{Z'}$ is the point of zero charge. Reprinted with permission from[31]. Copyright 1947 American Chemical Society.

minimum at the PZC (figure 2.7 where $E_{Z'}$ is the PZC)[28]. Therefore, experiments are often carried out using electrolyte concentrations lower than 10^{-2} M[29]. Since the electrode potential can be determined easily during experiments but the potential at the ohp cannot, ϕ_M is used in some publications to calculate the contribution of C_D (for example[30]).

The GCS model does not consider the influence of charged or uncharged species specifically adsorbed on the electrode and also other aspects are neglected, for example that C_H is not completely independent of potential[28]. Therefore, experimental data of the interfacial capacitance are more complex than the model in figure 2.7. An example is shown in figure 2.8[31].

In the case of asymmetric adsorption of electrolyte ions on the electrode, where one species of ion is preferentially adsorbed, the minimum of the interfacial capacitance does not correspond to the PZC. Both the PZC and the capacitive minimum shift to more positive potentials with increasing concentration in case of cation adsorption and to more negative potentials for anion adsorption[32]. Specifically adsorbed anions carry a charge on the electrolyte side of the interface which must be balanced. A positive countercharge is induced in the electrode because it is more polarizable than the electrolyte. Therefore, a more negative potential must be applied to the electrode to get rid of the positive charge and fulfill the condition of zero charge. The charge of the adsorbed anions is then balanced by cations in the diffuse layer[28].

If there is an additional layer, such as SAMs or an oxide layer, there is an additional capacitance:

$$C_{\mathrm{layer}} = \frac{\epsilon_{\mathrm{i}}\epsilon_0}{d}, \tag{2.10}$$

where ϵ_{i} is the dielectric constant of the layer material, ϵ_0 is the permittivity of vacuum and d is the layer thickness. This capacitance is in series with the double layer capacitance[27]. The SAM capacitance strongly depends on the length of the used molecules because longer molecules lead to a smaller capacitance. Most layers have a capacitance much lower than the double layer capacitance and they dominate the total interfacial capacitance[27].

Since there is a potential drop across the SAM there is a shift in the PZC. The potential shift depends on the polarity of the used molecules perpendicular to the interface plane, where a higher polarity leads to a bigger shift in potential. For an alkanethiol monolayer the shift with chain length can be expressed by[33]:

$$\Delta U_{PZC} = -\frac{N\Delta\mu_{\perp}}{\epsilon_0\epsilon_{\mathrm{i}}}, \tag{2.11}$$

where N is the surface density of thiol molecules, $\mu_{\perp}$ the molecular dipole moment perpendicular to the interface plane, ϵ_0 the vacuum permittivity and ϵ_{i} the effective permittivity of the monolayer.[33]

2.3.1 Cyclic Voltammetry

Cyclic voltammetry (CV) is a very commonly used method to investigate electrochemical interfaces. A three-electrode configuration as described above and shown in 2.5 is used to conduct the experiment. A potential is applied to the WE versus the fixed potential of the RE. This potential is then changed linearly with a fixed scan rate ν (in mV/s) until it reaches a predefined switching potential. Then the scan direction is reversed and the potential changes with the same scan rate in the other direction. Thus the potential variation has a triangular shape (figure 2.9) and the potential can be cycled between the two switching points. The starting potential of the measurement is normally chosen to be close to the open circuit potential (OCP) of the system. The data are usually plotted as current I versus potential U.

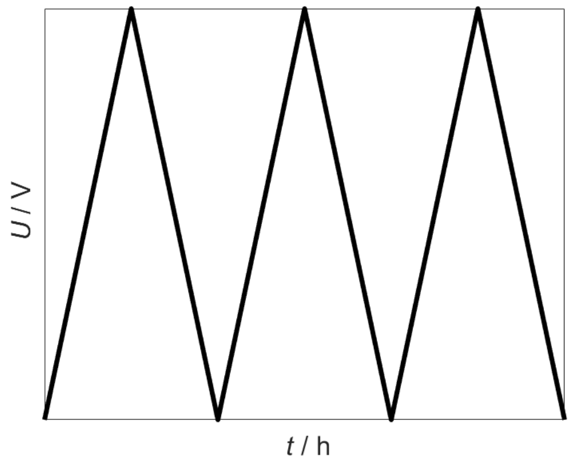

Figure 2.9: Potential U versus time t during a CV scan.

If an electroactive species is present, a faradaic reaction occurs when the potential is sufficiently positive to oxidize the species. A peak appears in the I versus U plot in the positive scan direction. Since the WE works as an anode for this reaction the scans in positive direction are called anodic scans. Similarly, scans in negative direction are called cathodic scans[34]. During the cathodic scan a peak appears at a more negative potential. The formal reduction potential of the redox couple is approximately in the middle between the anodic and the cathodic peak potential[35]. The separation between the two peaks is about $58/n$ mV when the reaction is reversible, where n is the number of transferred electrons. For irreversible reactions the peak separation is larger and the peaks do not overlap[34] [35]. Reactions that are reversible at low scan rates and irreversible at higher scan rates are called quasi-reversible[35].

If no additional electroactive species is present in an aqueous electrolyte, the only reactions are hydrogen evolution at low potentials and oxygen evolution at high potentials. Between the hydrogen evolution regime and the oxygen regime is the double layer regime where no faradaic reaction takes place. The current in the double layer regime is purely capacitive and proportional to the scan rate: $I = \nu C$. With this equation it is possible to obtain a value for C by performing scans with different scan rates. C is the slope of I versus ν[36]. An example of a CV scan with the three regimes can be seen in figure 2.10 where a CV spectrum of npAu in 10 mM $HClO_4$ with a scan rate of 1 mV/s is shown. The double layer regime is found to be roughly between −300 mV and +500 mV. Below −300 mV in the cathodic scan the onset of the hydrogen evolution is visible. Above +900 mV oxygen adsorption strongly increases the current during the anodic scan. A counterpeak appears in the cathodic scan at about +700 mV corresponding to oxygen desorption.

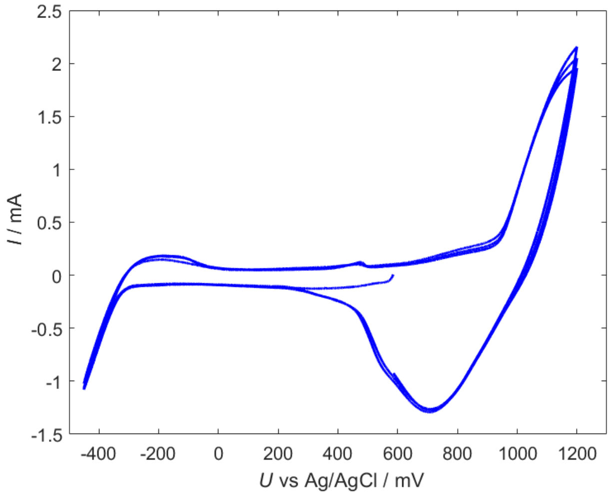

Figure 2.10: CV of untreated npAu in 10 mM $HClO_4$ between −450 mV and 1200 mV with a scan rate of 1 mV/s to determine the limits of the double layer regime.

2.3.2 Electrochemical Impedance Spectroscopy

This part about electrochemical impedance spectroscopy (EIS) is based on the book “Electrochemical Impedance Spectroscopy“ by Orazem[27]. Only a short summary is presented here including the information relevant for this work.

In an EIS measurement the reaction of a system to a sinusoidal input signal is observed for different frequencies of the input signal. In combination with equivalent electrical circuits (EEC) to fit the measured data, EIS can be used to gain a lot of information about the system, such as interfacial capacitance and pore resistance.

To perform an EIS measurement a constant DC potential overlapped by a small AC signal is applied to the electrochemical cell. The response of the system is measured for different applied AC frequencies and compared to the input signal. The transfer function is the relation between the input signal and the measured output. It consists of two parameters that depend on the frequency: the gain $H(\omega)$ and the phase $\varphi(\omega)$

$$|H(\omega)| = \frac{|Y|}{|X|}, \tag{2.12}$$

$$|\varphi(\omega)| = 2\pi\frac{\Delta t}{T}. \tag{2.13}$$

$|X|$ and $|Y|$ are the magnitude of the input and the output signal, ω is the frequency of excitation, Δt the time shift between the input and output signal, and T the time period. For most EIS measurements the input signal is a potential $\tilde{V}(\omega)$ and the output signal is a current $\tilde{i}(\omega)$. The impedance $Z(\omega)$ can then be calculated as the inverse of the transfer function:

$$Z(\omega) = \frac{\tilde{V}(\omega)}{\tilde{i}(\omega)}. \tag{2.14}$$

EECs are used to fit the the measured EIS data. They consist of several resistors and capacitors which describe the electrochemical interface. An example is shown in figure 2.11. Using EEC, it is possible to gain some insight into the processes at the interface. It is, however, not always possible to directly relate the elements of the equivalent circuit to physical processes.

The total impedance of a planar electrode immersed in an electrolyte consists of the electrolyte resistance R_e and the interfacial impedance Z_0. Since the current across the interface generally consists of a Faradaic current i_F and a capacitive charging current i_C, Z_0 consists of a double layer capacitor C_dl in parallel with the Faradaic impedance Z_F. In the case of a single reaction on a unifrom electrode, Z_F can be expressed as a charge transfer resistance R_ct[27] (figure 2.11). When no Faradaic process or chemical reaction takes place, R_ct is very large and the interfacial impedance is purely capacitive. The imaginary impedance of the system goes to infinity and the phase angle φ to -90° for $\omega \to 0$. The electrode is in its blocking state.

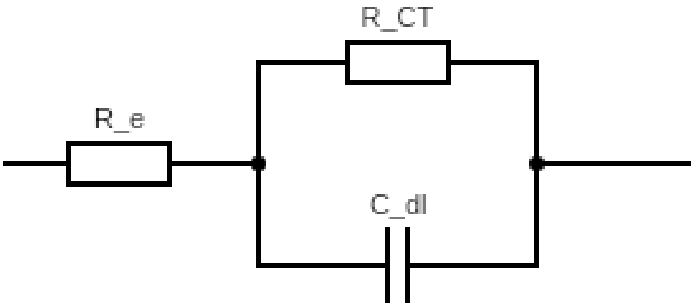

Figure 2.11: Equivalent electrical circuit for a planar electrode in an electrolyte with electrolyte resistance R_e, double layer capacitance C_{dl} and charge transfer resistance R_{ct}.

Constant phase elements (CPE) are often used to replace capacitors in EEC fits to improve the fit quality. In many publications this is done due to surface heterogeneity or a distribution of time constants. For the circuit described above the interfacial impedance Z can be expressed for the non-blocking state Z_{nb} and for the blocking state Z_{b} as:

$$Z_{\mathrm{nb}} = R_{\mathrm{e}} + \frac{R_{\mathrm{ct}}}{1 + R_{\mathrm{ct}}(i\omega)^{\alpha}Q}, \tag{2.15}$$

$$Z_{\mathrm{b}} = R_{\mathrm{e}} + \frac{1}{(i\omega)^{\alpha}Q}, \tag{2.16}$$

where Q is the CPE coefficient. α is an indication for the deviation of the system from the capacitive behavior and can be obtained by graphical methods . When $\alpha = 1$, Q is equivalent to a capacitance and the system is only connected to a single time constant. When $\alpha < 1$ the system has a distribution of time constants or a heterogeneous surface. The impedance of the capacitor $\frac{1}{i\omega C}$ is then replaced by $\frac{1}{(i\omega)^{\alpha}Q}$.[27]

Graphical interpretation of EIS data

Besides EEC fits, graphical methods can be applied for the interpretation of EIS data to give a qualitative interpretation of the system. The Nyquist plot ($-Z_{\mathrm{im}}(f)$ vs $Z_{\mathrm{re}}(f)$), the Bode modulus plot ($Z(f)$ vs f), and the Bode phase plot ($-\varphi(f)$ vs f) are the most commonly used plots of impedance data. Additionally, $Z_{\mathrm{im}}(f)$

versus f and the effective capacitance $C_{\mathrm{eff}}(f)$ versus f are presented here. An example from the book “Electrochemical Impedance Spectroscopy“ by Orazem[27] is used to demonstrate the advantages and disadvantages of the different plots. The data are simulated with the EEC shown in figure 2.12 and the values of the elements are listed in table 2.1. It consists of the electrolyte resistance R_{e}, the resistance of a layer on the electrode R_{l}, the charge transfer resistance R_{ct}, the layer capacitance C_{l} and the double layer capacitance C_{dl}. In the case of the blocking electrode, there is no R_{ct} and no charge transfer across the interface, which leads to purely capacitive behavior at low frequencies. For the non-blocking case with a finite R_{ct}, there is charge transfer across the interface which strongly influences the spectrum at low frequencies. In figures 2.13 to 2.16, the plots correspond to ideal capacitances. Deviations arising from replacing a capacitance by a constant phase element are only described in the text. The parameters of this simulation give two RC elements which dominate the spectrum in different frequency regimes, one in the high frequency regime with a characteristic frequency of $f_{\mathrm{ch1}} = 18\,\mathrm{kHz}$ and one in the low frequency regime with a characteristic frequency of $f_{\mathrm{ch2}} = 0.4\,\mathrm{Hz}$. This is used to highlight the difference between blocking and non-blocking state and to find the transition frequency between the two regimes.

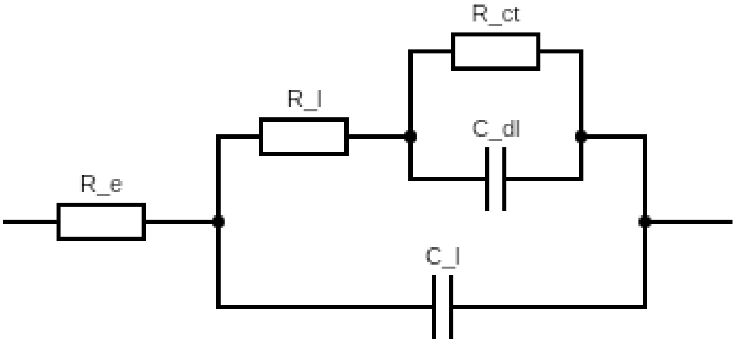

Figure 2.12: Equivalent electrical circuit with electrolyte resistance R_{e}, capacitance of a layer C_{l}, layer resistance R_{l}, double layer capacitance C_{dl} and charge transfer resistance R_{ct}.

Table 2.1: Values of the elements in the EEC in figure 2.12 with electrolyte resistance R_{e}, layer resistance R_{l}, charge transfer resistance R_{ct}, capacitance of a layer C_{l} and double layer capacitance C_{dl}.

R_{e} / Ω	R_{l} / Ω	R_{ct} / Ω	C_{l} / µF	C_{dl} / µF
100	100	10^5	0.0885	4

From the Nyquist plot shown in figure 2.13 information about the resistances and capacitances present in the system can be gained. A semicircle in the Nyquist plot corresponds to a process with a single time constant and is represented by a RC element in an EEC. The characteristic frequency f_{ch} of this process is the frequency at the maximum of the semicircle, the resistance is the diameter of the semicircle on the real axis, and the capacitance can be calculated as $C = \frac{1}{2\pi f_{\mathrm{ch}} R}$. The high frequency limit of the semicircle on the real axis is R_{e} and the low frequency limit is $R_{\mathrm{e}} + R$. A depressed shape of the semicircle indicates that more than one time constant is involved and to achieve good fit quality more than one RC element must be used. If a distribution of time constant exists, the capacitance must be replaced by a CPE. In the example two semicircles with well separated time constants can be seen for the non-blocking case (— in figures 2.13a and 2.13b) with characteristic frequencies indicated by a green symbol (✕). In the case of a blocking electrode (○) only one semicircle appears at high frequencies (figure 2.13a) and $-Z_{\mathrm{im}}$ increases strongly in the low frequency range at a constant Z_{re} (figure 2.13b), which is the typical capacitive behavior.

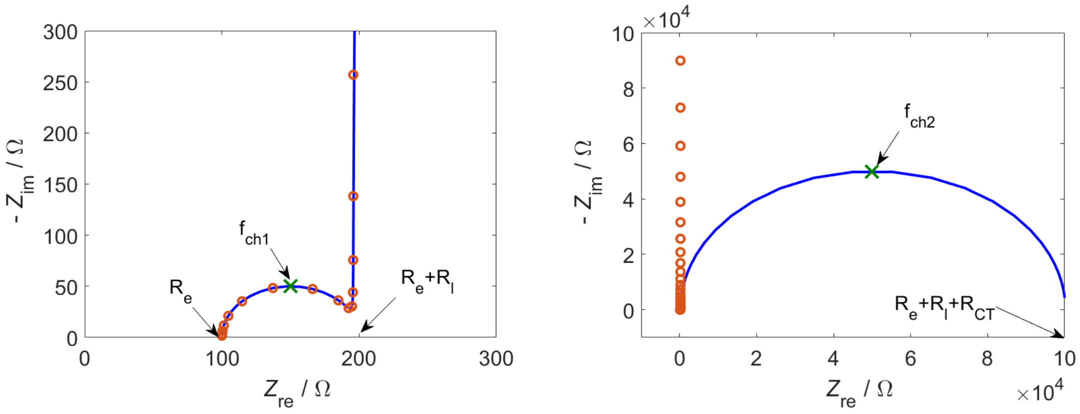

(a) **(b)**

Figure 2.13: Nyquist plots of the EEC circuit shown in figure 2.12 for the blocking state (○) and the non-blocking state (—) with the characteristic frequencies of the RC elements (✕): (a) high-frequency part, (b) low-frequency part.

Another possibility for graphic evaluation of the system is using the Bode plots. An example is given in figure 2.14. However, they have the big disadvantage that they are dominated by R_{e} in the high frequency limit due to the low impedance of the capacitors. The Bode modulus (figure 2.14a) plot goes towards R_{e}. If it is possible to estimate a value of R_{e}, for example with an EEC fit, the Bode modulus plot can be corrected to gain information about the system also in the high frequency regime with

$$|Z| = \sqrt{(Z_{\mathrm{re}} - R_{\mathrm{e}})^2 + Z_{\mathrm{im}}^2}. \tag{2.17}$$

The slope of the corrected impedance (▽) in the high frequency part is $-\alpha$ for a CPE and -1 for a perfect capacitor. In the low-frequency limit, $|Z|$ is constant for a non-blocking electrode (for the uncorrected (—) and corrected (▽) modulus) whereas the slope remains $-\alpha$ or -1 for the blocking electrode (◯). In the example, two RC elements are used to simulate the data. In the Bode modulus plot it is possible to find an intersection (—) between the constant low frequency regime of the first RC element and the high frequency part with a slope of -1 of the second RC element. At frequencies below this frequency constant f_{C} the system is dominated by the second RC element.

The Bode phase plot (figure 2.14b) is also dominated by R_{e} in the high frequency regime. It goes towards zero at high and low frequencies for the non-blocking electrode (—). The low frequency limit is 90° for the blocking electrode (◯), i.e. for a perfect capacitance, and $\alpha \cdot 90°$ for a CPE. The plot can be corrected with

$$\varphi = \tan^{-1}\left(\frac{Z_{\mathrm{im}}}{Z_{\mathrm{re}} - R_{\mathrm{e}}}\right). \tag{2.18}$$

The high frequency limit of the corrected Bode phase plot (▽) is 90° if the RC element has perfect capacitance and $\alpha \cdot 90°$ for a CPE. f_{C} determined in the Bode modulus plot is indicated again in black (—).

Another way to obtain characteristic frequencies $f_{\mathrm{ch}1,2}$ of the RC elements and a value for α of the CPE is the graphical analysis of the imaginary part of the impedance. $f_{\mathrm{ch}1,2}$ can be taken from the maxima (indicated by —) of Z_{im} vs f (— in figure 2.15a). The slope on the left and right side of a maximum is α and $-\alpha$, respectively, for a CPE or 1 and -1 for a capacitance. For the blocking electrode (◯) the second maximum does not appear in the plot and Z_{im} keeps increasing linearly down to lowest frequencies. Since it is not always easy to estimate if the curve is linear or slightly curved, the slope can be obtained more accurately by taking the derivative. f_{C} from the Bode modulus plot is again marked with a black line in the plots (—). It coincides well with the frequency where the slope is again at -1 when going towards smaller frequencies. A big advantage of plotting Z_{im} instead of $|Z|$ and φ (Bode plots) is that

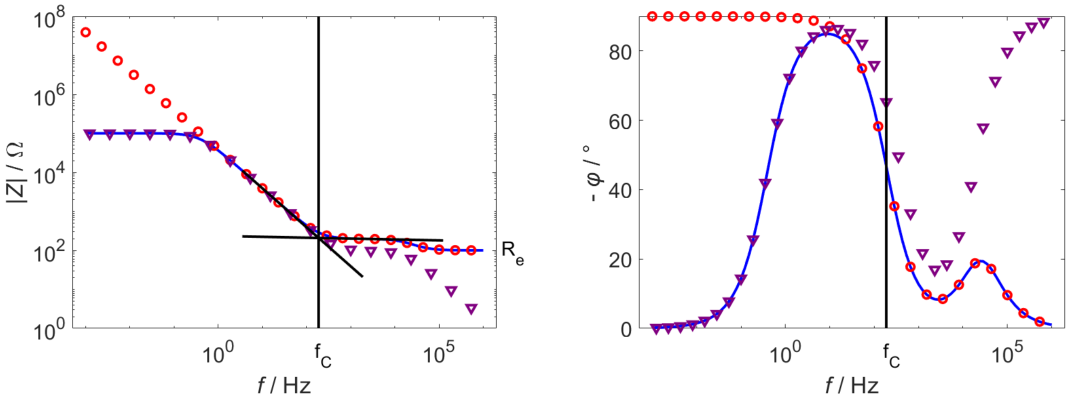

(a) **(b)**

Figure 2.14: Bode plots of the EEC circuit shown in figure 2.12 for the blocking state (◯) and the non-blocking state (—) and the non-blocking state corrected with the electrolyte resistance (▽): (a) Bode modulus plot with fit of two linear regimes of the uncorrected data and vertical line at intersection (—), (b) Bode phase plot with vertical line at the same frequency (—).

no estimation of R_e is needed.

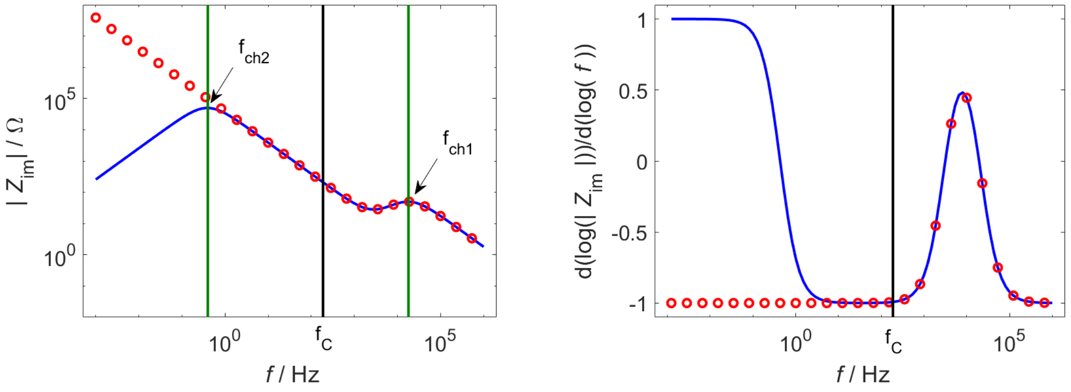

(a) **(b)**

Figure 2.15: (a) Imaginary part of the impedance versus frequency of the EEC circuit shown in figure 2.12 for the blocking state (◯) and the non-blocking state (—) with characteristic frequencies of the RC elements (—) and frequency constant determined in the Bod modulus plot (—) (b) Derivative of (a).

The effective capacitance C_eff can be used to estimate the capacitances present in the system if the frequency regimes of the different RC elements are well separated. An effective capacitance C_eff or an effective CPE coefficient Q_eff of the system can be calculated at each frequency according to:

$$C_{\mathrm{eff}} = \frac{-1}{2\pi f Z_{\mathrm{im}}}, \tag{2.19}$$

$$Q_{\mathrm{eff}} = \sin(\frac{\alpha\pi}{2})\frac{-1}{(2\pi f)^{\alpha} Z_{\mathrm{im}}}. \tag{2.20}$$

In the high frequency limit C_{eff} corresponds to the capacitance of the RC element. It increases when going towards lower frequencies in the non-blocking case (— in figure 2.16). For a blocking electrode (○), C_{eff} is independent of frequency. f_{C} is again indicated by a black line (—) and fits well with the high frequency limit of the second RC element. C_{eff} is 4.1 µF at this frequency which is close to the 4.0 µF of C_{dl}.

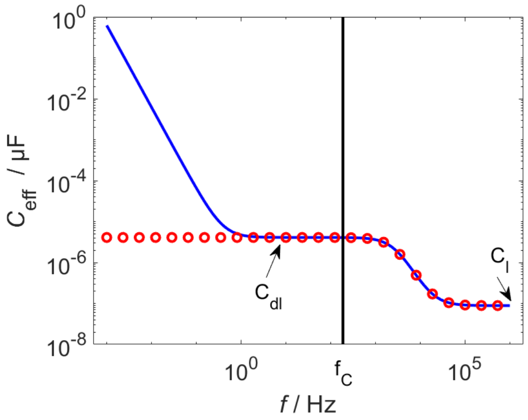

Figure 2.16: Effective capacitance of the of the EEC circuit shown in figure 2.12 for the blocking state (○) and the non-blocking state (—) and f_{C} (—).

Single frequency point of zero charge

C_{eff} is used in several publications to obtain a value of C[37] [38]. It can then be used to find the PZC for which C is minimal[39]. Since C_{eff} depends strongly on the frequency, it is necessary to use the right frequency related to the process under investigation for the calculations.

Different physical and chemical phenomena occur at different time constants and, therefore, dominate the EIS-spectrum in different frequency regimes. Using the Bode modulus plot of an EIS spectrum recorded at the OCP it is possible to determine time constants associated with these phenomena. They can be found at the transition between two linear regimes in the Bode modulus plot[39]. It is then possible to choose a smaller regime of frequencies or even a single frequency f_C at which the interfacial capacitance is dominated by the double layer contribution and not by any Faradaic or chemical process. The dependence of interfacial capacitance on the applied potential can then be investigated and the PZC be determined. An example from literature[39] is shown in figure 2.17. In this plot the frequency regime dominated by the double layer capacitance is located below the interception at 125 Hz. Frequencies around the other constant of 0.18 Hz are related to chemical reactions or diffusion processes.

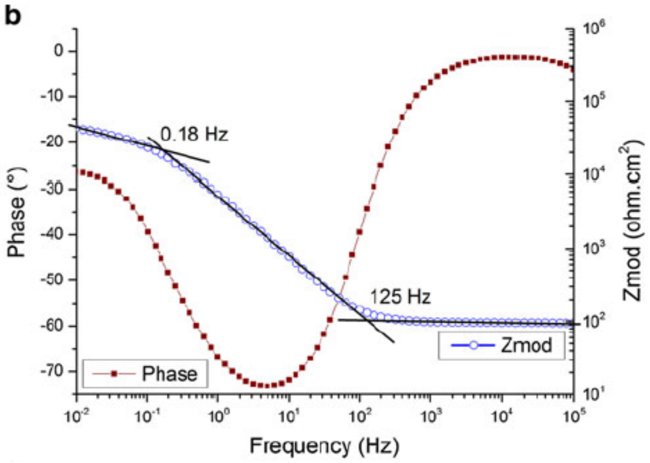

Figure 2.17: Bode Modulus (blue, Z_{mod} versus frequency) and Bode Phase (red, phase versus frequency) plots from EIS measurements of Ni30Cu70 in 0.1 M Na_2SO_4 at -0.9 V vs. MSE. Reprinted with permission from[39]. Copyright 2013 Springer Nature.

Nanoporous electrodes

For porous electrodes a more elaborate EEC is needed than for planar electrodes. According to the theory of de Levie[40] and Keiser[41], a porous electrode can be described by the pore electrolyte resistance per unit length R_{i} (in $\frac{\Omega}{\mathrm{cm}}$) in parallel with impedances for the interfacial impedance per unit length Z_{i} (in Ωcm). The electrolyte resistance outside the sample is described by a resistor. The model is shown in figure 2.18. In a porous electrode the interface is not uniformly accessible and the size of available interface depends on the frequency. The penetration depth of the AC signal can be expressed as $\lambda = \sqrt{\frac{Z}{R}}$ and increases with decreasing frequency due to the frequency-dependent capacitive part of Z. At high frequencies λ is much smaller than the pore length L and the pore shows semi-infinite behavior. For a purely capacitive Z the phase angle is then 45°. At lower frequencies $\lambda >> L$, the interface seems quasi planar and the phase angle increases to 90°[42]. In this case of a blocking electrode simple calculation of the pore resistance R_{pore} and the total interfacial capacitance C is possible[43]:

$$R_{pore} = \sum_{i=1}^{N} R_i, \tag{2.21}$$

$$C = \sum_{i=1}^{N+1} C_i, \tag{2.22}$$

where N is the number of used resistances. An example of the EEC is shown in figure 2.19b. 5 RC elements are used to fit the data.

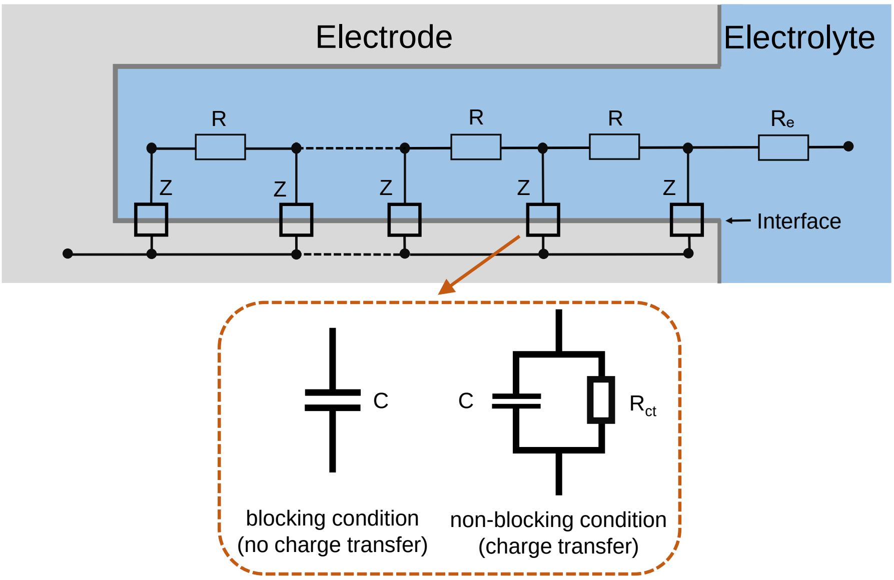

Figure 2.18: Model of a cylindrical pore electrode with an EEC consisting of electrolyte resistance R_{e}, pore resistance R and interfacial impedance Z in the blocking and non-blocking state. Reprinted with permission from[43].

In a previous master thesis at the Institute of Material Physics written by Philipp Brunner, EIS measurements on nanoporous samples of Au and Pd were performed and analyzed[43]. The results of this thesis build the starting point of the EIS measurements done within the present work. It was observed that the first two RC elements in the EEC create the small semicircle at high frequencies (visible for example in figure 2.19a). The capacitances of these two RC elements are much smaller than in the other RC elements and they originate from the Au wire used to contact the samples. Therefore, they are not included in the calculation of the interfacial capacitance of the npAu sample. The first resistance of 71.2 Ω represents the electrolyte resistance outside the pores.

In his master thesis, Philipp Brunner also noticed, that the value of C does not depend much on the number N of used RC elements, but the value of R increases with N and the error of R gets larger for higher N. Since the fit quality is bad for low N, it is necessary to find a trade-off to have an acceptable fit quality and a reasonably low error of R.

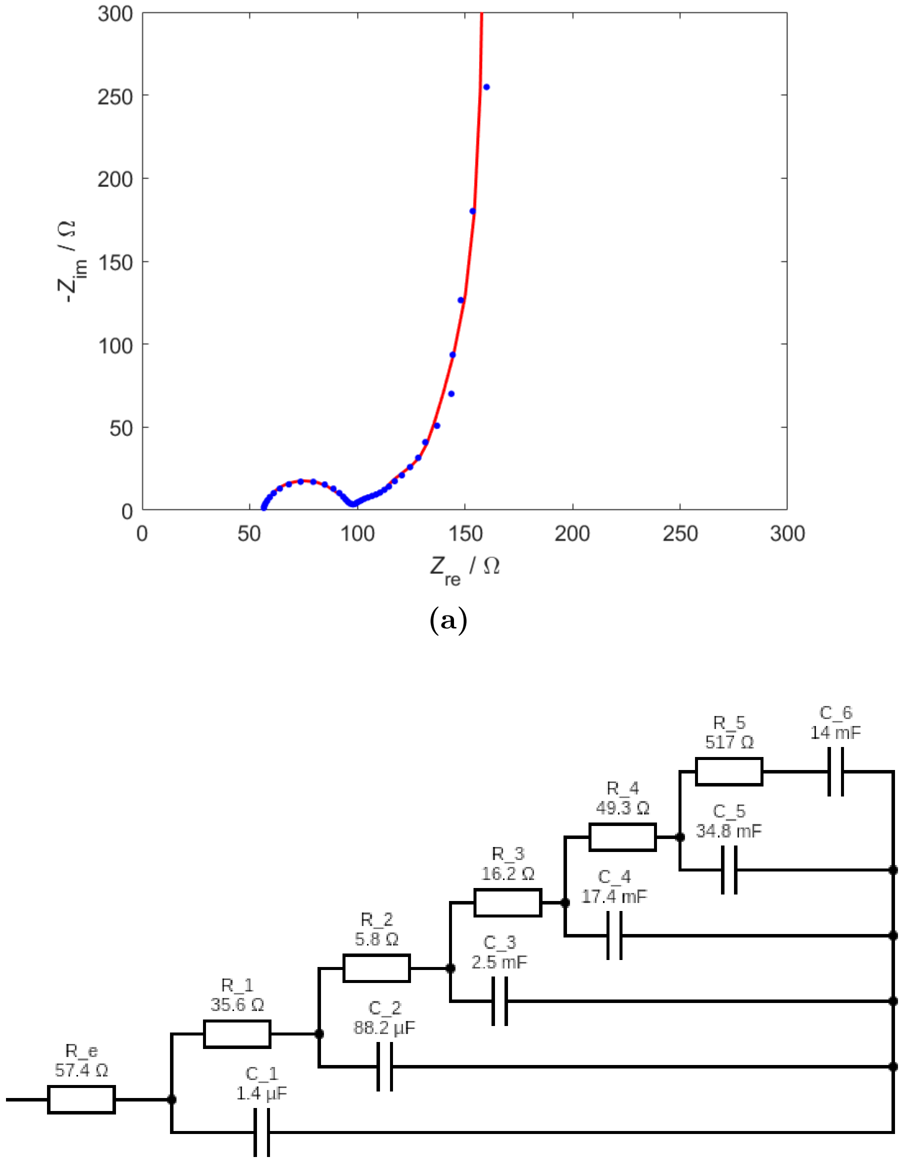

(a)

(b)

Figure 2.19: Data of EIS measurement on a npAu sample between 100 kHz and 10 mHz and EEC fit: (a) Nyquist plot of measured EIS data (●) and fit (—), (b) Equivalent electrical circuit according to the theory of de Levie[40] and Keiser[41].

In the case that reactions take place at the electrode-electrolyte interface, the EEC needs to be adjusted by adding a charge transfer resistance in parallel with the last capacitance. A charge transfer current can then flow when $\omega \rightarrow 0$. In the Nyquist plot the onset of a big semicircle can be seen in the low frequency range. This effect appears when the applied DC potential coincides with the potential of a chemical or Faradaic reaction. Forward and backward reaction or adsorption and desorption can then be induced by the AC signal and charge is transferred between electrode and electrolyte.

2.4 Protonation - Deprotonation

The control of the surface charge of npAu modified with SAMs can be improved further when the SAMs are functionalized with carboxyl groups. The degree of acid dissociation can be controlled by changing the applied potential or the pH of the electrolyte. An electrostatic bond can then be created between the charged carboxyl groups of the SAMs and enzymes containing a polar group.

This section about protonation and deprotonation of SAMs is mostly based on the thermodynamic model developed by Smith and White[44] and the kinetic model by Burgess et al.[18]. The molecules used for SAMs in their publications have a carboxyl group at the unbound end from which a hydrogen ion can dissociate (deprotonation). It is assumed that these groups all lie in the same plane, the plane of acid dissociation (PAD, figure 2.20). Depending on the pH of the used electrolyte and the potential difference $\Delta V_\mathrm{s} = \Phi_\mathrm{PAD} - \Phi_\mathrm{S}$ between the PAD and the potential of the bulk electrolyte, a fraction of molecules is in the deprotonated state[44]. The surface $\mathrm{p}K_\mathrm{a}$ is the dissociation constant of the acidic monolayers when there is no electric field in this region ($\Delta V_\mathrm{s} = 0$). It can differ strongly from the $\mathrm{p}K_\mathrm{a}$ of the same molecules in solution without forming a SAM. The difference can arise from field-dependent or solvent-dependent stabilization or destabilization of the acid group. The proton concentration at the acid group has also an influence on the $\mathrm{p}K_\mathrm{a}$[18].

Externally changing the potential distribution by applying a potential can change the degree of acid dissociation (figure 2.20B). The equilibrium shifts with applied electrode potential to minimize the free energy. This results in a current visible in CV measurements. Applying a potential negative of the PZC on an electrode covered with

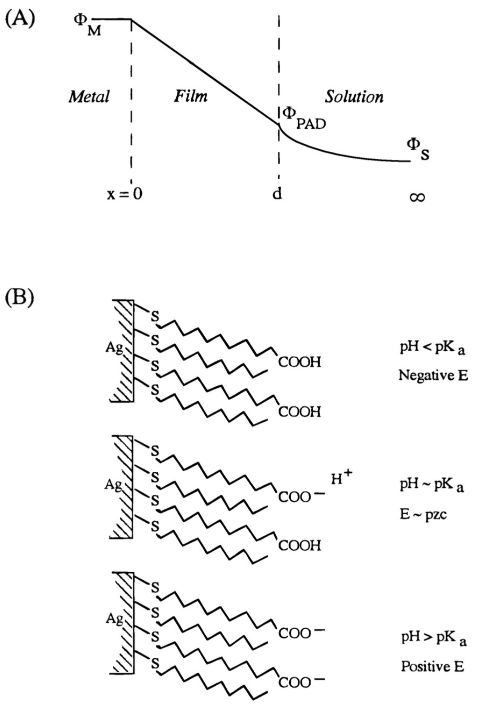

Figure 2.20: (A) Electrostatic potential distribution across a metal/acid monolayer/solution interface. (B) Schematic representation of a mixed monolayer of 11-mercaptoundecanoic acid and 1-decanethiol in contact with an electrolyte solution as a function of electrode potential (E) and pH. Reprinted with permission from[45]. Copyright 1998 American Chemical Society.

a SAM will decrease the degree of acid dissociation to reduce the repulsion between the negative charge in the metal and the charge of the deprotonated acids. Positive potentials have the opposite effect. The degree of acid dissociation has an influence on the potential distribution of the interface within the SAM and in the solution part.[45]

Also the pH value changes the degree of dissociation. A higher pH value means a lower concentration of hydrogen ions and therefore more ions dissociate from the carboxyl groups in the PAD to reach equilibrium concentration. Smith and White derived a relation between the chemical state of the film, the pH value of the electrolyte and the interfacial potential using thermodynamic equilibrium conditions[44],

$$\log[\frac{f}{1-f}] = \mathrm{pH} - \mathrm{p}K_\mathrm{a} + \frac{F\Delta V_\mathrm{s}}{2.3RT}, \tag{2.23}$$

where f is the fraction of molecules in the deprotonated state, F is Faraday's constant, R the molar gas constant and T the temperature. For the case that $f = 1/2$, this changes to[44]:

$$\mathrm{p}K_{1/2} = \mathrm{p}K_\mathrm{a} - \frac{F\Delta V_\mathrm{s}}{2.3RT}. \tag{2.24}$$

ΔV_s has to change depending on the pH of the solution with $-59\,\frac{\mathrm{mV}}{\mathrm{decade}}$ to keep the degree of dissociation at $f = 1/2$.

Smith and White also derived an expression for the total interfacial capacitance C_T, which can be separated into three parts: the film capacitance C_F, the solution capacitance C_S and the capacitance due to the acid/base dissociation of the carboxyl groups $C(f)$[44]:

$$\frac{1}{C_\mathrm{T}} = \frac{1}{C_\mathrm{F}} + \frac{1}{C_\mathrm{S} + C(f)}. \tag{2.25}$$

C_F can be modeled as a Helmholtz capacitor with a constant value per interface area, $C_\mathrm{F} = \frac{\epsilon_0 \epsilon_\mathrm{F}}{d}$, where ϵ_0 is the permittivity of free space, ϵ_F the dielectric constant, and d the thickness of the SAM.

The pseudocapacitance $C(f)$ can be expressed as[44]:

$$C(f) = \frac{F^2 \Gamma_\mathrm{T}}{2.3RT} f(1-f), \tag{2.26}$$

where Γ_T is the concentration of SAM molecules.

The dependence of C_T on potential at different pH values is shown in figure 2.21 for a SAM of 4-mercaptopyridine which can pick up a H^+ ion. Similar behavior is described for a SAM containing a carboxyl group by Smith and White[44]. When the pH of the electrolyte is much lower than the pK_a-value, the SAM is fully protonated at all applied potentials. $C(f)$ then goes to zero and the interfacial capacitance C_T depends only on C_S. In this case a capacitance minimum is observed at the PZC of the protonated state when no excess charge carriers are accumulating in the solution close to the interface. When the pH is much higher than the pK_a-value, the SAM is fully deprotonated at all applied potentials during the CV and $C(f)$ goes again to zero. This time a capacitance minimum can be observed at the PZC + $\frac{F\Gamma_T}{C_\mathrm{F}}$, where Γ_T is the sum of the surface concentrations of the protonated and deprotonated molecules.

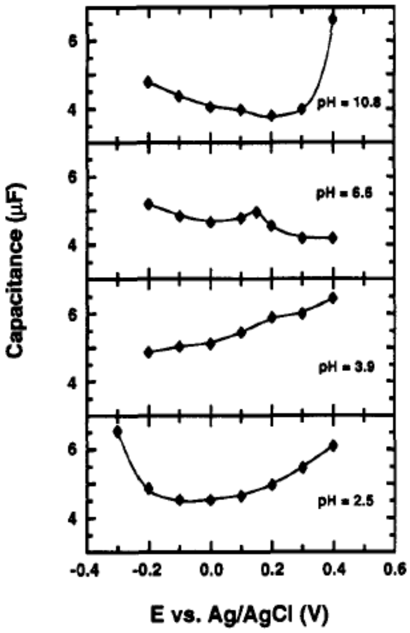

Figure 2.21: Differential capacitance versus potential at different pH values of the electrolyte, measurements performed on Au wire electrodes modified with a 4-mercaptopyridine SAM. Reprinted with permission from[46]. Copyright 1993 American Chemical Society.

The minimum has shifted because the potential difference between the metal and the PAD has changed due to ionization of the PAD. The PAD is now negatively charged which causes a more positive PZC. The difference between the two mimima can be used to estimate C_F[44][46]. If $C_\mathrm{F} << C_\mathrm{S}$, the total capacitance is independent of the applied electrode potential and no minimum can be measured[45]. At pH-values closer to the pK_a-value, $C(f)$ is finite and changes depending on ΔV_s. $C(f)$ has a maximum at the potential where half of the carboxyl groups are ionized[45]. A maximum in C_T appears close to this potential[18][47], but it is often assumed that the maxima are at the same potential[18][45]. This assumption will also be used in this thesis.

In CVs it is possible to find a peak corresponding to the maximum of C_T (figure 2.22). It is assumed that the SAMs are electrochemically inert and do not transport any charge. The only current in a CV is then the current charging the electrode interface[44]. The current is caused by the non-faradaic reaction of protonation and deprotonation of the carboxyl groups. It is a pseudo-capacitive effect but formally similar to a faradaic impedance for a surface-immobilized redox species[18][48]: $I = \nu A C_\mathrm{T}$, where ν is the scan rate in $\frac{\mathrm{V}}{\mathrm{s}}$ and A is the surface area of the sample. The CV curve should therefore show a reversible peak-shaped voltammogramm, with the peak at the maximum of C_T, when $f = 1/2$[45].

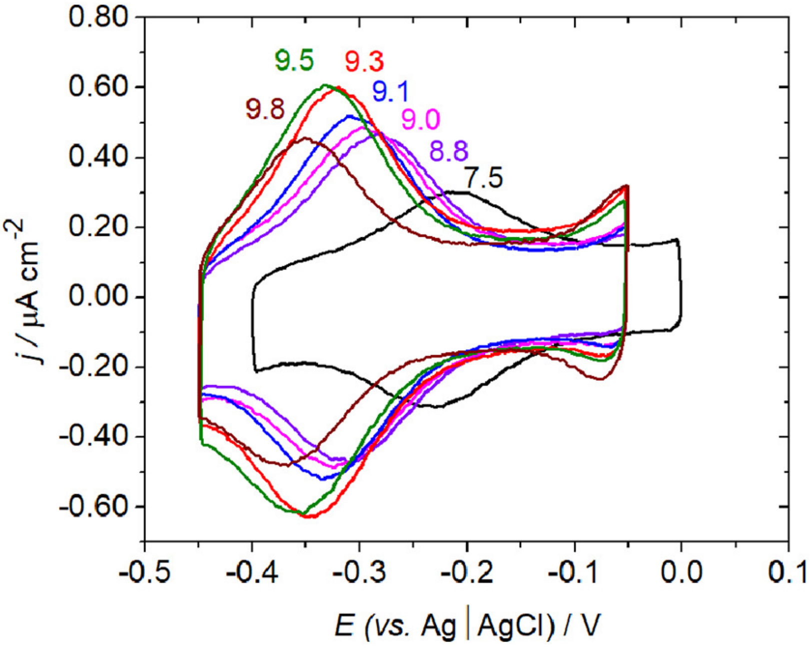

Figure 2.22: CVs of a polycrystalline gold bead electrode coated with a mercaptopropionic acid SAM to show the pH-dependent protonation/deprotonation reaction of MPA. Reprinted with permission from[48]. Copyright 2018 Elsevier B.V.

A fact that can not be explained with the thermodynamic model by Smith and White is the dependence of the maximum peak current on pH (for example visible in figure 2.22). It was assumed that the highest peak in the CV corresponds to p$K_{1/2}$, because similar values had already been reported in literature. There was, however, no theoretical basis for this interpretation[45]. The variation of the peak height indicates a dependence of $\frac{1}{C_\mathrm{S}+C(f)}$ on pH. C_S has a minimum at the PZC of the monolayer covered Au and the peak should be strongest when the PZC equals the potential where half of the acids are dissociated. This is the case at the pK_a where $\Delta V_\mathrm{S} = 0$. When the potential where $f = 1/2$ is far away from the PZC, the film capacity is dominating C_T and almost no peak can be observed.

Burgess et al. developed a kinetic model which describes this effect[18]. They found that the peak is highest at pH 9 for mercaptoundecanoic acid. In their publication, also EIS measurements performed at different potentials for one pH value are presented. At potentials far away from the peak potential in the CV they observed the expected behavior of a series connection of resistor and capacitor with a 90° phase angle at low frequencies. When the potential is close to the peak potential they observed a dip in this frequency regime. The dip is strongest when the applied potential is the peak potential in the CV. At this potential they used an equivalent circuit with the protonation/deprotonation impedance in parallel with the film capacitor. They derived equations for the real and imaginary part of this impedance which also describes the peak in the CV and tested their model with simulations. Their results show that the most pronounced dip in the Bode phase plot appears when the pH is equal to the $\mathrm{p}K_{1/2}$[18].

M. Smiljanić et al.[48] investigated the dependence of the CV curves on the chain length of the mercaptoalkanecarboxylic acids with CV and EIS measurements. They found that the peak in the CV curves is highest around pH = 8.8 for mercaptohexadecanoic acid (the longest SAM molecule they used) and pH = 9.4 for mercaptopropionic acid (the shortest they used). Only a small part of the acids dissociates during the protonation and deprotonation peaks in the CV curves and the amount of charge transferred strongly depends on the chain length. Longer chains lead to smaller peaks. This can be explained if the potential drop ΔV_{F} across the SAM does not depend much on the length of the SAM. The capacitance C_{F} decreases with increasing chain length which leads to a smaller peak height because the charge transferred to or from the electrode in the CV is: $Q_{\mathrm{m}} = C_{\mathrm{F}}\Delta V_{\mathrm{F}}$. Additionally, they observed that the separation of protonation and deprotonation increases with chain length. The dip in the Bode phase plot at potentials close to the peak in the CV (described before) was also observed by Smiljanić et al. It can be seen best for the longest SAM. The frequency of the dip decreases with increasing chain length which indicates slower reaction kinetics and explains the peak separation in the CV.

3 Experimental

3.1 Sample preparation

An AgAu master alloy was prepared by melting Ag and Au in an arc-melter in a ratio of 75at% Ag and 25at% Au. After arc-melting the alloy was homogenized in a sealed glass tube under argon atmosphere at 800 °C over night. It was then rolled in several steps to $170 \pm 10\,\mu\mathrm{m}$ and annealed at 2.2×10^{-5} mbar and 600 °C for one hour. To prove the homogeneity, XRD measurements were performed which showed that there was only one phase present in the alloy. Samples of 50 ± 8 mg were cut from the alloy and contacted using an Au wire which was folded around the sample and then pressed against it. The samples were then dealloyed in an electrochemical cell, using 0.1 M $HClO_4$ as an electrolyte, a curled Pt wire as counter electrode and a commercial Ag/AgCl reference electrode filled with 3M KCl connected to the electrolyte by a KNO_3 salt bridge. For the dealloying process a constant potential of 1.1 V was applied until the current dropped below 50 µA. The primary oxide of the nanoporous samples was then removed by performing a CV in 0.1 M $HClO_4$ between 1.2 V and −0.2 V versus the Ag/AgCl potential.

To modify the samples with SAMs different molecules were used as purchased from SigmaAldrich: 16-mercaptohexadecanoic acid (MHDA, $HS(CH_2)_{15}COOH$) with a purity of >99%, 3-mercaptopropionic acid (MPA, $HS(CH_2)_2COOH$) with a purity >99% and sodium 2-mercaptoethanesulfonate (MESA, $HS(CH_2)_2SO_2ONa$) with a purity >98%. The molecules are shown in figure 3.1. MPA and MHDA have the same functional group (COOH) and were chosen to investigate the influence of the chain length on the capacitance, point of zero charge and protonation/deprotonation reaction, whereas MESA has a different functional group (SO_2OH) to see the influence of the functional group on the capacitance and point of zero charge. MPA and MESA were dissolved in pure distilled water, whereas MHDA was dissolved in a solution of 90% ethanol and 10% acetic acid due to its low polarity and insolubility in water. In this case, to avoid the presence of water in the nanoporous sample it was placed in a vacuum recipient which was pumped to about 10^{-5} mbar before immersing it in the solution containing MHDA. Concentrations of SAMs in solution and immersion times of the samples are listed in table 3.1. 5 ml of the solutions were used to create the SAMs.

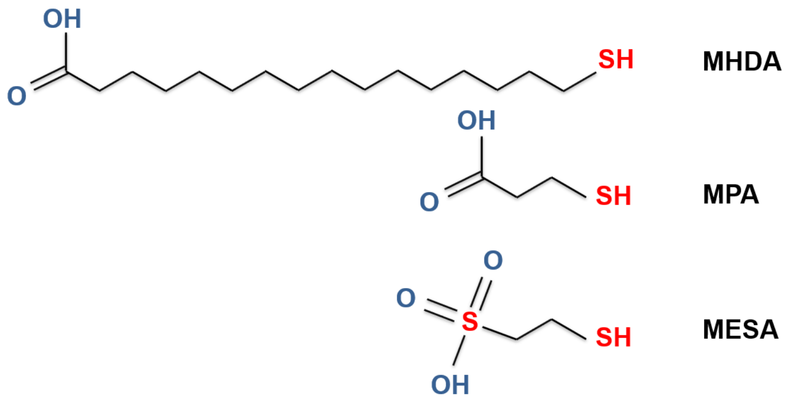

Figure 3.1: Molecules used to create the SAMs.

Table 3.1: List of the samples: m is the mass of the alloy before deallyoing, t_{SAM} the immersion times of the samples in the SAM solution and n the concentration of the SAM molecules in the solution.

	m / mg	SAM	t_{SAM} / h	n / mmol/l	comment
Sample 1	50.8	-	-	-	test measurements
Sample 2	52.5	-	-	-	-
Sample 3	50.1	MHDA	26	6.2	-
Sample 4	45.4	MESA	47	6.0	-
Sample 5	52.7	MESA	42	7.9	-
Sample 6	56.5	MPA	66	5.7	-
Sample 7	58.2	MHDA	90	5.5	-
Sample 8	56.3	MHDA	65	5.0	-
Sample 9	56.9	MHDA	145	5.4	-
Sample 10	57.8	MHDA	73	5.0	-
Sample 11	55.2	-	-	-	-
Sample 12	53.8	-	-	-	test measurements
Sample 13	53.4	MHDA	90	5.2	test measurements
Sample 14	55.0	MPA	66	5.7	test measurements
Sample 15	48.1	MPA	67	5.7	-

3.2 Electrochemical Measurements

A Metrohm Autolab PGSTAT128N potentiostat controlled by the software NOVA was used to perform all electrochemical measurements and record the data. Again, a

Ag/AgCl reference electrode filled with 3M KCl connected by a KNO_3 salt bridge was used in all the measurements relative to which all potentials $U_{\mathrm{Ag/AgCl}}$ will be stated in the following. Curled Pt wires or carbon cloths were used as counter electrodes depending on the experiment. A schematic representation is shown in figure 3.2 with the working electrode WE, the reference electrode RE, and the counter electrode CE. Also included are the pH-electrode pH-E and the magnetic stirrer which are only used in the measurements for the protonation/deprotonation reaction.

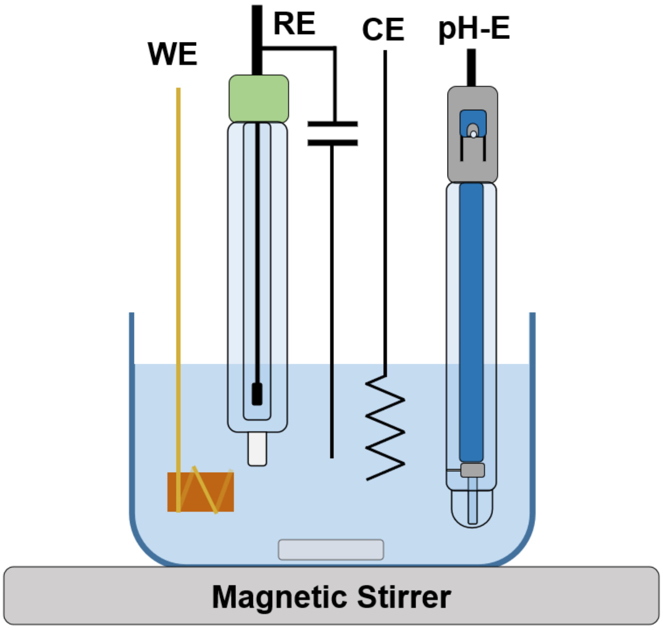

Figure 3.2: Schematic representation of the experimental setup for the electrochemical measurements with the working electrode (WE), the reference electrode (RE) with additional capacitance in parallel during EIS measurements, the counter electrode (CE), the pH-electrode (pH-E) and the magnetic stirrer with stirring bar.

3.2.1 Determination of the Point of Zero Charge

To determine the PZC, EIS measurements were performed at different applied potentials on untreated npAu and on npAu modified with SAMs. 10 mM or 0.1 M $HClO_4$ was used as electrolyte and a curled Pt wire as counter electrode. To avoid unwanted features caused by the RE at high frequencies in the EIS data, a capacitor was placed in parallel with the Ag/AgCl reference electrode and connected via a Pt wire to the electrolyte. The capacitor reduces the impedance of the reference electrode at high frequencies[43]. The applied frequencies for the EIS measurements were between 100 kHz and 1 mHz. The potential was varied only within the limits of the double layer regime for which it could be assumed that no desorption of SAM molecules takes place. The experimental parameters are listed in table 3.2.

Table 3.2: Sample list with experimental parameters for EIS measurements to determine the point of zero charge, n is the concentration of $HClO_4$ in the electrolyte and t_{imm} is the immersion time in the electrolyte before the measurement was started, t_{wait} is the waiting time after measuring the OCP before the 1st EIS measurement.

	SAM	n / mM	OCP / $U_{\mathrm{Ag/AgCl}}$	t_{imm}	t_{wait} / min
Sample 2	-	10	not determined	24 h	1
Sample 3	-	10	+ 0.66	36 min	1
Sample 3	MHDA	10	+ 0.25	21 min	30
Sample 4	-	10	+ 0.61	21 h	1
Sample 4	MESA	10	+ 0.18	44 min	10
Sample 5	-	100	+ 0.59	21 h	1
Sample 5	MESA	10	+ 0.25	2 h	1
Sample 6	MPA	10	+ 0.24	2 h	10

3.2.2 Protonation/Deprotonation of the SAM

To measure the protonation and deprotonation of a SAM, CV curves with 3 mV/s or 5 mV/s were recorded in the double layer regime on untreated npAu sample 11, sample 8 modified with MHDA, and sample 15 modified with MPA. A carbon cloth was used as counter electrode and 0.1 M NaCl as electrolyte with an initial pH of about 5.5 which was then adjusted by adding 0.1 M or 10 mM NaOH or HCl. The EIS measurements listed in table 3.3 were performed at a constant pH at different potentials with a curled Pt wire as counter electrode and the capacitor in parallel with the reference electrode. The pH was measured using a BlueLine pH-electrode with platinum wire junction and liquid electrolyte by SI analytics in combination with a WTW Pocket pH-meter pH 3110 single device. To ensure equal distribution of ions in the setup, the electrolyte was stirred with a magnetic stirrer at 300 rpm or 500 rpm at the beginning and every time the pH was adjusted. The magnetic stirrer was turned off and the stir bar removed from the cell 5 minutes before the measurement was started.

Table 3.3: Sample list with experimental parameters for EIS measurements to observe protonation/deprotonation reactions in 0.1 M NaCl, t_{imm} is the immersion time in the electrolyte before the measurement was started.

	SAM	pH	OCP / V vs Ag/AgCl	t_{imm} / h
Sample 9	MHDA	9.5	+ 0.28	80
Sample 10	MHDA	9.0	+ 0.14	8

4 Results

In the following chapter the results of the different measurements are presented. At the beginning, the EIS measurements performed in the double layer regime in 10 mM $HClO_4$ on untreated npAu are compared to the EIS measurements on npAu modified with different SAMs. Graphical methods as well as EEC fits are used. Then, the EIS measurements are used to gain information about the interfacial capacitance at different potentials in the double layer regime by fitting the data with EECs and by calculations of C_{eff}. The dependence of the capacitance on applied potential is used to find the PZC. Finally, the CV and EIS measurements performed on npAu modified with MHDA or MPA in 100 mM NaCl are presented to show the protonation/deprotonation reaction of the carboxyl groups. The pH of the NaCl-solution is adjusted with 100 mM NaOH or HCl to see the influence of pH on protonation/deprotonation reaction.

4.1 EIS measurements

EIS measurements are performed between 100 kHz and 1 mHz on sample 2 (untreated npAu), sample 3 modified with MHDA, sample 6 with MPA, and sample 5 with MESA in the double layer regime at +150 mV. In the double layer regime the interface is in its blocking state and purely capacitive behavior is expected in the low-frequency limit. Graphical methods and EEC fits are applied to see the differences of the EIS data recorded on different samples. To graphically compare the data measured on untreated npAu and on samples modified with a SAM, the Nyquist plots, Bode phase plots, Bode modulus plots and plots of Z_{im} versus f and C_{eff} versus f are used.

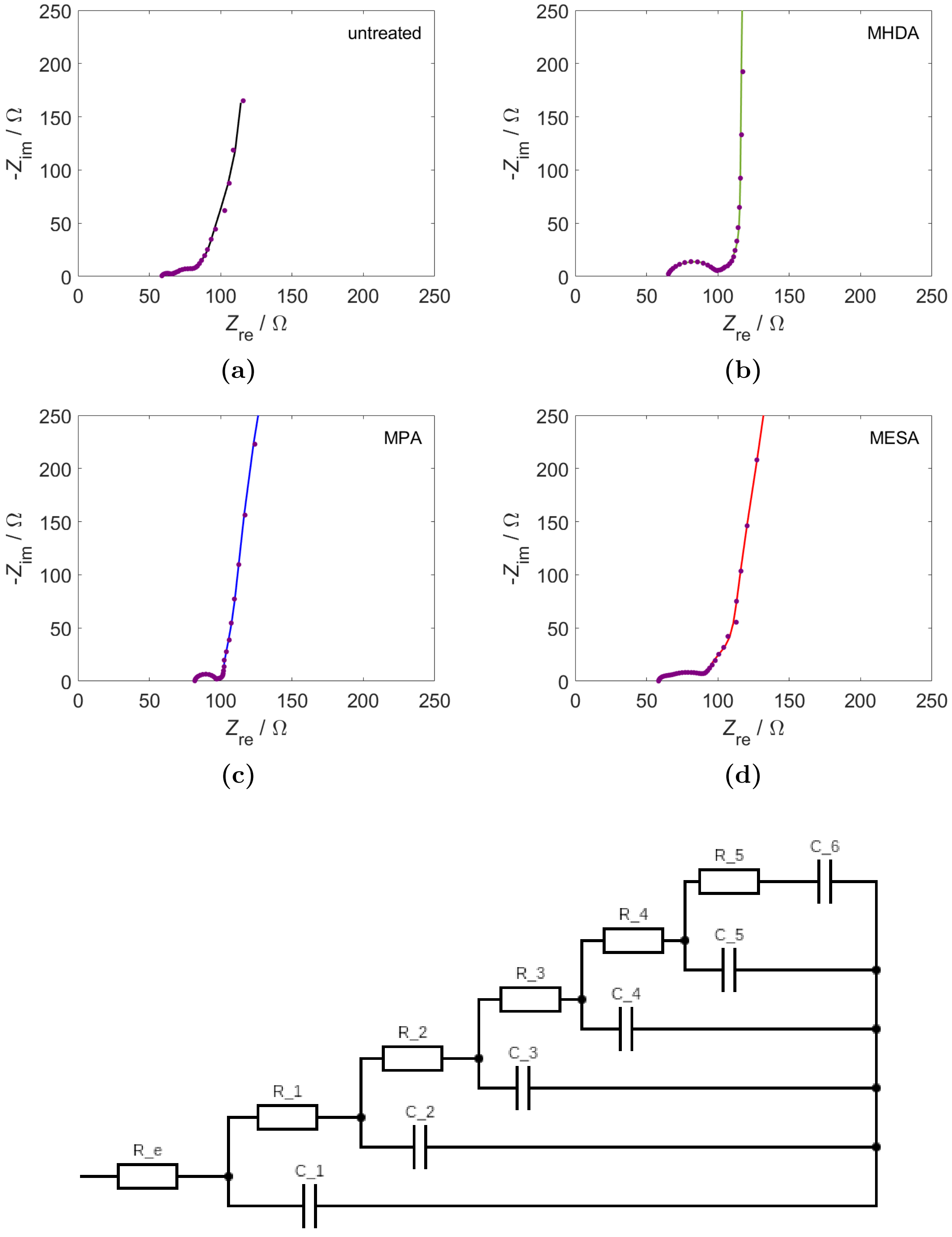

(a) (b) (c) (d) (e)

Figure 4.1: Nyquist plots of measured EIS data (●) and fit between 100 kHz and 14 mHz at +150 mV in 10 mM $HClO_4$: (a) untreated npAu (—), (b) npAu modified with MHDA (—), (c) npAu modified with MPA (—), (d) npAu modified with MESA (—). (e) Equivalent electrical circuit according to the theory of de Levie[40] and Keiser[41] with 5 RC elements. The fitted values are listed in table 4.1.

Table 4.1: Values of the EEC fits with 5RC elements for different samples at +150 mV in 10 mM $HClO_4$ between 100 kHz and 14 mHz. EIS data and fits are shown in figure 4.1.

	Sample 2	Sample 3	Sample 6	Sample 5
SAM	-	MHDA	MPA	MESA
R_e / Ω	59.0 ± 0.2	65.3 ± 0.2	82.0 ± 0.1	58.7 ± 0.2
R_1 / Ω	6.6 ± 0.3	23 ± 1	12.8 ± 0.4	11.0 ± 0.4
C_1 / µF	13 ± 1	1.68 ± 0.07	8.4 ± 0.3	12.0 ± 0.8
R_2 / Ω	6.3 ± 0.7	11 ± 1	2.7 ± 0.4	13.8 ± 0.6
C_2 / µF	$(48 \pm 8) \cdot 10$	9 ± 2	$(14 \pm 5) \cdot 10$	$(13 \pm 1) \cdot 10$
R_3 / Ω	12.5 ± 0.8	13.3 ± 0.9	6.1 ± 0.3	11.0 ± 0.6
C_3 / mF	2.4 ± 0.3	0.41 ± 0.04	3.5 ± 0.3	1.7 ± 0.2
R_4 / Ω	40 ± 7	76 ± 16	$(28 \pm 3) \cdot 10$	69 ± 5
C_4 / mF	27 ± 2	1.6 ± 0.1	16.2 ± 0.3	15.6 ± 0.6
R_5 / Ω	$(40 \pm 8) \cdot 10$	$(53 \pm 11) \cdot 1000$	$(38 \pm 2) \cdot 100$	$(22 \pm 4) \cdot 100$
C_5 / mF	28 ± 2	0.9 ± 0.1	4.7 ± 0.1	19.4 ± 0.6
C_6 / mF	17 ± 2	0.12 ± 0.02	5.0 ± 0.4	6 ± 1

Figures 4.1a to 4.1d show the Nyquist plots for graphical analysis of untreated npAu and npAu modified with MHDA, MPA or MESA. The EIS data are fitted using the NOVA software with EECs according to the theory of de Levie[40] and Keiser[41] consisting of the electrolyte resistance and 5 RC elements (figure 4.1e), as described in section 2.3.2. The values of all the fits are listed in table 4.1.

In the Nyquist plots of all the different samples, a semicircle appears in the high-frequency regime. As described in section 2.3.2, this semicircle is caused by the Au wire; the RC elements corresponding to this semicircle are not included in the calculations of interfacial capacitance C and pore resistance R_{pore} of the samples. For untreated npAu (figure 4.1a), the first semicircle ($R \approx 7\,\Omega$, $f_{\text{ch}} =\approx 1600\,\text{Hz}$, $C = \frac{1}{2\pi f R} \approx 14\,\mu\text{F}$) has an almost perfect shape and seems to correspond to the first RC element (R_1 and C_1 of sample 2 in table 4.1). An additional semicircle can be seen at lower frequencies with $R \approx 16\,\Omega$ which is close to the sum of the resistances of the 2nd and 3rd RC element. For the samples modified with MHDA (figure 4.1b) or MPA (figure 4.1c), the sum of the resistances of the first two RC elements agrees well with the diameter of the semicircle ($R \approx 35\,\Omega$ for MHDA and $R \approx 15\,\Omega$ for MPA). For the sample modified with MESA (figure 4.1d), the semicircle is more depressed and it is not so easy to determine a diameter. However, the diameter seems to be approximately the sum of the resistances of the first three RC elements. The values of C and R obtained by the EEC fit are listed together with the fit quality χ^2 in table 4.2. The values for C are related to the mass of Au in the sample and given in mF/mg. The very feature-rich shape of the untreated sample and the sample modified with MESA is probably the reason for the lower fit quality.

Table 4.2: Interfacial capacitance C, pore resistance R_{pore} and fit quality χ^2 for different samples at +150 mV in 0.1 M $HClO_4$ between 100 kHz and 14 mHz from EEC fit with 5RC elements. The EEC is shown in figure 4.1e and the fitted elements are listed in table 4.1.

	SAM	C / mF/mg	ΔC / mF/mg	R_{pore} / Ω	ΔR_{pore} / Ω	χ^2
Sample 2	-	4.3	0.3	460	80	0.0027
Sample 3	MHDA	0.16	0.01	53000	11000	0.0012
Sample 6	MPA	1.36	0.06	4100	250	0.0003
Sample 5	MESA	2.1	0.1	2300	400	0.0023

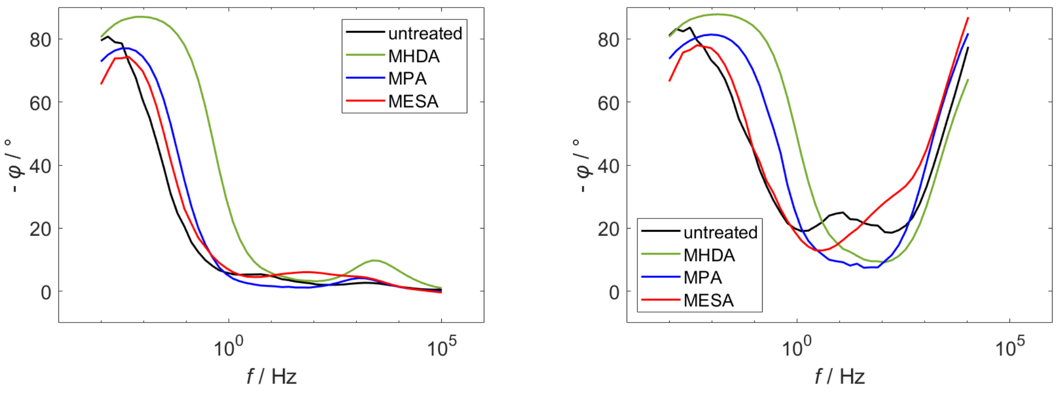

(a) (b)

Figure 4.2: Bode phase plots of the EIS data of untreated npAu (—), modified with MHDA (—), MPA (—) or MESA (—) recorded at +150 mV in 10 mM $HClO_4$ between 100 kHz and 1 mHz : (a) uncorrected data, (b) corrected with R_e from the EEC fit (see table 4.1).

The Bode phase plots of the different samples are shown in figure 4.2a. They qualitatively show the expected behavior for a sample with several RC elements in its blocking state. However, none of the samples reaches 90° at low frequencies, which would indicate ideal capacitive behavior. The sample modified with the long-chained MHDA is closest to 90° and also the untreated npAu and the sample modified with the short-chained MPA reach phase angles above 80°. The sample modified with MESA has the lowest phase angle. At the lowest measured frequencies the phase decreases again which indicates some kind of charge transfer. For the untreated npAu and the sample modified with MESA features appear in the middle-frequency regime similar to the effects already seen in the Nyquist plots (figures 4.1a and 4.1d). The features can be seen even better in the corrected Bode phase plots in figure 4.2b which are calculated using the value of R_e from the EEC fit. At high frequencies the corrected curves increase towards 90° but they do not converge. The highest measured frequencies are not plotted due to the fluctuations of Z_{re} which strongly influence φ when $Z_{re} \approx R_e$ according to equation 2.18 ($\varphi = \tan^{-1}(\frac{Z_{im}}{Z_{re}-R_e})$).

In the corrected Bode modulus plot (figure 4.3a) and the plot of Z_{im} (figure 4.3b) and their derivatives (figures 4.3c and 4.3d), the sample closest to the ideal capacitance is again the sample modified with MHDA. In both plots of the derivative it is stable at a value very close to -1 at low frequencies. The samples with MESA and MPA reach approximately -0.94. The sample with MESA fluctuates strongly whereas the sample with MPA is almost constant in a wide range of frequencies. The untreated npAu sample does not seem to converge to any value at low frequencies and has even more negative slopes than -1 at the lowest measured frequencies.

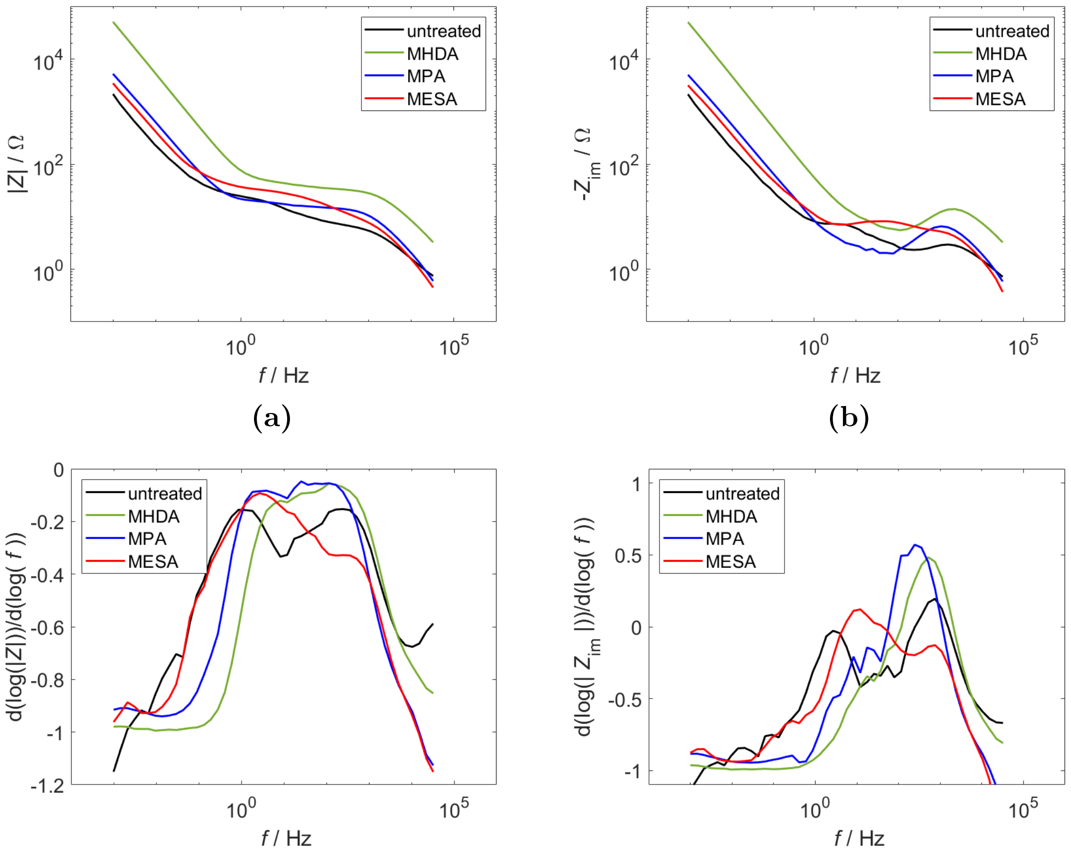

(a) (b)

(c) (d)

Figure 4.3: EIS data recorded at +150 mV in 10 mM $HClO_4$ between 100 kHz and 1 mHz on untreated npAu (—), modified with MHDA (—), MPA (—) or MESA (—): (a) Bode modulus plots corrected with R_e from the EEC fit (table 4.1), (b) Z_{im} versus f, (c-d) derivatives of (a) and (b).

Two different methods are used to obtain values for the capacitance of the samples. The effective capacitance C_{eff} is compared to the values achieved by the EEC fit (table 4.2). In the low-frequency regime a plateau appears for C_{eff} as expected for an electrode in its blocking state. These values agree well with the values of the EEC fit. At the lowest frequencies C_{eff} slightly deviates from the plateau indicating the onset of charge transfer.

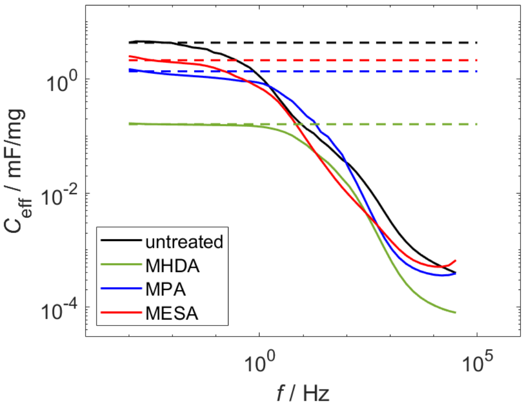

Figure 4.4: Effective capacitance C_{eff} versus frequency f of the EIS data recorded at +150 mV in 10 mM $HClO_4$ between 100 kHz and 1 mHz on untreated npAu (—), modified with MHDA (—), MPA (—) or MESA (—). The C-values from the EEC fits (see table 4.2) are indicated by dashed lines.

4.2 Point of Zero Charge

Knowledge about the charge accumulating at the interface between an electrode and an electrolyte is very important for enzyme immobilization since it can be used to create an electrostatic bond. In this part the point of zero charge (PZC) of untreated npAu and npAu modified with different SAMs is determined to investigate the influence of a SAM on the charge accumulating at the interface. The PZC is the electrode potential at which no excess charge is accumulating on the electrode side and on the electrolyte side of the interface. It can be determined via the double layer capacitance C_{dl}, which has a minimum at the PZC. To investigate the dependence of C_{dl} on potential, EIS measurements are performed in a frequency range from 100 kHz to 1 mHz at different applied potentials. Values of the capacitance C are then obtained by EEC fit and C_{eff}-calculations at frequencies where C is dominated by C_{dl}. The values of the two methods are compared and minima of C are determined, which are at the PZC.

To find the frequency regime for the determination of the PZC, the EIS measurements in the double layer regime at +150 mV are used again. This time the Bode modulus plots without correction for the ohmic electrolyte resistance are plotted in figures 4.5a to 4.5e. Two linear regimes can be observed in all the Bode modulus plots in their logarithmic form. A steep decrease at low frequencies f is followed by an almost flat regime at higher frequencies. As described in section 2.3.2, the intersection of these two linear regimes gives the frequency constant f_C below which the total interfacial capacitance C is dominated by C_dl [39]. The frequency constants of sample 2 (untreated npAu), sample 3 modified with MHDA, sample 6 with MPA and sample 5 with MESA are listed in table 4.3.

Table 4.3: Frequency constants f_C from figure 4.5 for PZC determination.

	SAM	Electrolyte	f_C / Hz
Sample 2	-	10 mM $HClO_4$	0.02
Sample 3	MHDA	10 mM $HClO_4$	0.49
Sample 6	MPA	10 mM $HClO_4$	0.07
Sample 5	MESA	10 mM $HClO_4$	0.05
Sample 5	-	100 mM $HClO_4$	0.16

For each applied frequency the effective capacity C_eff is calculated. C_eff versus frequency for the different samples is shown in figure 4.6. At high frequencies C_eff depends strongly on the frequency, whereas at low frequencies a plateau can be observed in the logarithmic plot. Deviation from the plateau at the lowest frequencies can be seen especially for the untreated npAu (sample 2, figure 4.6a) and sample 3 modified with MHDA (figure 4.6b). For sample 6 modified with MPA (figure 4.6c), sample 5 modified with MESA (figure 4.6d) and the untreated npAu in 0.1 M $HClO_4$ (sample 5, 4.6e) this increase is much smaller. The vertical line in each of the plots of C_eff versus frequency marks f_C determined from the Bode modulus plots in figure 4.5 and listed in table 4.3. f_C lies in the plateau regime of C_eff for all the samples. Values for C are taken from C_eff at frequencies lower than f_C since C_eff is dominated by C_dl at these frequencies. The lowest measured frequencies are not used to avoid the influence of charge transfer. The measured data are then fitted with an EEC using the NOVA software. C-values are calculated from the EEC as the sum of the capacitors (equation 2.22). Again, the capacitors involved in the creation of the high-frequency semicircle are not included in this sum. The C-values found by the EEC fit are compared to the values obtained from C_eff in sections 4.2.1 and 4.2.2.

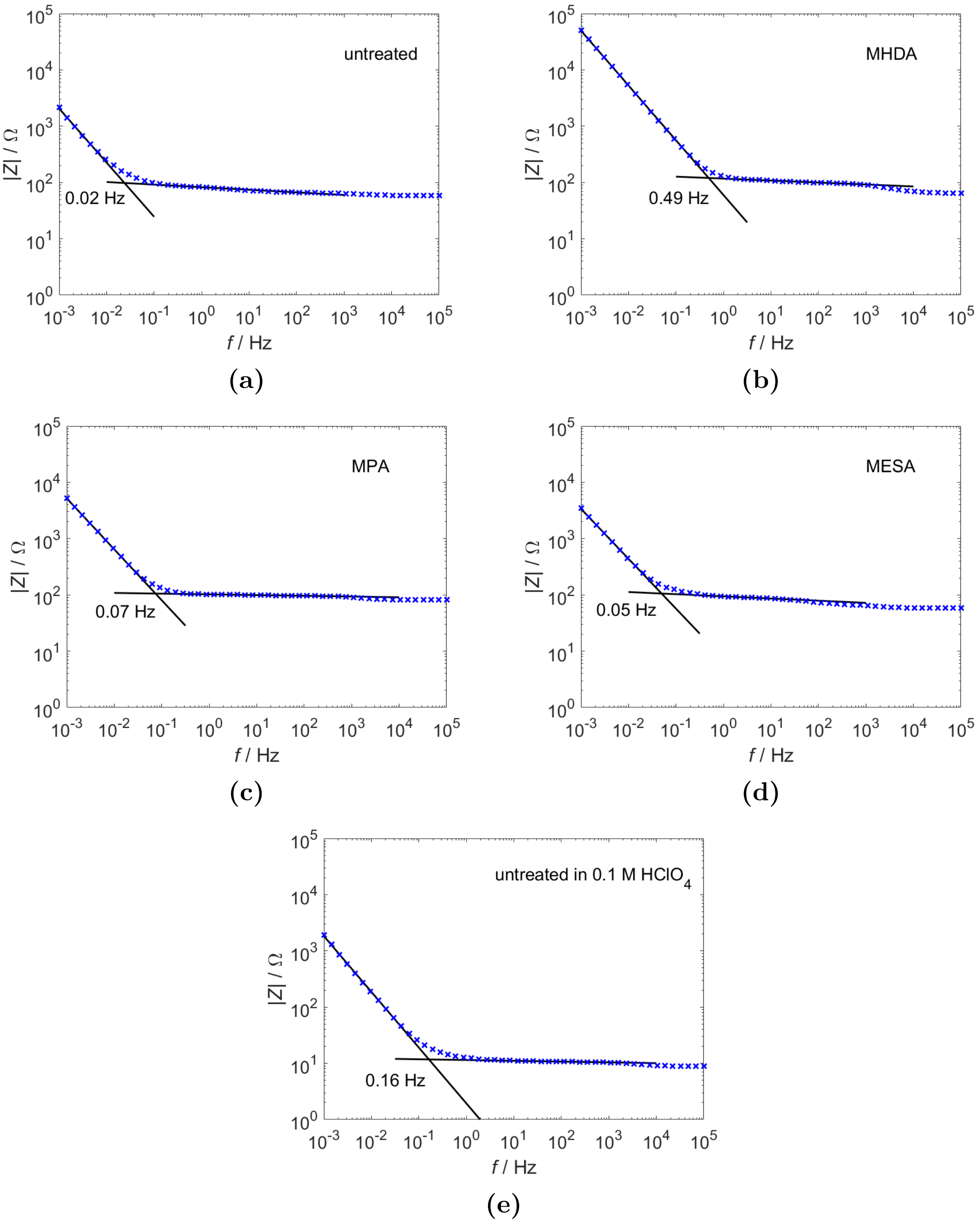

(a) (b) (c) (d) (e)

Figure 4.5: Bode modulus plots of the EIS data in the frequency range between 100 kHz and 1 mHz at +150 mV (×) and fits in linear regimes (—). The interception gives f_C: (a) untreated npAu sample 2 , (b) sample 3 modified with MHDA , (c) sample 6 modified with MPA , (d) sample 5 modified with MESA all in 10 mM $HClO_4$, (e) untreated npAu sample 5 in at +100 mV in 0.1 M $HClO_4$.

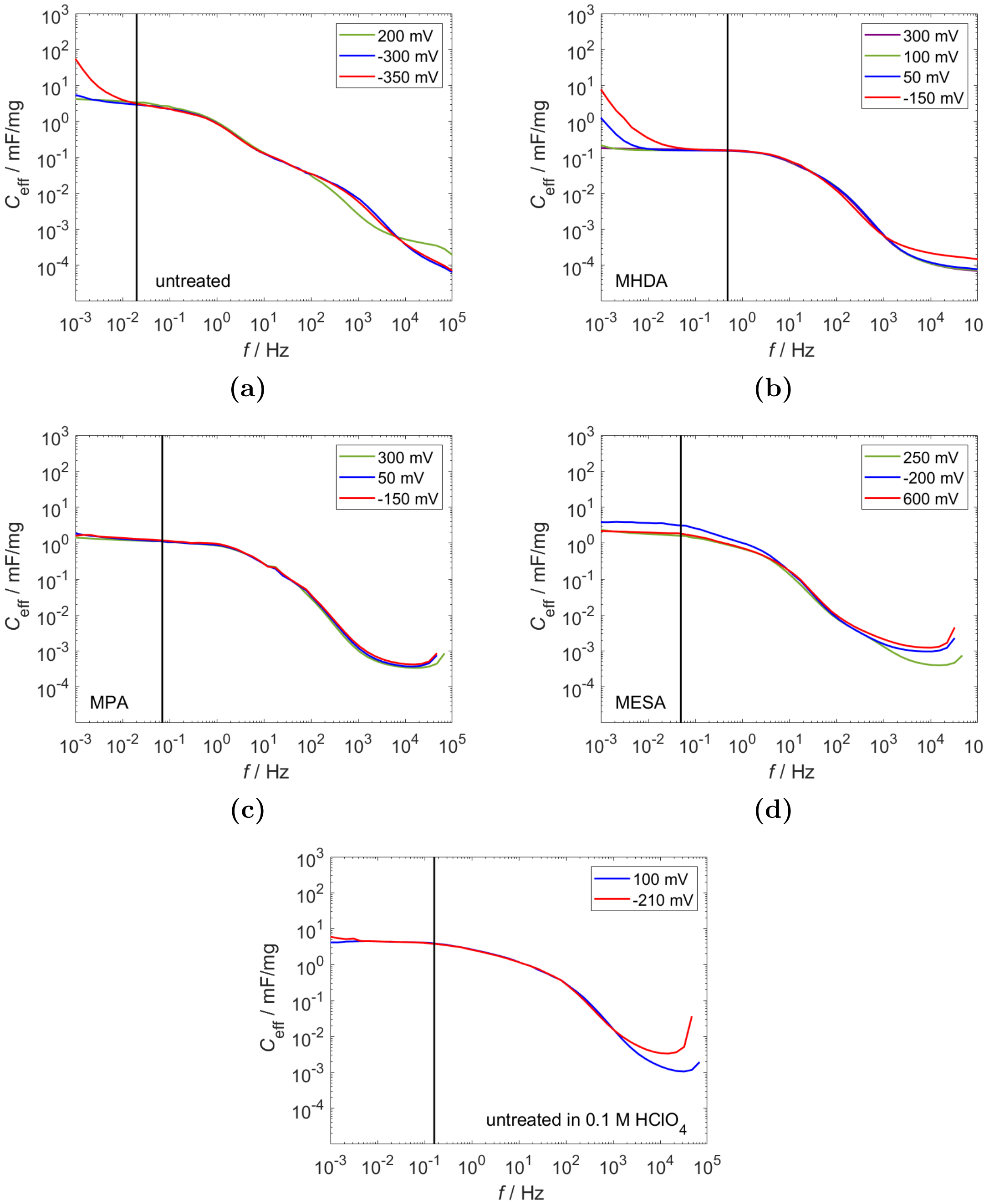

(a)

(b)

(c)

(d)

(e)

Figure 4.6: C_{eff} of npAu dependent on frequency f at different potentials: (a) untreated npAu sample 2, (b) sample 3 modified with MHDA, (c) sample 6 modified with MPA, (d) sample 5 modified with MESA all in 10 mM $HClO_4$, (e) untreated npAu sample 5 in 0.1 M $HClO_4$. Vertical lines indicate f_C determined from the Bode modulus plots figure 4.5 and listed in table 4.3.

4.2.1 Untreated npAu

To find the PZC of untreated npAu, EIS measurements in 10 mM $HClO_4$ are performed between +200 mV and −450 mV on sample 2. The measurements at potentials more negative than −350 mV show a strong deviation of C_{eff} from the plateau at f_C (figure 4.6a) and are therefore not used in the calculations. The increase of C_{eff} at the lowest measured frequencies is already visible at −300 mV but it only seems to start at frequencies much lower than f_C. The dependence of C on applied potential is shown in figure 4.7 for the EEC fit with 5 RC-elements down to 14 mHz (×) and for the single frequency PZC calculation with C_{eff} at 5 mHz (—) and 14 mHz (—). The values of the two methods are of the same magnitude and a variation of the capacitance with potential can be seen. Interestingly, the C-value from the EEC fit is much higher at −300 mV whereas C taken from C_{eff}-calculations stays low for the selected frequencies. It seems like the onset of charge transfer is visible in the EEC fit but not in C_{eff} at comparable frequencies. At −350 mV C increases also for the C_{eff}-calculations due to charge transfer. The C-value obtained via EEC fit at −350 mV is much higher and therefore not shown in the plot. There is no minimum in the double layer regime where a linear decrease of C towards more cathodic potentials can be seen especially for the C-values taken from C_{eff}.

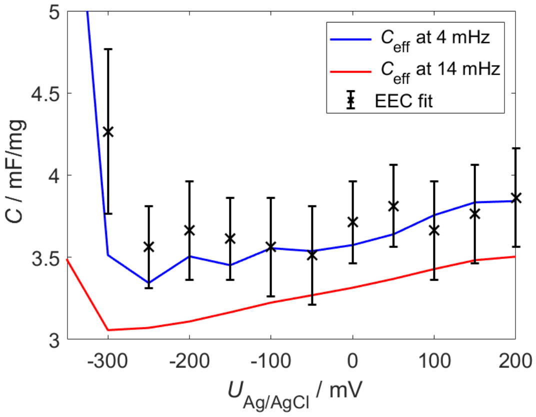

Figure 4.7: Interfacial capacitance C of sample 2 in 10 mM $HClO_4$ at different applied potentials $U_{\text{Ag/AgCl}}$: C-values taken from C_{eff} at 5 mHz (—) and 14 mHz (—) and values from the EEC fit (down to 14 mHz with 5 RC-elements, ×).

The same measurements are performed on sample 5 in 0.1 M $HClO_4$ (figure 4.8b). To avoid the influence of charge transfer at cathodic potentials, no measurements are done below −210 mV. C_{eff} as a function of frequency is plotted in figure 4.6e. Additionally, C is calculated doing CV scans with different sweep rates ν according to $C = \frac{I(\nu)}{\nu}$ where the current $I(\nu)$ is taken as the average of cathodic and anodic current at +100 mV. C_{eff}-calculations at 43 mHz (— in figure 4.8b) and 133 mHz

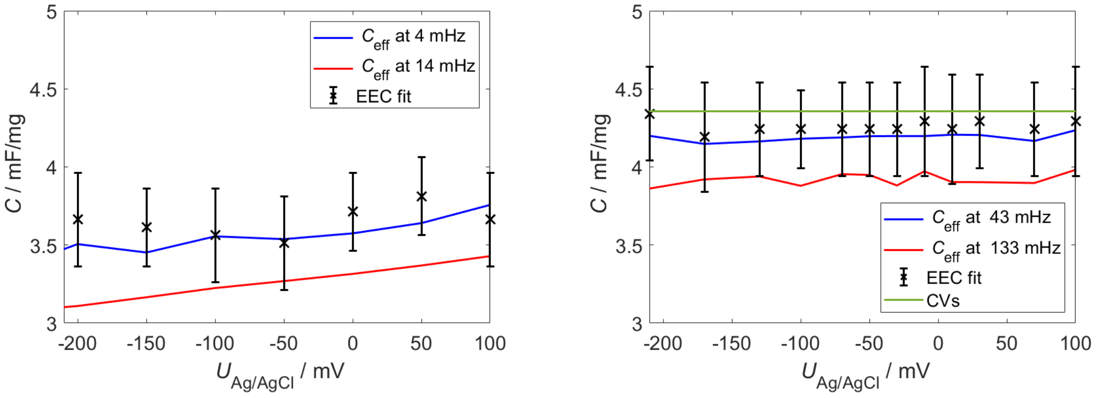

(a) **(b)**

Figure 4.8: Interfacial capacitance C of npAu at different applied potentials $U_{\mathrm{Ag/AgCl}}$ in different electrolyte concentrations: (a) Data of figure 4.7 in a smaller potential range: Sample 2 in 10 mM $HClO_4$. (b) Sample 5 in 0.1 M $HClO_4$: C-values taken from C_{eff} at 43 mHz (—) and 133 mHz (—), values from the EEC fit (down to 43 mHz with 5 RC-elements, ✕) and the value calculated doing CV scans (—).

(—) and the capacity of the EEC fit with 5 RC-elements down to 43 mHz (✕) give very similar results and are close to the value calculated with the CVs (—). For comparison of the measurements in the different electrolyte concentrations, the same measurement in 10 mM $HClO_4$ as in 4.7 is shown again in figure 4.8a in the smaller potential range. The capacitance in 0.1 M $HClO_4$ (figure 4.8b) is clearly higher and seems to be almost independent of potential whereas the capacitance in 10 mM $HClO_4$ (figure 4.8a) changes slightly with potential.

4.2.2 npAu modified with SAMs

In the EIS spectra recorded on sample 3 modified with MHDA a big semicircle at low frequencies can be seen in the Nyquist plot for some potentials (figure 4.9). This is caused by charge transfer reactions at the electrode electrolyte interface. These reactions also influence C_{eff} as shown in figure 4.6b, where the value of C_{eff} increases again at low frequencies after reaching a plateau at intermediate frequencies. The increase gets bigger at more cathodic potentials. f_{C} coincides with the plateau region of C_{eff} and a frequency a bit lower than f_{C} is used to find the dependence of C on potential. The result is shown in figure 4.10a for a frequency of 133 mHz. For this sample a minimum at about +100 mV can be seen.

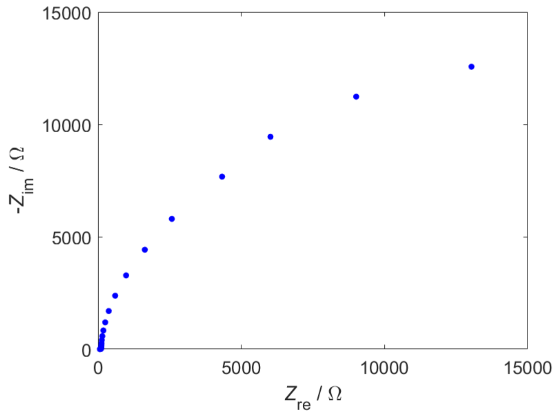

Figure 4.9: Nyquist plot of sample 3 modified with MHDA in 10 mM $HClO_4$ at −50 mV between 100 kHz and 1 mHz.

Good agreement between C-values originating from the EEC fit (×) and values calculated via C_{eff} (—) can be seen if the lower frequency limit of the EEC fit is higher than the single frequency used to obtain C-values from C_{eff} (figure 4.10b). In figure 4.10b, the EEC fit down to 133 mHz shows a strong increase of C at negative potentials due to the onset of charge transfer. When taking C-values from C_{eff} this increase can not be seen at 133 mHz (figure 4.10a) but at lower frequencies, such as 20 mHz (figure 4.10b). This is similar to the observations on untreated npAu in 10 mM $HClO_4$ (figure 4.7). The curve in figure 4.10a can also be observed in EEC fits when only frequencies down to 600 mHz are used for the fit. However, the C-values from the EEC fits then have very large error bars due to the low number of data points and are therefore not shown.

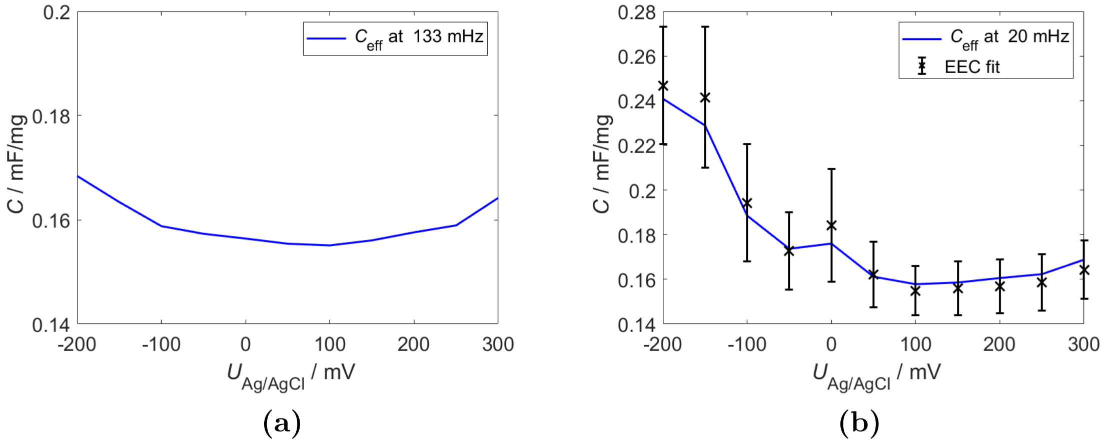

(a) (b)

Figure 4.10: Interfacial capacitance C of sample 3 modified with MHDA in 10 mM $HClO_4$ dependent on potential $U_{\mathrm{Ag/AgCl}}$:(a) C-values taken from C_{eff} at 133 mHz (—), (b) C-values taken from C_{eff} at 20 mHz (—) and capacitance values from EEC fit down to 133 mHz with 5 RC-elements (×). Different ranges are used on the y-axis to show the minimum in (a).

The capacitance values calculated for sample 6 modified with MPA are shown in figure 4.11. C-values are taken from C_{eff} (figure 4.6c) at 20 mHz (— in figure 4.11) and an EEC fit with four RC-elements is done including frequencies down to 43 mHz (×). Again, good agreement between the C-values obtained by the two methods can be seen. C is higher at negative potentials and it is lowest at +150 mV to +250 mV.

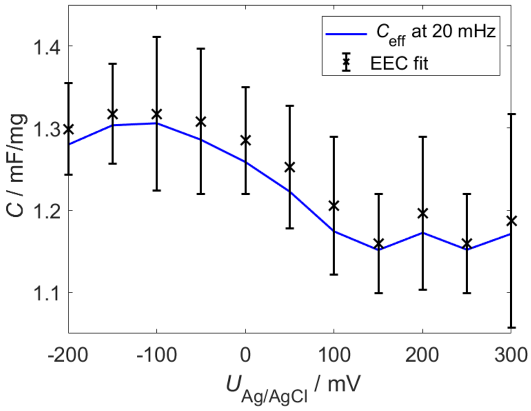

Figure 4.11: Interfacial capacitance C of sample 6 modified with MPA in 10 mM $HClO_4$ dependent on potential $U_{\mathrm{Ag/AgCl}}$. C-values taken from C_{eff} at 20 mHz (—) and capacitance from the EEC fit down to 43 mHz using 4 RC-elements (×).

The results of the EIS measurements on sample 5 modified with MESA are shown in figure 4.12 with EEC fits down to 14 mHz. The EEC fits (×) are in very good agreement with C_{eff} (figure 4.6d) recorded at 14 mHz (— in figure 4.12). The dashed line with the arrow connecting the two data points should indicate the chronological order of the measurements. The first measurement is performed close to the OCP at +250 mV. The potential is then decreased in steps of −50 mV. After the EIS measurement at −200 mV the potential is set again to +250 mV and then increased up to +600 mV. The data point at +250 mV recorded after the point at −200 mV is not shown in this plot, because it is much higher than the value recorded at the beginning at +250 mV and exceeds the limits of the plot. A small minimum can be seen around +500 mV.

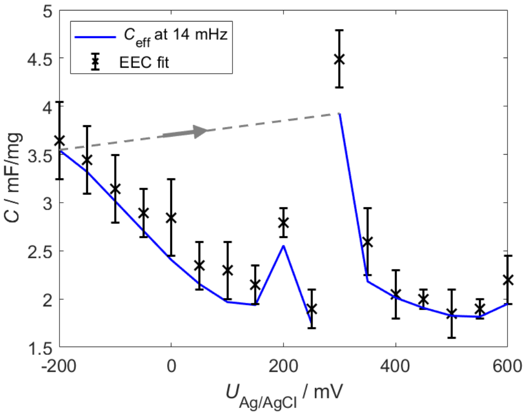

Figure 4.12: Interfacial capacitance C of sample 5 modified with MESA in 10 mM $HClO_4$ dependent on potential $U_{\mathrm{Ag/AgCl}}$. C-values taken from C_{eff} at 14 mHz (—). The dashed line with the arrow indicates the chronological order of the measurements. Capacitance from the EEC fit (×) down to 14 mHz using 6 RC-elements from +250 mV to −200 mV and 5 RC-elements from +300 mV to +600 mV.

The number of RC elements used in the EEC fit for sample 5 modified with MESA is not the same for all potentials. The spectra recorded from +250 mV to −200 mV all have a depressed semicircle consisting of several overlapping semicircles in the high frequency regime (figure 4.1d). In section 4.1, three RC elements are used in the fit to form such a semicircle. In the measurements performed after switching the potential from −200 mV to +250 mV a less depressed semicircle appears at high frequencies, which is formed by only two RC elements in the fit. The high-frequency regime of the measurement at +150 mV (—) is plotted again in figure 4.13 together with the measurement recorded later at +350 mV (—) to show the different shapes of the semicircles. The high-frequency semicircle is caused by the Au wire. The RC-elements used to fit it do not contribute to the capacity of the sample. To keep a constant number of three RC-elements to fit the data corresponding to the nanoporous sample, the total number of RC-elements was changed from six to five.

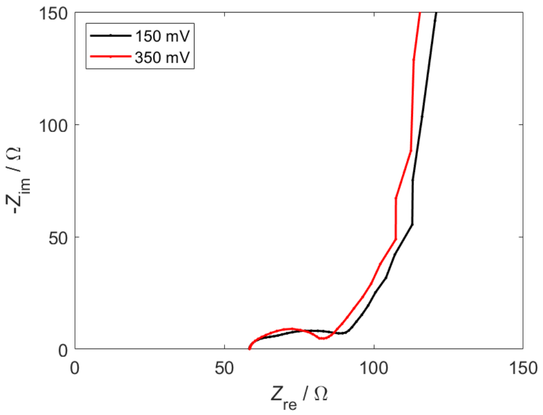

Figure 4.13: High frequency regime of the Nyquist plots of EIS measurements of sample 5 with a MESA SAM in 10 mM $HClO_4$ at +150 mV (—, same as in figure 4.1d) and after several other measurements at +350 mV (—).

The potentials where the minima in interfacial capacitance are found are listed in table 4.4 for the different samples. Only for sample 3 modified with the long-chained MHDA a clear minimum is found (figure 4.10). For the samples modified with the short MPA (figure 4.11) and MESA SAMs (figure 4.12), estimates for the PZC can be made whereas for the untreated npAu samples (figure 4.7 and 4.8) no minimum can be determined.

Table 4.4: Minima of the total interfacial capacitance (PZC) for untreated npAu and with different SAMs

	SAM	Electrolyte	PZC / mV
Sample 2	-	10 mM $HClO_4$	no minimum found
Sample 3	MHDA	10 mM $HClO_4$	+100
Sample 6	MPA	10 mM $HClO_4$	≈ + 150 to + 250
Sample 5	MESA	10 mM $HClO_4$	≈ +500
Sample 5	-	10 mM $HClO_4$	no minimum found

4.3 Protonation - Deprotonation

The results of the CV and EIS measurements performed to investigate the protonation/deprotonation reaction are presented in this section. All the measurements in 0.1 M NaCl strongly depend on the immersion time of the sample in the electrolyte. More peaks appear and the peaks get higher in CVs when untreated npAu is kept in the electrolyte for a longer time. For npAu modified with MHDA only very small peaks can be seen after 5 h 46′ and the height of the peaks increases strongly with immersion time.

During the measurements for protonation and deprotonation reaction it is tried to establish a constant pH-value. However, a drift in the value measured with the pH-electrode is observed for almost all the measurements. After the measurement, the pH-value is lower than at the beginning. The difference reaches values up to about 0.3. Some part of this drift might be caused by the difference between the pH-value measured in a stirred solution and in an unstirred solution. Without stirring the H^+ and OH^- ions adsorb on the glass electrode of the pH meter. A double layer and a triple layer of ions exists at the solution side of the interface. The ions change the potential of the glass electrode which is measured versus a reference electrode. Stirring disturbs the double and triple layer and therefore changes the result of the pH measurement[49]. After stirring is stopped the layers are built up again. During this time a shift in the measured pH value is observed. Stirring is stopped 5 min before each measurement, but a slight drift in pH is still present. The pH values of the protonation/deprotonation measurement are always given as the value at the beginning of the CV or EIS measurement. There is also a long-term drift in pH of about 2 when the measurement setup is kept for 16 h.

4.3.1 CV Measurement Results

Untreated npAu

CV measurements are performed on untreated npAu (sample 11) in 0.1 M NaCl as a reference to compare the appearing peaks with peaks present in the samples modified with a SAM. Measurements are performed after different times of immersion in the electrolyte and different pH values. Immersion times and pH values at the beginning of the measurements are listed together with the OCP in table 4.5. The OCP increases at the beginning and reaches a stable value at long immersion times. Two CV curves are shown to compare the peaks after only 2 h 33′ in the electrolyte (figure 4.14a) and after 21 h 32′ (figure 4.14b). Clearly more peaks appear at longer immersion times and the height of the peaks increases.

Table 4.5: Immersion time t, pH value and open circuit potential OCP for the CV measurements on untreated npAu (sample 11) in 0.1 M NaCl.

t	pH	OCP / V vs Ag/AgCl
1 h 17′	6.7	+ 0.11
2 h 33′	9.7	+ 0.54
18 h 19′	7.7	+ 0.64
21 h 32′	9.1	+ 0.65
24 h 8′	9.6	+ 0.64

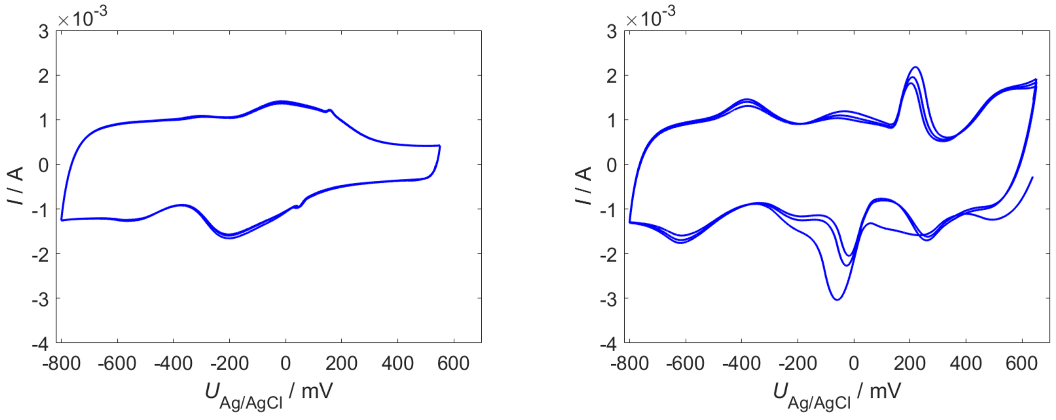

(a) **(b)**

Figure 4.14: CV scans with 5 mV/s on untreated npAu (sample 11) in 0.1 M NaCl: (a) at pH 9.7 after 2 h 33′, (b) at pH 9.1 after 21 h 32′ in solution.

npAu modified with MHDA

Many CV measurements are performed on sample 8 modified with long-chained MHDA after different immersion times and at different pH values. Immersion time, pH and OCP at the beginning of the measurements are listed in table 4.6. Three CV curves are shown in figure 4.15 to demonstrate the influence of immersion time and storage at air for 24 h. At potentials below −200 mV all the curves have an offset towards negative currents which increases at more cathodic potentials. Figure 4.15a shows the CV data recorded after 5 h 46′ at a pH of 9.2. Only a small peak appears at −600 mV during the cathodic scan and no counterpeak can be seen during the anodic scan. Higher peaks appear after 25 h 26′ in 0.1 M NaCl at ph 7.5 in figure 4.15b. Two peaks appear very close to each other between −200 mV and 0 mV in the anodic scan. After 49 h in 0.1 M NaCl, 24 h at air and 3 h 33′ in 0.1 M NaCl at pH 7.1, the peaks still have a very similar shape but are more pronounced.

Table 4.6: Immersion time t, pH value and open circuit potential OCP for the CV measurements on sample 8 modified with MHDA in 0.1 M NaCl.

t	pH	OCP / V vs Ag/AgCl
1 h 15′	5.8	+ 0.14
3 h 39′	9.2	+ 0.10
5 h 46′	9.2	+ 0.10
6 h 26′	8.0	+ 0.14
23 h 57′	7.0	+ 0.16
25 h 26′	7.5	+ 0.17
24 h in electrolyte 24 h at air again immersed in electrolyte		
0 h 37′	5.5	+ 0.17
1 h 40′	5.2	+ 0.16
2 h 39′	6.7	+ 0.20
3 h 33′	7.1	+ 0.23
4 h 43′	8.0	+ 0.23
5 h 43′	8.6	+ 0.25
6 h 23′	9.1	+ 0.21
7 h 3′	9.7	+ 0.18

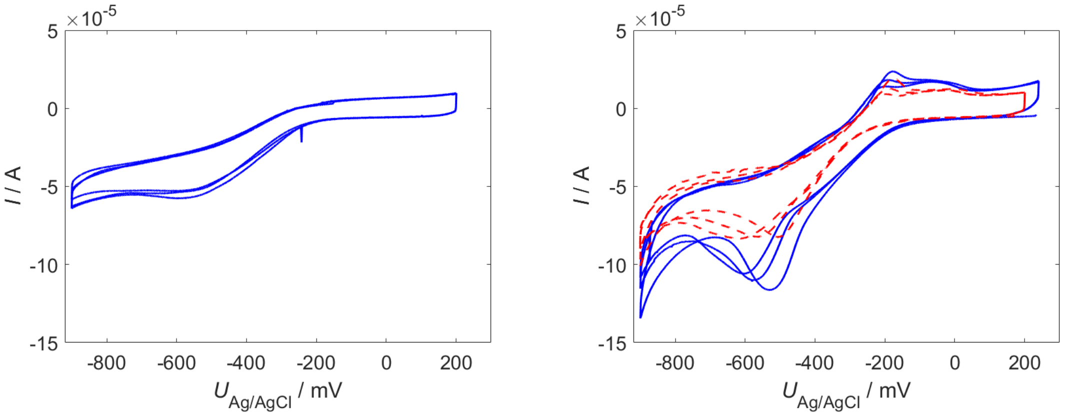

(a) **(b)**

Figure 4.15: CV scans with 5 mV/s on sample 8 modified with MHDA: (a) at pH 9.2 after 5 h 46′ in 0.1 M NaCl (—), (b) at pH 7.5 after 25 h 26′ in 0.1 M NaCl (- - -) and at pH 7.1 after 49 h in 0.1 M NaCl, 24 h at air and 3 h 33′ in 0.1 M NaCl (—).

A series of measurements is performed after 49 h in 0.1 M NaCl, 24 h at air and immersion in 0.1 M NaCl similar to the measurements shown in figure 4.15. The pH decreases in the beginning from 5.5 to 5.2 and is then increased stepwise to 9.7 by adding 10 mM NaOH. Three CV cycles are done in each measurement to ensure stability of the measured effects. The peaks during the negative scan of the 2nd and 3rd cycle for the different pH values are shown in figure 4.16.

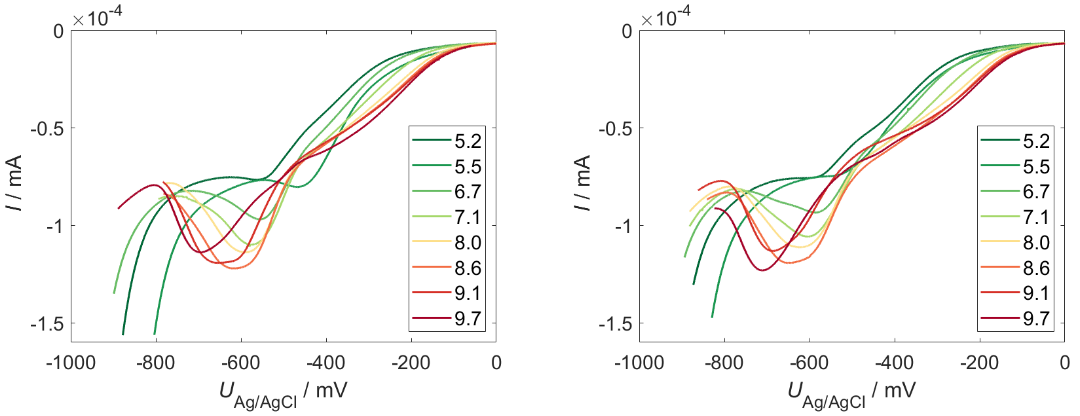

(a) (b)

Figure 4.16: Sample 8 with MHDA at different pH values after 49 h in 0.1 M NaCl, 24 h at air and immersion in 0.1 M NaCl (immersion times and OCP are listed in table 4.6): peak in negative scan direction for CV scans with 5 mV/s: (a) 2nd CV cycle and (b) 3rd cycle.

In all the CV curves the protonation peak in the 2nd cycle (figure 4.16a) is larger than the peak in the 3rd cycle (figure 4.16b) except for the measurement at a pH of 9.72 (see figure 4.17). It can not be explained why the peak at a pH of 9.72 in the 3rd cycle is even higher than the one in the 3rd cycle at a pH of 8.59.

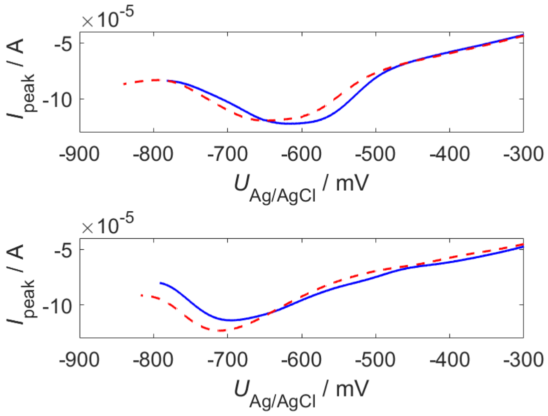

Figure 4.17: Comparison of the protonation peaks of 2nd (—, shown also in figure 4.16a) and 3rd (- - -, 4.16b) CV cycle for a pH of 8.59 (top) and 9.72 (bottom) of the CV data recorded on sample 8 with MHDA in 0.1 M NaCl with a scan rate of 5 mV/s.

npAu modified with MPA

To determine the influence of different chain lengths, similar experiments are performed on sample 15 modified with the short-chained MPA SAM. In table 4.7 the insertion times together with pH and OCP before each CV measurement are listed. The results of some of the CVs are depicted in figure 4.18 to show the evolution of the CV curves over time. The shape and also the OCP change strongly with time and at the end they are very similar to the measurements on untreated npAu.

Table 4.7: Insertion time t, pH value and open circuit potential OCP for the CV measurements on sample 15 modified with a MPA SAM.

t	pH	OCP / V vs Ag/AgCl
1 h 1′	5.7	+ 0.28
1 h 35′	5.2	+ 0.92
2 h 7′	5.3	+ 0.14
3 h 52′	7.6	+ 0.30
5 h 41′	8.9	+ 0.33
7 h 2′	9.6	+ 0.41
24 h 16′	10.3	+ 0.59

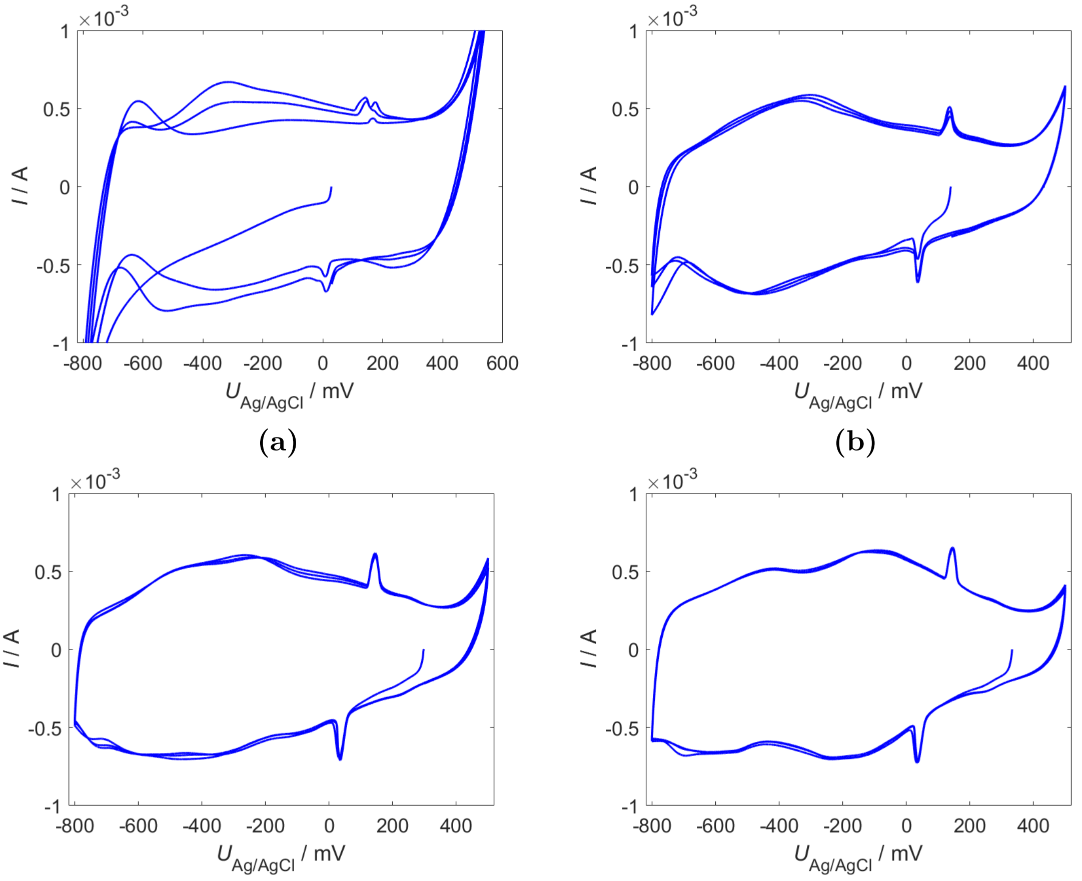

(a) **(b)** **(c)** **(d)**

Figure 4.18: CV scans with 5 mV/s on sample 15 modified with MPA in 0.1 M NaCl: (a) at pH 5.7 after 1 h 1′ in the electrolyte, (b) at pH 5.3 after 2 h 7′, (c) at pH 7.6 after 3 h 52′, (d) at pH 8.9 after 5 h 41′.

4.3.2 EIS Measurement Results

npAu modified with MHDA

EIS measurements are performed on sample 9 modified with a MHDA SAM at different applied potentials and a pH of 9.5 after 80 h in the electrolyte to verify the results of the CV measurements. When changing between two potentials a linear voltage sweep is performed at a very low scan rate of 0.5 mV/s. The linear voltage sweeps are presented in figure 4.19. One peak appears in negative direction at −540 mV and one in positive direction at −60 mV similar to the CV scans shown before with a higher scan rate of 5 mV/s.

The dependence of the effective interfacial capacitance C_{eff} on frequency is shown in figure 4.20a for the different potentials. A plateau can be seen at intermediate frequencies

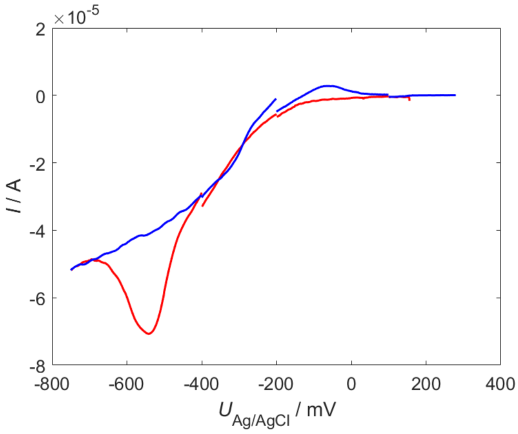

Figure 4.19: npAu with MHDA in 0.1 M NaCl at pH 9.5 after 80 h in solution: Linear voltage sweeps between EIS measurements with a scan rate of 0.5 mV/s in negative (—) and positive direction (—).

and an increase towards lower frequencies for some applied potentials (figure 4.20a). The increase depends on the applied potential but also on the direction of the linear voltage sweep between the measurements. It is strongest at $-400\,\mathrm{mV}$ close to the peak in the cathodic scan in figure 4.19. In figure 4.20b the corresponding Bode phase plots are shown. A decrease in $-\varphi$ can be observed at low frequencies for some potentials which is again strongest at $-400\,\mathrm{mV}$. In both plots in figure 4.20 good capacitive behavior at low frequencies can be seen for applied potentials of $+280\,\mathrm{mV}$ and $+100\,\mathrm{mV}$.

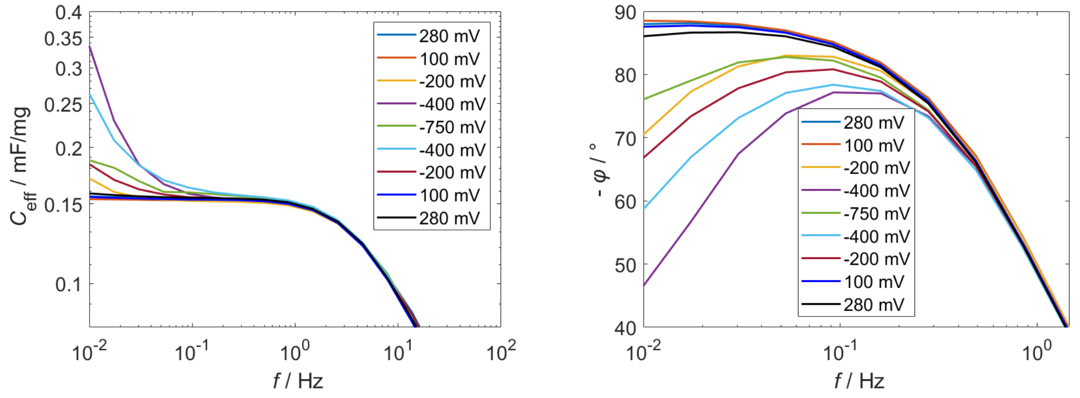

(a) **(b)**

Figure 4.20: (a) Effective interfacial capacitance C_{eff} dependent on frequency f, (b) low frequency part of Bode phase plot for npAu modified with MHDA in 0.1 M NaCl at pH 9.5 after 80 h in solution. The legend indicates the chronological order of the measurements.

The data are fitted with EEC fits in the NOVA software to further investigate charge transfer during the measurements. The Nyquist plot and the EEC of the measurement at $-400\,\mathrm{mV}$ going towards more negative potentials are shown in figures 4.21a and

4.21b. Since the protonation/deprotonation process is formally similar to a Faradaic reaction, a charge transfer resistance R_{CT} is put in parallel with the last capacitance in the EEC fit. In the Nyquist plot the onset of a big semicircle can be seen at low frequencies. In figures 4.22a and 4.22b are the same plots for the first measurement at +280 mV. Only slight bending of the curve can be seen at low frequencies and R_{CT} is two orders of magnitude higher at +280 mV. For both applied potentials the first two capacitors create the high-frequency semicircle and do not contribute to the interfacial capacitance of the sample.

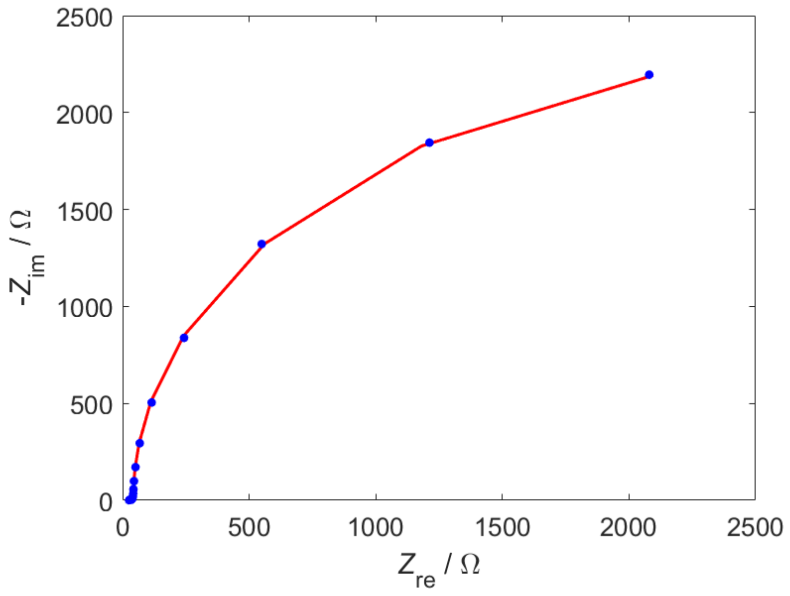

(a)

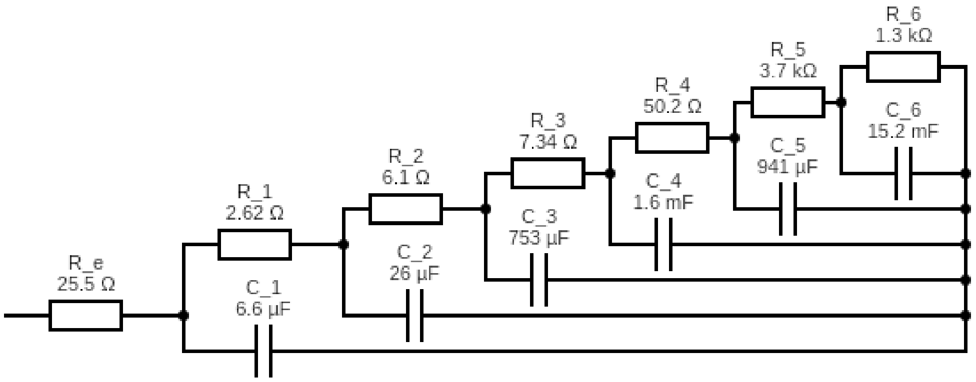

(b)

Figure 4.21: EIS measurement between 100 kHz and 10 mHz at −400 mV going towards more negative potentials on sample 9 with MHDA in 0.1 M NaCl: (a) Nyquist plot of measured EIS data (●) and fit (—), (b) Equivalent electrical circuit according to the theory of de Levie[40] and Keiser[41].

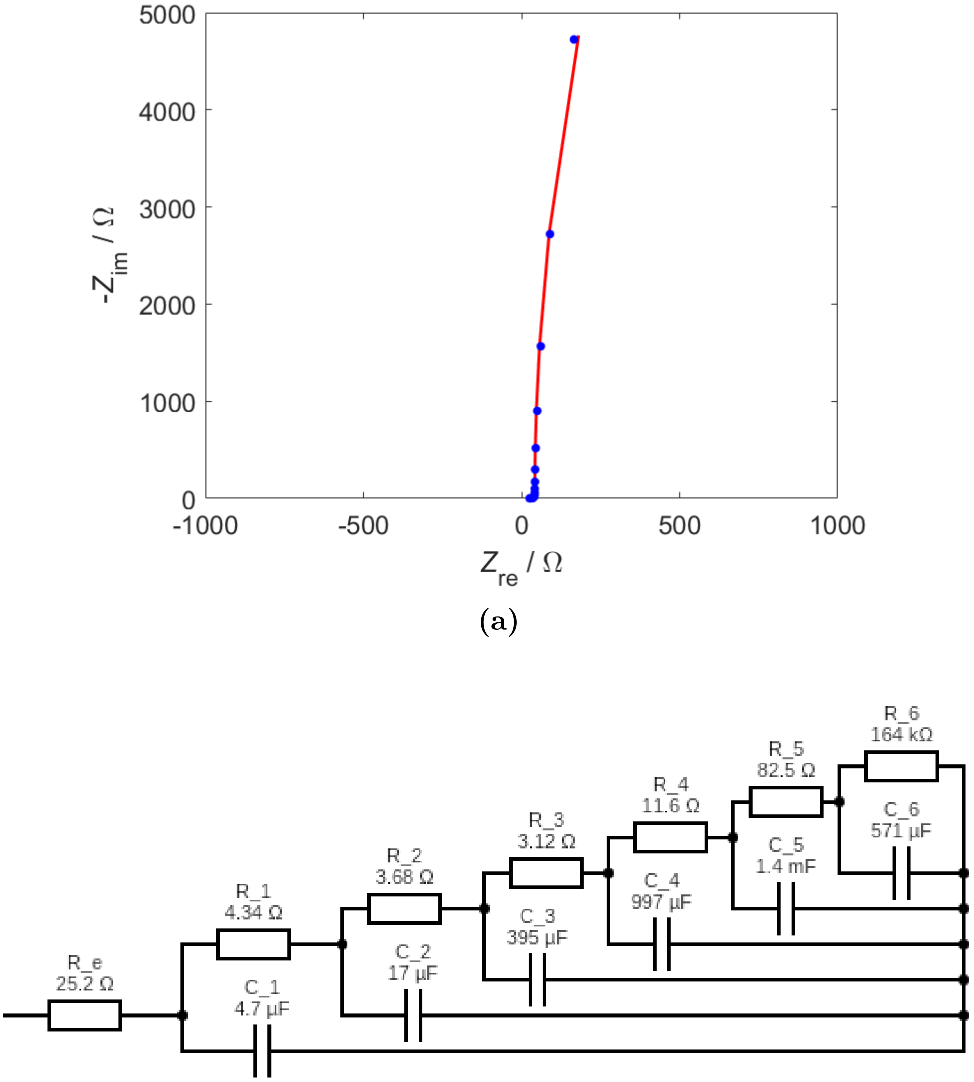

(a)

(b)

Figure 4.22: Same as figure 4.21 measured at +280 mV.

5 Discussion

In this chapter the results are considered in more detail. The underlying processes are discussed and the results compared with literature. First, the differences between the untreated npAu and samples modified with SAMs are discussed by analyzing the EIS spectra in the double layer regime. Then, the PZC measurements are investigated in more detail and problems arising from the structure of npAu are discussed. Finally, the protonation/deprotonation reaction of MHDA and MPA is discussed and the CVs will be compared to CVs of untreated npAu.

5.1 EIS measurements

In this part, the EIS measurements performed in the double layer regime at +150 mV vs Ag/AgCl (presented in section 4.1) are discussed in more detail to qualitatively analyze the influence of the SAMs on the samples.

In the Bode phase plot (figure 4.2), the Bode modulus plot (figure 4.3a), and the plot of Z_{im} versus f (figure 4.3b), all samples qualitatively show curves similar to the curves expected for an electrode in its blocking state in the double layer regime but they deviate from the ideal capacitive behavior in the low-frequency regime. The deviation is strongest for untreated npAu and smallest for the sample modified with the long-chained MHDA. The plot of the derivative of Z_{im} versus f (figure 4.3d) and the Bode phase plot (figure 4.2) are presented again in figures 5.1a and 5.1b, respectively, to discuss the differences of the different samples in more detail. For untreated npAu, the slope of Z_{im} versus f (figure 5.1a) does not converge to a stable value at low frequencies and reaches values more negative than -1. In the Bode phase plot (figure 5.1b), the untreated npAu sample does not increase to 90° at low frequencies. Strong fluctuations can be seen at the lowest frequencies in both plots. These effects probably originate from surface heterogeneities of the nanoporous sample with many different surface states such as terraces, steps and low-coordinate surface atoms which are related to different frequencies. The values for MESA in the Bode phase plot (figure 5.1b) are clearly smaller than for MPA at low frequencies which indicates that the SAM formed by MESA creates a less uniform surface with more heterogeneities even though they have similar lengths. The sample with a long-chained MHDA monolayer has the most homogeneous surface and a phase close to 87° is reached. The creation of a SAM leads to a more uniform and smoother surface especially in the case of MHDA. An additionally reason for deviation from the ideal capacitive behavior for all the samples is the influence of pores of different sizes[50].

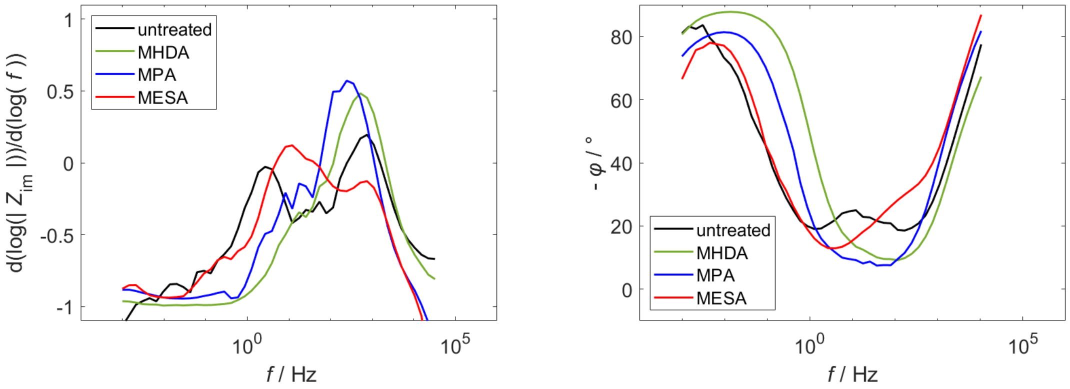

(a) **(b)**

Figure 5.1: EIS data of untreated npAu (—), modified with MHDA (—), MPA (—) or MESA (—) recorded at +150 mV in 10 mM $HClO_4$ between 100 kHz and 1 mHz : (a) Derivative of Z_{im} versus f (taken from figure 4.3d), (b) corrected Bode phase plot (taken from figure 4.3a).

Charge transfer occurs at the lowest measured frequencies for all the samples modified with different SAMs. This can be seen by the decrease in phase in figure 5.1b. It is probably caused by the early onset of hydrogen evolution at the Au surface. For the short-chained MPA and MESA SAMs, ions can pass through the SAM and reach the electrode surface due to the short chain length and due to defects in the monolayer which can be described as pinholes[16]. For the long-chained MHDA, the formation of a defect-free monolayer is expected not allowing any ion transfer through the SAM. This is described in literature for long chained SAMs on flat Au surfaces[16] and on npAu[51]. Boubour et al.[52] have, however, already observed the deviation of $-\varphi$ from 90° at low frequencies for long-chained SAMs in an electrolyte without electrochemical redox couple below a critical potential. When the applied potential is lower than the critical potential, the SAM transforms and defects are induced. Perturbation of the SAM is then possible which causes the deviation from the blocking state. The critical potential for MHDA stated by Boubour et al. is, however, −350 mV which is much more cathodic than the +150 mV applied here during the EIS measurements. Another source of charge transfer might be an incomplete monolayer of MHDA caused by the relatively short immersion time of 26 h in 5 ml of the solution containing 6.2 mM MHDA. According to Patel et al.[51], a blocking layer of a long-chained thiol is already formed after 24 h but the blocking properties still increase slowly over the next 4 days. For a short-chained SAM, completion of the monolayer after 72 h was reported by Hengge et al.[53]. Longer immersion in the SAM solution would probably increase the blocking behavior of the MHDA SAM. For MPA and MESA, longer immersion times would, however, not lead to a blocking layer. Patel et al.[51] could not form a blocking layer with short-chained thiol SAMs on npAu even after 2 weeks of immersion in the SAM solution.

Good agreement is found between the EEC fit (table 4.2) of the EIS data and the effective capacitance C_{eff} in the low frequency regime (see figure 4.4). A clear decrease in interfacial capacitance can be seen when npAu is modified with SAMs. This decrease depends on the chain length because the capacitance of the SAM is in series with the double layer capacitance. A longer chain length d leads to a smaller capacitance according to $C_{\text{SAM}} = \frac{\epsilon\epsilon_0}{d}$. MHDA is the longest molecule used for the SAMs and has the lowest capacitance whereas MPA and MESA have similar lengths and the capacitance is of the same magnitude. The difference in capacitance between the MPA and MESA SAMs might arise from the different polarity of the molecules. The EEC fit also shows the increase in pore resistance with increasing chain length. This is probably caused by the decrease in pore radius.

5.2 Point of Zero Charge

In this part the results of section 4.2 are interpreted in more detail and obstacles arising during the determination of the point of zero charge (PZC) are discussed.

During the EIS measurements to determine the PZC, a small negative DC current was observed on all the samples at potentials more cathodic than +200 mV which increases at more cathodic potentials. It is most likely caused by the early onset of hydrogen evolution at the Au surface as already discussed in section 5.1 for the different samples. The determination of the interfacial capacitance is therefore done in a frequency regime where no influence of charge transfer on interfacial capacitance is assumed. An example of the DC current is shown in figure 5.2 for sample 6 modified with MPA.

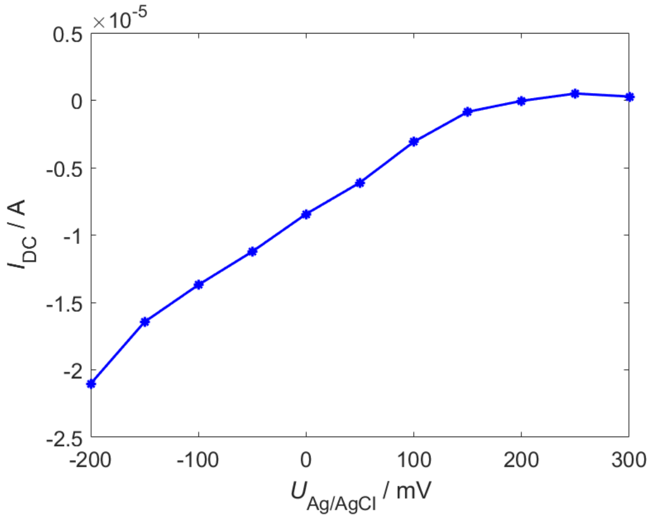

Figure 5.2: DC current during the EIS measurements for the determination of the PZC on sample 6 modified with MPA in 10 mM $HClO_4$. The results of the PZC determination of this measurement are shown in figure 4.11.

5.2.1 Untreated npAu

The results of the EIS measurements performed on npAu show no minimum of C at any potential in 10 mM $HClO_4$ in the double layer regime (figure 4.7). Starting from the higher edge of the investigated potential range, C decreases towards more cathodic potentials until it increases strongly due to the onset of charge transfer. The values in the double layer regime depend on the frequency used to calculate C_{eff} but they also vary with the applied potential. This means that the double layer capacitance is influenced by the diffuse layer capacitance C_{D}. A clearly higher and more constant C is observed in 0.1 M $HClO_4$ (figure 4.8b). This is caused by the higher electrolyte concentration, which decreases the thickness of the diffuse part of the double layer and increases its capacitance C_{D}. Therefore, also C increases and it might be dominated by the Helmholtz capacitance C_{H}, which does not depend much on the potential.

As known from literature[54], the values of the PZC depend strongly on the crystal orientation. This might be the reason, that the PZC of npAu could not be determined. The values of the PZC of different crystal orientations of Au in 10 mM $HClO_4$ are listed in table 5.1. The values were originally given versus SCE and then shifted to Ag/AgCl, taking the potential of Ag/AgCl as -0.04 V versus the SCE electrode. When the desorption of cysteine on similar samples of npAu was observed by Hengge et al.[53], they found that 9.3×10^{-7} mol out of the total 3.5×10^{-6} mol adsorbed Cysteine molecules is adsorbed on the (111) Au plane. This is the surface of fcc Au with the lowest surface energy[55] and seems to make up for only 27% of the npAu surface. Chen-Wiegart et al[56] found that for thermally coarsened npAu 16% of the surface are oriented in the {111}-direction with a 10° angular tolerance. 10% are oriented in the {100}-direction with a 10° angular tolerance. Therefore, large contributions must also originate from other, less stable, surface structures. All these surface sites would create capacitors which are connected in parallel to create the total interfacial capacitance. Even if a minimum of C was found in the measurements, it would not correspond to the PZC but rather to the PZC of the dominant surface orientation. Charge would still accumulate at the other surface sites.

Table 5.1: PZC of Au in 10 mM $HClO_4$ for different crystal orientations[54].

Surface orientation	PZC / V vs Ag/AgCl
Au(111)	+ 0.27
Au(100)	+ 0.12
Au(110)	+ 0.02
Au(210)	- 0.06

The work function (and with it the PZC) of a surface depends strongly on the roughness of the surface which causes the differences in PZC for the different surface orientations. Rough surfaces induce many dangling bonds for atoms close to the surface of the metal which lead to a cathodic PZC[57]. Many low coordinated surface atoms[58] and a lot of steps and surface defects are expected to appear on the surface of npAu. It is therefore hard to compare the results of the PZC measurements of npAu with values of samples with a well defined surface orientation. The low coordinate surface atoms and defects probably create an even rougher surface than the (210) and cause an even more cathodic PZC. Similar considerations were done by Doneaux et al.[54] regarding the surface of polycrystalline gold. They analyzed the desorption of different SAMs from a polycrystalline gold surface and compared them to peaks appearing in the desorption of well defined surfaces with only one orientation. The biggest desorption peak was very close to the desorption peak of the (210) Au surface which is the crystallographic orientation with the roughest surface structure they investigated. They concluded that the similarity of the desorption peaks is not caused by the actual presence of (210) domains but rather to the similarities of the (210) surface to the microscopic environment of the polycrystalline sample, which has a lot of kinks and steps.

5.2.2 npAu modified with SAMs

Adding a layer of organic molecules leads to a more even surface. In the case of the long MHDA molecule the influence of different surface structures of the npAu can no longer be seen after the creation of the SAM. The measurements on the samples with MPA and MESA still show some influence of the heterogeneous underlying structure which complicates the determination of the PZC.

For sample 3 modified with MHDA, a minimum in interfacial capacitance is observed at about +100 mV (figure 4.10a). This is close to the PZC at $0.12 \pm 0.01\,\mathrm{V}$ for 11-mercaptoundecanoic acid on Au(111) in 0.1 M $HClO_4$ determined by Ramirez et al[33]. The determination of the PZC is done at 133 mHz where perturbation does not influence C_{eff}, as shown in figure 4.6b.

The measurements on sample 6 modified with a MPA SAM (figure 4.11) do not result in a clear minimum of C. Some influence of the npAu surface is still present in the measurements due to pinholes in the monolayer[16] as already described above, which makes the determination of the PZC much more difficult. The measured values are, however, clearly lower around +100 mV to +300 mV rather than at negative potentials (figure 4.11). Therefore, it can be assumed that the PZC is equal or more anodic than +100 mV.

During the EIS measurements on sample 5 modified with MESA, some part of the SAM might desorb from the sample when the potential is shifted from +250 mV to −200 mV. The CV curve of a fresh MESA SAM (— in figure 5.3b) differs strongly from the CV recorded on sample 5 modified with MESA after the EIS measurements (- - -). Desorption leads to an increase in C because the interfacial capacitance of npAu without a SAM is much higher. Since the values measured before at more cathodic potentials are bigger than the ones measured afterwards at more anodic potentials, the PZC seems to be at more anodic potentials (figure 4.12). The difference in interfacial capacitance could be even bigger if the potentials were changed in a different order. Additionally, there is still a negative DC current (figure 5.3a) during the measurements at +250 mV, +300 mV and +350 mV. The system was not in its equilibrium state during these measurements which explains the large difference between the two capacitance values measured at +250 mV and the large capacitance at +300 mV (figure 4.12). Equilibrium is reached during the measurement at +400 mV, 6 h after the potential switch from −200 mV to +250 mV. A small minimum of C can be seen in figure 4.12 at +500 mV and it can be assumed that the PZC is approximately at this potential.

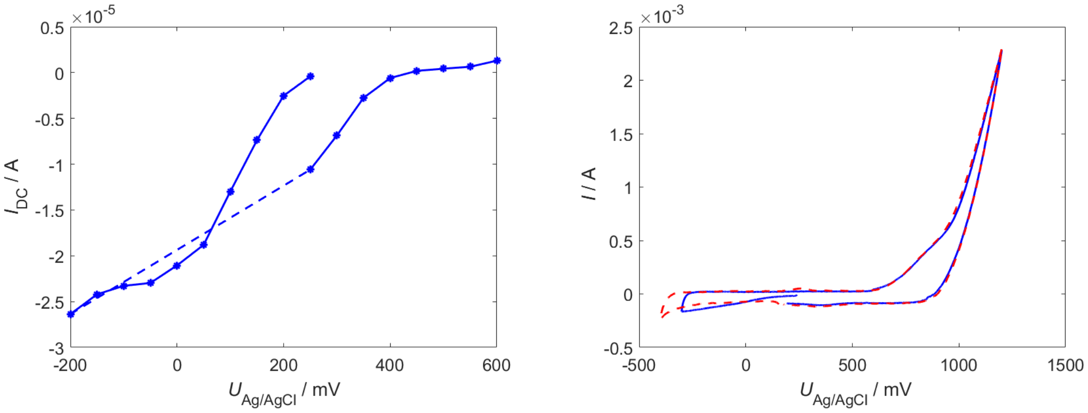

(a) **(b)**

Figure 5.3: (a) DC current I_{DC} during the EIS measurements for PZC determination of sample 5 modified with MESA in 10 mM $\mathrm{HClO_4}$ dependent on potential $U_{\mathrm{Ag/AgCl}}$. (b) CV recorded after the measurements shown in (a) (- - -) compared to the first CV cycle of a fresh MESA SAM (—). Scan rate: 1 mV/s.

The difference in the PZC for the different SAMs is caused by differences in dipole moment perpendicular to the electrode surface[33]. MESA has the highest polarity of the three used molecules due to dissociation of a H^+ ion from the sulfonic acid group even at very low pH values and therefore has the most anodic PZC.

5.3 Protonation - Deprotonation

In the following part further interpretation of the results of section 4.3 is done. The CVs to investigate the protonation/deprotonation reaction on samples modified with MHDA and MPA are analysed and compared to the CVs on untreated npAu. The EIS measurements on a sample modified with MHDA are then used to analyze the reaction in more detail. Long immersion times are needed for samples modified with MHDA before the protonation/deprotonation reaction can be observed. This is probably caused by long diffusion times of the electrolyte into the porous sample, since the pore size is about 10 nm to 20 nm[25] and the length of MHDA 2 nm[59].

Untreated npAu

The CV curves of untreated npAu in 0.1 M NaCl change strongly with the immersion time of the sample in the electrolyte. More peaks appear in the spectrum recorded after 21 h 32′ and some are much bigger than the ones present in the CV curve measured after 2 h 33′ (figure 4.14). It is very likely that the adsorption of Cl^- ions is responsible for these changes. Lipkowski et al.[60] show that adsorption of Cl^- ions already takes place at potentials more cathodic than the PZC on an Au(111) surface. The adsorption then strongly increases at more anodic potentials. Adsorption of anions causes pseudocapacitive behavior in the double layer regime of the interface which strongly changes CV results even at very low Cl^- concentrations of 10^{-6} M or 10^{-3} M[61]. Increasing concentration changes the CV again very strongly[62]. All these measurements were performed on Au samples with defined surface orientations. They show strong dependence on the concentration of Cl^- and several peaks arise from adsorption[61]. Even more features appear in the CV curves (figure 4.14) of npAu probably due to its rough surface structure. No attempt is made to interpret the appearing peaks in the present work. The spectra are only used for comparison with the CVs on npAu modified with SAMs.

npAu modified with MHDA

The CV curves on npAu modified with a MHDA SAM (figure 4.15) have a very different shape than the CVs recorded on untreated npAu (figure 4.14). A small peak in the negative scan direction is visible after 5 h 46′ in the electrolyte. This peak increases strongly when the sample is left in the NaCl-solution for 25 h 26′ and a counterpeak appears in the positive scan direction. Since the peak height increases but the peak potential does not change strongly, it can be assumed that diffusion of the electrolyte into the pores was not completed after 5 h 46′ and the system was not in equilibrium. After leaving the sample in the electrolyte for 49 h, at air for 24 h and putting it back into the electrolyte for 3 h 33′, the peaks are even more prominent but still have a similar shape as after 25 h 26′ in the electrolyte. It is concluded that the SAM is stable and does not desorb during the measurements or during storage within the electrolyte or at air for 24 h. Similar stability has been reported in literature[6] [8].

There is one peak in the spectrum of the untreated npAu at about -0.6 V (figure 4.14) close to the peak of the sample with a MHDA SAM (figure 4.15). The shape is, however, very different and also the counterpeak does not appear at the same potential. It is therefore assumed that these two peaks are not caused by the same effect. All other peaks present in the CVs of untreated npAu do not appear in any of the CVs performed on npAu modified with MHDA. An almost completely blocking monolayer of MHDA can therefore be assumed which is in good agreement with literature for long-chained thiols on npAu[51], as already discussed in section 5.1. An exception is again the small negative DC current measured at cathodic potentials probably caused by the early onset of hydrogen evolution on the Au surface (similar to figure 5.2 for MPA). It causes the negative shift of the CV visible especially below -100 mV in figure 4.15 and probably also obscures the anodic deprotonation peak.

The peaks of sample 8 modified with MHDA clearly show a dependence on pH (see figure 4.16). The peak heights dependent on pH are compared in figure 5.4, where the heights taken from the 2nd and 3rd CV cycle are shown together with their average. The peak heights in the second CV cycle have a clear minimum at a pH of about 8.6. In the third cycle the peak at a pH of 9.7 is most pronounced. The average still shows a minimum at 8.6. It can be assumed that the pK_a of MHDA on npAu is around 8.6, which is in very good agreement with literature where Smiljanic et al.[48] report the highest peak in the CVs at a pH of 8.8.

The average peak potential dependent on pH can be seen in figure 5.5. Also a linear fit is done which does not include the second measurement at pH 5.21 since it is the only point deviating strongly from the linear fit. The slope of the fit is -45 ± 4 mV/decade, which is a bit lower than the $-59\,\frac{\mathrm{mV}}{\mathrm{decade}}$ expected according to equation 2.24. The

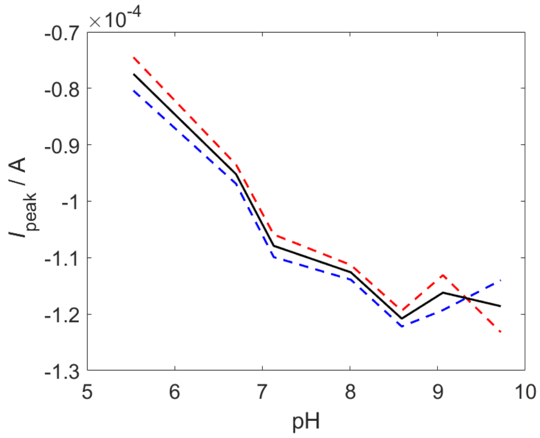

Figure 5.4: Peak current I_{peak} versus pH of the CV data recorded on sample 8 with MHDA in 0.1 M NaCl with a scan rate of 5 mV/s: Peak heights in 2nd (- - -) and 3rd (- - -) CV cycle and average (—).

calibration of the pH-electrode gave only -52 mV/decade which accounts for part of the difference. Additionally, the potential used for the slope of the linear fit is the potential difference between the electrode and the bulk solution and not ΔV_S. This might also cause some discrepancy between the values[18].

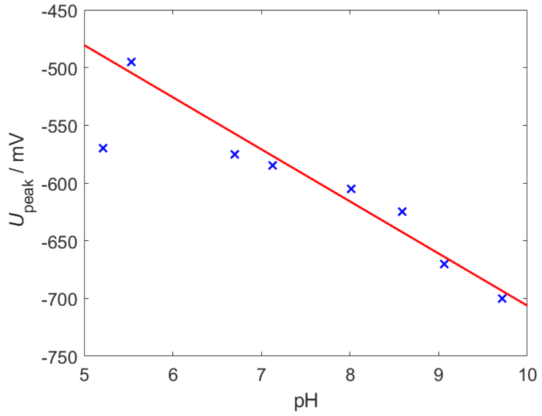

Figure 5.5: npAu with MHDA in 0.1 M NaCl at different pH values: Potential at the peak position U_{peak} versus pH value, measurement potentials (×) and linear fit (—).

npAu modified with MPA

The CV curves of sample 15 modified with a MPA SAM show peaks already after 1 hour in the electrolyte at a pH of 5.7 (figure 4.18). In figure 5.6 the peaks of MPA (—) are larger and the separation between the peaks is smaller than for MHDA (—), but the location of the average of the peaks is similar to the measurements with MHDA.

This is in agreement with the results of Smiljanic et al.[48] which show that the peak height of protonation and deprotonation decreases and the peak separation increases with increasing chain length. For the first two measurements in figure 4.18 the peaks appear at potentials where there are no peaks for untreated npAu. It is therefore assumed that these peaks correspond to the protonation/deprotonation reaction.

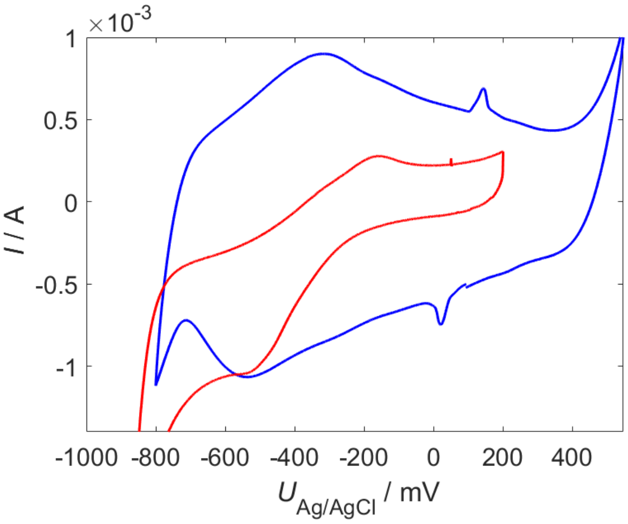

Figure 5.6: Comparison of CV measurements on npAu modified with MPA and MHDA with a scan rate of 5 mV/s: MPA at pH 5.2 (—) after 1 h 35′ in the electrolyte, MHDA at pH 5.5 after 49 h in 0.1 M NaCl, 24 h at air and 0 h 37′ in the electrolyte multiplied by 14 (—).

However, the measurement in figure 4.18a after 1 hour in the electrolyte has peaks at 0 V and +0.15 V very similar to those found in the CV of untreated npAu (compare figure 4.14a). As discussed in the previous sections, this is caused by the short chain length of MPA which leads to the formation of pinholes in the SAM[16]. After longer immersion time of the sample in the electrolyte, the shape of the curves changes very strongly (see figure 4.18) and takes the shape of the CVs of untreated npAu. After 3 h 52′ at pH 7.6 there are features from both the MPA SAM and the untreated surface overlapping; after 5 h 41′ at pH 8.9 no more peaks originating from protonation/deprotonation reactions of MPA are visible. Also the OCP increases with time and reaches a value comparable to the untreated npAu. Figure 5.7 shows the 3rd CV cycles of a sample which was originally covered with a MPA SAM after 7 h 2′ in the electrolyte (—) in comparison to an untreated npAu sample after 2 h 33′ in the electrolyte (—). The OCPs are +0.41 V and +0.54 V, respectively. The two curves look very similar and it is concluded that most of the MPA has desorbed. However, no desorption peak can be seen in the CV curves and it could not be determined at which step in the measurement the SAM desorbed.

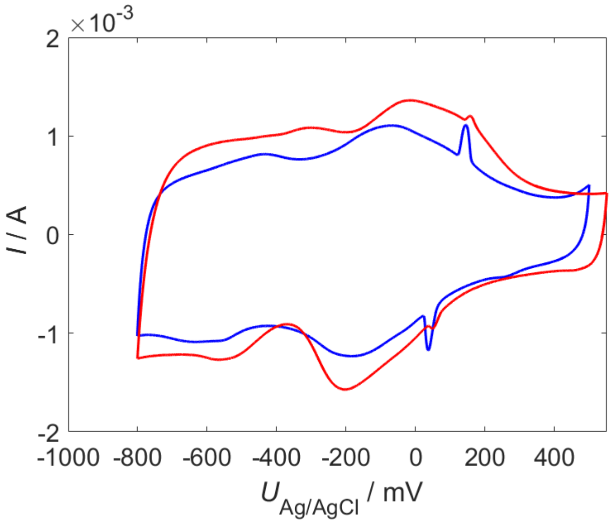

Figure 5.7: Comparison of CV measurements of npAu modified with MPA and untreated npAu: npAu modified with MPA at pH 9.6 with a scan rate of 3 mV/s after 7 h 2′ in the electrolyte (—, multiplied by 5/3 to account for the different scan rates), untreated npAu at pH 9.7 with a scan rate of 5 mV/s after 2 h 33′ in the electrolyte (—).

EIS measurements

The protonation and deprotonation peaks can also be seen in the linear sweeps between the potential points chosen for the EIS measurements (figure 4.19). In the EIS measurements, the Bode phase plots show a decrease of $-\varphi$ at low frequencies for applied potentials around the protonation peak (figure 4.20b). This is a deviation from the purely capacitive behavior and is an indication for a reaction. At potentials more positive than the deprotonation peak the phase stays close to 90° even at low frequencies indicating almost perfect capacitive behavior. The phase dip is shown again in figure 5.8a for the measurements on sample 9 with MHDA and in 5.8b for sample 10 with MHDA for a larger variety of applied potentials and after a shorter immersion time of 8 h in the electrolyte. A minimum can clearly be seen in both plots at about -400 mV to -450 mV. The protonation/deprotonation reaction can be seen in EIS measurements after 8 h in the electrolyte (figure 5.8b), whereas longer times are necessary to observe clear peaks in CV measurements (figure 4.15). In figure 5.8, the phase dip between -400 mV to -600 mV is bigger when the sweep direction is going towards more cathodic potentials (—), whereas it is bigger at -300 mV to -200 mV when going towards more anodic potentials (—). A larger phase dip is measured in the direction in which the peak appears in the linear voltage sweeps.

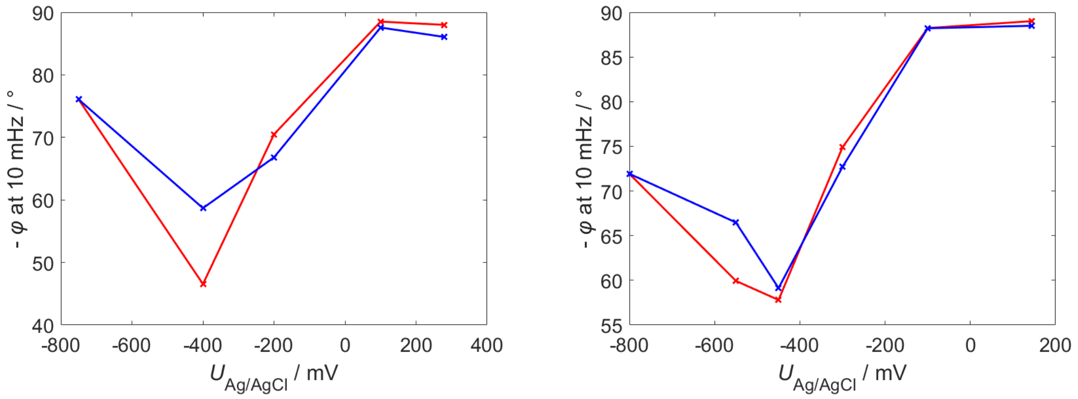

(a) **(b)**

Figure 5.8: Phase dip at 10 mHz during cathodic (—) and anodic scan (—): (a) sample 9 modified with MHDA in 0.1 M NaCl at pH 9.5 after 80 h in solution, (b) sample 10 modified with MHDA at pH 9.0 after 8 h in solution.

The same effect can be seen in the charge transfer resistance R_{CT} of the EEC fits in figure 5.9a. At $-200\,\mathrm{mV}$ R_{CT} is clearly higher during the cathodic scan (—). At $-400\,\mathrm{mV}$ it is higher in the anodic scan (—). At potentials more positive than $-200\,\mathrm{mV}$, R_{CT} is much higher indicating very little charge transfer.

The total interfacial capacitance C taken from the EEC fits in figure 5.9b stays small down to $-200\,\mathrm{mV}$, then increases strongly at $-400\,\mathrm{mV}$, and decreases again at $-750\,\mathrm{mV}$. In the anodic scan (—) C is smaller than in the cathodic scan (—) at $-400\,\mathrm{mV}$ and bigger at $-200\,\mathrm{mV}$. At more anodic potentials C reaches the exact same value as in the previous measurements which indicates reversibility of the reaction.

These observations of the phase dip (figure 5.8), R_{CT} (figure 5.9a), and C (figure 5.9b) all show that the protonation reaction is much stronger around $-400\,\mathrm{mV}$ than at $-200\,\mathrm{mV}$ during the cathodic scan. At $-750\,\mathrm{mV}$ the SAM is in its protonated state. The charge transfer is then probably due to the hydrogen evolution. At $-400\,\mathrm{mV}$ all effects are larger in the cathodic scan than in the anodic scan. At $-200\,\mathrm{mV}$ the effects are smaller during the cathodic scan. The reason for that might be the long time constants related to the protonation/deprotonation and the difference between protonation and deprotonation potential, which is clearly visible even in the very slow potential scan with 0.1 mV/s and several stops for EIS measurements in figure 4.19. At more anodic potentials the values before and after the scan are very close to each other. The reaction is reversible and the measurements do not seem to influence the system.

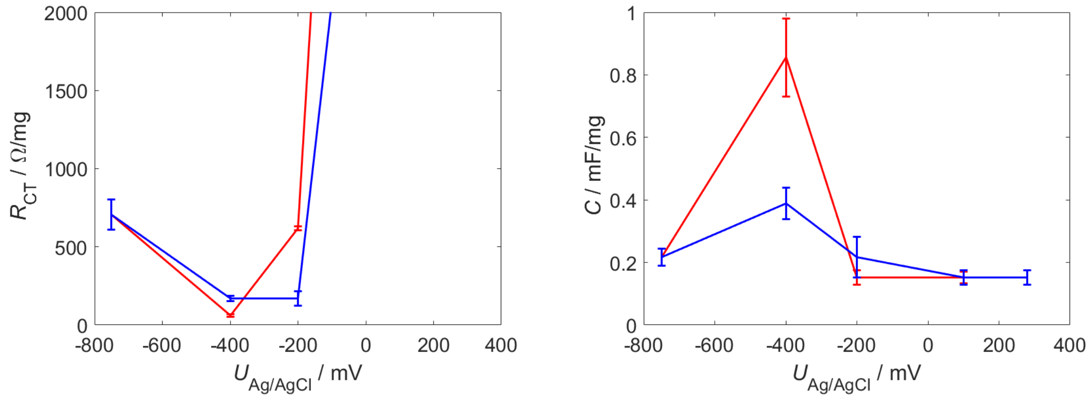

(a) **(b)**

Figure 5.9: EIS measurements on sample 9 modified with MHDA in 0.1 M NaCl at pH 9.5 after 80 h in solution: (a) Charge transfer resistance R_{CT} from EEC fit versus potential $U_{\mathrm{Ag/AgCl}}$ and (b) interfacial capacitance C from EEC fit versus potential $U_{\mathrm{Ag/AgCl}}$ during cathodic (🟥) and anodic scan (🟦).

With the EIS data it is also possible to gain information about the capacitance at higher frequencies where no chemical reactions can take place and C is dominated by the double layer capacitance. The Bode modulus plot with linear fit and frequency constant at the intersection is shown in figure 5.10a. The frequency at the intersection is 1.23 Hz. C taken as C_{eff} at 853 mHz shown in figure 5.10b is lower during the cathodic scan (🟥) than during the anodic scan (🟦) at potentials of −200 mV and −400 mV. At 100 mV and 280 mV C reaches its initial value after protonation and deprotonation. C seems to be higher in the protonated state which is contradictory to results in literature on flat electrodes[63]. Charging the interface by deprotonation of the carboxyl groups should increase the potential drop across the double layer and therefore lead to a higher double layer capacitance[63]. This discrepancy might be caused by non-equilibrium conditions during the measurement. Non-equilibrium is indicated by a changing DC current. Figure 5.11 shows the DC current during the EIS measurement and the time of the measurement used for the C_{eff}-calculations at 853 mHz is indicated by a vertical red line. At this time the DC current deviates from the almost constant current after longer times. A longer wait time at the constant potential might therefore be needed before starting the EIS measurement. All other results of the EIS measurements to investigate the protonation/deprotonation reaction discussed before were either taken at lower frequencies were the system seems to be in equilibrium or taken from the EEC fits which include all frequencies. Another possible explanation is that the onset of charge transfer can already be observed at higher frequencies during the anodic scan. It could influence C_{eff} already at frequencies in the plateau regime of figure 4.20a which are assumed to be dominated by the double layer capacitance. The origin of this shift in frequencies can, however, not be explained.

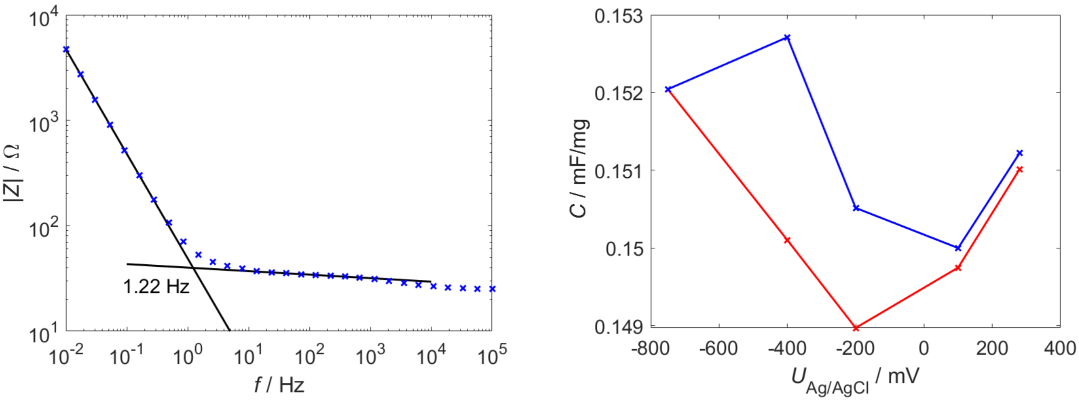

(a) **(b)**

Figure 5.10: EIS measurements on sample 9 modified with MHDA in 0.1 M NaCl at pH 9.5 after 80 h in solution: (a) Bode modulus plot of the EIS data in the frequency range between 100 kHz and 10 mHz at OCP = +280 mV (×) and fits in linear regimes (—), (b) Interfacial capacitance C taken from C_{eff} at 853 mHz during cathodic scan (—) and anodic scan (—).

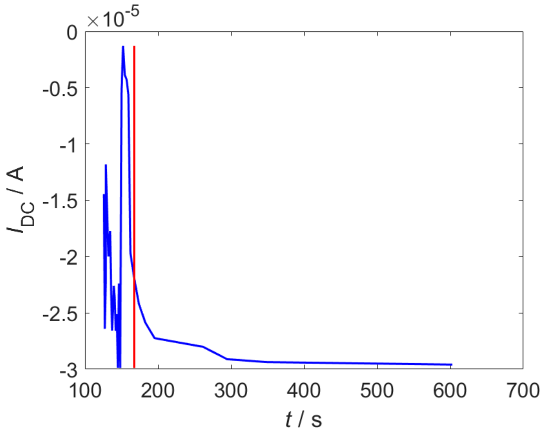

Figure 5.11: EIS measurements on sample 9 modified with MHDA in 0.1 M NaCl at pH 9.5 after 80 h in solution: DC current I_{DC} versus time t of the EIS measurement at −400 mV during the anodic scan (—). The red line (—) indicates the frequency at which the C_{eff}-values are taken for the plot in figure 5.10b.

6 Conclusion and Outlook

In this thesis, the behavior of self-assembled monolayers (SAMs) on nanoporous gold was investigated with a focus on further application in enzyme immobilization. To investigate the differences arising from different chain lengths and functionalized groups, the long-chained 16-mercaptohexadecanoic acid (MHDA) and the short chained 3-mercaptopropionic acid (MPA), both functionalized with a carboxyl group, and sodium 2-mercaptoethanesulfonate (MESA), functionalized with a sulfonic acid group, were used to create the SAMs.

EIS measurements were performed in 10 mM $HClO_4$ between 100 kHz and 1 mHz on the different samples in the double layer regime at +150 mV vs Ag/AgCl. Strong fluctuations in the data were observed at low frequencies on nanopourous gold without a SAM caused by the highly irregular surface with many different surface sites such as terraces, steps, and low-coordinate surface atoms. Modification of the sample with a SAM lead to a more homogeneous surface structure, especially in the case of the long-chained MHDA. For the shorter MPA and MESA the influence of the underlying structure was still visible.

To gain knowledge about the charge at the interface between the sample and the electrolyte, the point of zero charge (PZC) was determined for the different samples by finding a minimum in double layer capacitance. EIS measurements were performed at different applied potentials. Values of the double layer capacitance were then obtained via equivalent electrical circuit fit according to the theory of de Levie [40] and Keiser [41] and via the calculation of the effective capacitance at frequencies where it is dominated by the double layer capacitance. The PZC could not be determined on a nanoporous gold sample without SAM due to the different surface states which have different points of zero charge. For MHDA the PZC was found at +100 mV versus Ag/AgCl. For MPA a potential regime with lower double layer capacitance was determined but no clear minimum was found. The PZC of MPA was assumed to be at about +150 mV to +250 mV. During the measurements on the sample modified with MESA, a part of the SAM might have desorbed at cathodic potentials and the system was not in equilibrium during some of the measurements. However, a minimum could still be assumed around +500 mV versus Ag/AgCl.

To control the degree of dissociation of the carboxyl groups on MHDA and MPA, CV measurements were performed in 0.1 M NaCl with an initial pH of about 5.5 which was then adjusted by adding 0.1 M or 10 mM NaOH or HCl. During the CVs performed on a sample modified with MHDA the current arising from the protonation of the SAMs could be seen. The peak shifted towards more cathodic potentials with increasing pH and was highest around a pH of 8.6. This is in good agreement with results reported in literature. Much higher peaks and less separation between protonation and deprotonation peaks were observed on the sample modified with MPA which is again in agreement with literature. MPA was, however, not stable during the measurements and after several measurements the MPA had desorbed from the sample. EIS measurements were performed on samples modified with MHDA at a pH of 9 to confirm the CV measurements. The biggest dip in the Bode phase plot at 10 mHz was observed at potentials of about −400 mV to −450 mV versus Ag/AgCl. The dip corresponds to charge transfer and the potentials are close to the peak potential of the CVs.

In conclusion, the modification of nanoporous gold with SAMs leads to a more uniform surface. This is important for controlling the surface charge with an externally applied potential. Additionally, the surface charge can be adjusted by controlling the degree of acid dissociation with potential and pH which can be used for immobilization of enzymes.

Continuing this work, several measurements could be done to improve the results. The measurements to determine the PZC on a sample modified with MESA could be repeated only at potentials more anodic than +250 mV to avoid desorption and ensure equilibrium during the measurements. Measurements could be performed to investigate the desorption process of MPA in $HClO_4$ and NaCl. To further investigate the protonation/deprotonation reaction, measurements could be performed on coarsened npAu modified with MHDA for faster diffusion of the electrolyte into the pores. Additionally, a different electrolyte without Cl^--ions could be used to avoid the influence of the complicated behavior of Cl^--ions on npAu.

Bibliography

[1] M. Hakamada, M. Takahashi and M. Mabuchi. Enzyme electrodes stabilized by monolayer-modified nanoporous au for biofuel cells. *Gold Bulletin*, **45** (2011) 9.
DOI: 10.1007/s13404-011-0038-1.

[2] X. Xiao, J. Ulstrup, H. Li, M. Wang, J. Zhang and P. Si. Nanoporous gold assembly of glucose oxidase for electrochemical biosensing. *Electrochimica Acta*, **130** (2014) 559.
DOI: 10.1016/j.electacta.2014.02.146.

[3] K. J. Stine. Enzyme immobilization on nanoporous gold: A review. *Biochemistry Insights*, **10** (2017) 117862641774860.
DOI: 10.1177/1178626417748607.

[4] A. Ulman. Formation and structure of self-assembled monolayers. *Chemical Reviews*, **96** (1996) 1533.
DOI: 10.1021/cr9502357.

[5] S. Dong and J. Li. Self-assembled monolayers of thiols on gold electrodes for bioelectrochemistry and biosensors. *Bioelectrochemistry and Bioenergetics*, **42** (1997) 7.
DOI: 10.1016/s0302-4598(96)05172-0.

[6] E. Cortes, A. A. Rubert, G. Benitez, P. Carro, M. E. Vela and R. C. Salvarezza. Enhanced stability of thiolate self-assembled monolayers (SAMs) on nanostructured gold substrates. *Langmuir*, **25** (2009) 5661.
DOI: 10.1021/la804251a.

[7] I. McCue, E. Benn, B. Gaskey and J. Erlebacher. Dealloying and dealloyed materials. *Annual Review of Materials Research*, **46** (2016) 263.
DOI: 10.1146/annurev-matsci-070115-031739.

[8] C. Vericat, M. E. Vela, G. Benitez, P. Carro and R. C. Salvarezza. Self-assembled monolayers of thiols and dithiols on gold: new challenges for a well-known system. *Chemical Society Reviews*, **39** (2010) 1805.
DOI: 10.1039/b907301a.

[9] F. Malem and D. Mandler. Self-assembled monolayers in electroanalytical chemistry: application of .omega.-mercapto carboxylic acid monolayers for the electrochemical detection of dopamine in the presence of a high concentration of ascorbic acid. *Analytical Chemistry*, **65** (1993) 37.
DOI: 10.1021/ac00049a009.

[10] S. D. Evans and A. Ulman. Surface potential studies of alkyl-thiol monolayers adsorbed on gold. *Chemical Physics Letters*, **170** (1990) 462.
DOI: 10.1016/s0009-2614(90)87085-6.

[11] R. W. Zehner, B. F. Parsons, R. P. Hsung and L. R. Sita. Tuning the work function of gold with self-assembled monolayers derived from $X-[C_6H_4-C\equiv C-]_nC_6H_4-SH$ (n= 0, 1, 2; X = H, F, CH_3, CF_3, and OCH_3). *Langmuir*, **15** (1999) 1121.
DOI: 10.1021/la981114f.

[12] I. Martinović, G. Zlatić, Z. Pilić, L. Šušić, O. Kowalska, D. Petrović, F. Falak and J. Mišković. Self-assembled monolayers of alkanethiol as inhibitors against copper corrosion in synthetic acid rain. *International Journal of Electrochemical Science*, (2019) 4206.
DOI: 10.20964/2019.05.28.

[13] J. C. Love, L. A. Estroff, J. K. Kriebel, R. G. Nuzzo and G. M. Whitesides. Self-assembled monolayers of thiolates on metals as a form of nanotechnology. *Chemical Reviews*, **105** (2005) 1103.
DOI: 10.1021/cr0300789.

[14] C. Vericat, M. E. Vela, G. Corthey, E. Pensa, E. Cortés, M. H. Fonticelli, F. Ibañez, G. E. Benitez, P. Carro and R. C. Salvarezza. Self-assembled monolayers of thiolates on metals: a review article on sulfur-metal chemistry and surface structures. *RSC Adv.*, **4** (2014) 27730.
DOI: 10.1039/c4ra04659e.

[15] Y. Chu, B.-R. Seo and J.-W. Kim. Electrochemical properties of alkanethiol monolayers adsorbed on nanoporous au surfaces. *Bulletin of the Korean Chemical*

Society, **31** (2010) 3407.
DOI: 10.5012/bkcs.2010.31.11.3407.

[16] S. Campuzano, M. Pedrero, C. Montemayor, E. Fatás and J. M. Pingarrón. Characterization of alkanethiol-self-assembled monolayers-modified gold electrodes by electrochemical impedance spectroscopy. *Journal of Electroanalytical Chemistry*, **586** (2006) 112.
DOI: 10.1016/j.jelechem.2005.09.007.

[17] M. Collinson, E. F. Bowden and M. J. Tarlov. Voltammetry of covalently immobilized cytochrome c on self-assembled monolayer electrodes. *Langmuir*, **8** (1992) 1247.
DOI: 10.1021/la00041a004.

[18] I. Burgess, B. Seivewright and R. B. Lennox. Electric field driven protonation/deprotonation of self-assembled monolayers of acid-terminated thiols. *Langmuir*, **22** (2006) 4420.
DOI: 10.1021/la052767g.

[19] V. Zielasek, B. Jürgens, C. Schulz, J. Biener, M. M. Biener, A. V. Hamza and M. Bäumer. Gold catalysts: Nanoporous gold foams. *Angewandte Chemie International Edition*, **45** (2006) 8241.
DOI: 10.1002/anie.200602484.

[20] A. Wittstock, J. Biener and M. Bäumer. Nanoporous gold: a new material for catalytic and sensor applications. *Physical Chemistry Chemical Physics*, **12** (2010) 12919.
DOI: 10.1039/c0cp00757a.

[21] H.-J. Jin and J. Weissmüller. Bulk nanoporous metal for actuation. *Advanced Engineering Materials*, **12** (2010) 714.
DOI: 10.1002/adem.200900329.

[22] N. V. Lavrik, C. A. Tipple, M. J. Sepaniak and P. G. Datskos. Enhanced chemi-mechanical transduction at nanostructured interfaces. *Chemical Physics Letters*, **336** (2001) 371.
DOI: 10.1016/s0009-2614(01)00155-5.

[23] H. Qiu, L. Xue, G. Ji, G. Zhou, X. Huang, Y. Qu and P. Gao. Enzyme-modified nanoporous gold-based electrochemical biosensors. *Biosensors and Bioelectronics*, **24** (2009) 3014.
DOI: 10.1016/j.bios.2009.03.011.

[24] X. Xiao, P. Si and E. Magner. An overview of dealloyed nanoporous gold in bioelectrochemistry. *Bioelectrochemistry*, **109** (2016) 117.
DOI: 10.1016/j.bioelechem.2015.12.008.

[25] J. Biener, A. Wittstock, L. A. Zepeda-Ruiz, M. M. Biener, V. Zielasek, D. Kramer, R. N. Viswanath, J. Weissmüller, M. Bäumer and A. V. Hamza. Surface-chemistry-driven actuation in nanoporous gold. *Nature Materials*, **8** (2008) 47.
DOI: 10.1038/nmat2335.

[26] W. Hamann, Carl H. / Vielstich. *Elektrochemie*. Wiley-VCH, Weinheim (4. Auflage September 2005).

[27] M. E. Orazem and B. Tribollet. *Electrochemical impedance spectroscopy*. John Wiley & Sons (2017).

[28] A. J. Bard and L. R. Faulkner. *Electrochemical Methods: Fundamentals and Applications*. John Wiley & Sons (2001).

[29] V. Jović and B. Jović. Eis and differential capacitance measurements onto single crystal faces in different solutions: Part i: Ag (111) in 0.01 m nacl. *Journal of Electroanalytical Chemistry*, **541** (2003) 1.
DOI: 10.1016/S0022-0728(02)01309-8.

[30] G. C. Lica and Y. J. Tong. Electrochemical impedance spectroscopic measurement of potential of zero charge of octanethiolate-protected au and pd nanoparticles. *Journal of Electroanalytical Chemistry*, **688** (2013) 349.
DOI: 10.1016/j.jelechem.2012.10.008.

[31] D. C. Grahame. The electrical double layer and the theory of electrocapillarity. *Chemical reviews*, **41** (1947) 441.

[32] Y. Uematsu, R. R. Netz and D. J. Bonthuis. The effects of ion adsorption on the potential of zero charge and the differential capacitance of charged aqueous interfaces. *Journal of Physics: Condensed Matter*, **30** (2018) 064002.
DOI: 10.1088/1361-648X/aaa4d4.

[33] P. Ramírez, R. Andreu, Á. Cuesta, C. J. Calzado and J. J. Calvente. Determination of the potential of zero charge of au (111) modified with thiol monolayers. *Analytical chemistry*, **79** (2007) 6473.
DOI: 10.1021/ac071341z.

[34] N. Elgrishi, K. J. Rountree, B. D. McCarthy, E. S. Rountree, T. T. Eisenhart and J. L. Dempsey. A practical beginner's guide to cyclic voltammetry. *Journal of Chemical Education*, **95** (2017) 197.
DOI: 10.1021/acs.jchemed.7b00361.

[35] G. A. Mabbott. An introduction to cyclic voltammetry. *Journal of Chemical Education*, **60** (1983) 697.
DOI: 10.1021/ed060p697.

[36] C. Lakshmanan, R. N. Viswanath, S. R. Polaki and R. Rajaraman. Determination of surface area of nanoporous metals: Insights from double layer charging. AIP Publishing LLC (2015).
DOI: 10.1063/1.4918242.

[37] H. Wang and L. Pilon. Intrinsic limitations of impedance measurements in determining electric double layer capacitances. *Electrochimica Acta*, **63** (2012) 55.
DOI: 10.1016/j.electacta.2011.12.051.

[38] D. Jambrec, M. Gebala, F. La Mantia and W. Schuhmann. Potential-assisted dna immobilization as a prerequisite for fast and controlled formation of dna monolayers. *Angewandte Chemie International Edition*, **54** (2015) 15064.
DOI: 10.1002/anie.201506672.

[39] B. Ter-Ovanessian, C. Alemany-Dumont and B. Normand. Single frequency electrochemical impedance investigation of zero charge potential for different surface states of cu–ni alloys. *Journal of Applied Electrochemistry*, **44** (2014) 399.
DOI: 10.1007/s10800-013-0642-2.

[40] R. de Levie. On porous electrodes in electrolyte solutions. *Electrochimica Acta*, **8** (1963) 751.
DOI: 10.1016/0013-4686(63)80042-0.

[41] H. Keiser, K. Beccu and M. Gutjahr. Abschätzung der porenstruktur poröser elektroden aus impedanzmessungen. *Electrochimica Acta*, **21** (1976) 539.
DOI: 10.1016/0013-4686(76)85147-X.

[42] D. D. Macdonald. Reflections on the history of electrochemical impedance spectroscopy. *Electrochimica Acta*, **51** (2006) 1376.
DOI: 10.1016/j.electacta.2005.02.107.

[43] P. Brunner. Master's thesis: Nanoporous structure of dealloyed metals investigated by electrochemical impedance spectroscopy (2018).

[44] C. Smith and H. White. Voltammetry of molecular films containing acid/base groups. *Langmuir*, **9** (1993) 1.
DOI: 10.1021/la00025a001.

[45] H. S. White, J. D. Peterson, Q. Cui and K. J. Stevenson. Voltammetric measurement of interfacial acid/base reactions. *The Journal of Physical Chemistry B*, **102** (1998) 2930.
DOI: 10.1021/jp980035+.

[46] M. A. Bryant and R. M. Crooks. Determination of surface pka values of surface-confined molecules derivatized with ph-sensitive pendant groups. *Langmuir*, **9** (1993) 385.
DOI: 10.1021/la00026a005.

[47] W. R. Fawcett, M. Fedurco and Z. Kovacova. Double layer effects at molecular films containing acid/base groups. *Langmuir*, **10** (1994) 2403.
DOI: 10.1021/la00019a062.

[48] M. Smiljanić, C. Adam and T. Doneux. Electric field induced proton transfer at α, ω-mercaptoalkanecarboxylic acids self-assembled monolayers of different chain length. *Journal of electroanalytical chemistry*, **815** (2018) 238.
DOI: 10.1016/j.jelechem.2018.03.010.

[49] K. Cheng. Counterion triple layer in solid/solution interface: Stirring and temperature effects on pH measurements. *Journal of Colloid and Interface Science*, **239** (2001) 385.
DOI: 10.1006/jcis.2001.7580.

[50] H.-K. Song, Y.-H. Jung, K.-H. Lee and L. H. Dao. Electrochemical impedance spectroscopy of porous electrodes: the effect of pore size distribution. *Electrochimica Acta*, **44** (1999) 3513.
DOI: 10.1016/s0013-4686(99)00121-8.

[51] D. A. Patel, A. M. Weller, R. B. Chevalier, C. A. Karos and E. C. Landis. Ordering and defects in self-assembled monolayers on nanoporous gold. *Applied Surface Science*, **387** (2016) 503.
DOI: 10.1016/j.apsusc.2016.05.149.

[52] E. Boubour and R. B. Lennox. Potential-induced defects inn-alkanethiol self-assembled monolayers monitored by impedance spectroscopy. *The Journal of Physical Chemistry B*, **104** (2000) 9004.
DOI: 10.1021/jp000151o.

[53] E. Hengge, E.-M. Steyskal, R. Bachler, A. Dennig, B. Nidetzky and R. Würschum. Adsorption and desorption of self-assembled l-cysteine monolayers on nanoporous gold monitored by in situ resistometry. *Beilstein Journal of Nanotechnology*, **10** (2019) 2275.
DOI: 10.3762/bjnano.10.219.

[54] T. Doneux, M. Steichen, A. De Rache and C. Buess-Herman. Influence of the crystallographic orientation on the reductive desorption of self-assembled monolayers on gold electrodes. *Journal of electroanalytical chemistry*, **649** (2010) 164.
DOI: 10.1016/j.jelechem.2010.02.032.

[55] S. Wang, E. Tian and C. Lung. Surface energy of arbitrary crystal plane of bcc and fcc metals. *Journal of Physics and Chemistry of Solids*, **61** (2000) 1295.
DOI: 10.1016/S0022-3697(99)00415-1.

[56] Y. chen Karen Chen-Wiegart, S. Wang, Y. S. Chu, W. Liu, I. McNulty, P. W. Voorhees and D. C. Dunand. Structural evolution of nanoporous gold during thermal coarsening. *Acta Materialia*, **60** (2012) 4972.
DOI: 10.1016/j.actamat.2012.05.012.

[57] K. M. Dickinson, K. E. Hanson and R. A. Fredlein. Potentials of zero charge and capacitance minima of polycrystalline gold in sodium fluoride solutions. *Electrochimica acta*, **37** (1992) 139.
DOI: 10.1016/0013-4686(92)80022-E.

[58] C. Mahr, P. Kundu, A. Lackmann, D. Zanaga, K. Thiel, M. Schowalter, M. Schwan, S. Bals, A. Wittstock and A. Rosenauer. Quantitative determination of residual silver distribution in nanoporous gold and its influence on structure and catalytic performance. *Journal of catalysis*, **352** (2017) 52.
DOI: 10.1016/j.jcat.2017.05.002.

[59] J. F. Smalley, S. W. Feldberg, C. E. D. Chidsey, M. R. Linford, M. D. Newton and Y.-P. Liu. The kinetics of electron transfer through ferrocene-terminated alkanethiol monolayers on gold. *The Journal of Physical Chemistry*,

99 (1995) 13141.
DOI: 10.1021/j100035a016.

[60] J. Lipkowski, Z. Shi, A. Chen, B. Pettinger and C. Bilger. Ionic adsorption at the au(111) electrode. *Electrochimica Acta*, **43** (1998) 2875.
DOI: 10.1016/s0013-4686(98)00028-0.

[61] B. B. Blizanac, C. A. Lucas, M. E. Gallagher, M. Arenz, P. N. Ross and N. M. Marković. Anion adsorption, CO oxidation, and oxygen reduction reaction on a au(100) surface: the pH effect. *The Journal of Physical Chemistry B*, **108** (2004) 625.
DOI: 10.1021/jp036483l.

[62] Z. Kerner and T. Pajkossy. Measurement of adsorption rates of anions on au(111) electrodes by impedance spectroscopy. *Electrochimica Acta*, **47** (2002) 2055.
DOI: 10.1016/s0013-4686(02)00073-7.

[63] R. Schweiss, C. Werner and W. Knoll. Impedance spectroscopy studies of interfacial acid–base reactions of self-assembled monolayers. *Journal of Electroanalytical Chemistry*, **540** (2003) 145.
DOI: 10.1016/s0022-0728(02)01303-7.

Acknowledgment

Finally, I would like to sincerely thank all the people who contributed to the success of this thesis.

Univ.-Prof. Dr. Roland Würschum, Institute of Materials Physics, TU Graz
for giving me the opportunity to write my thesis at the Institute of Materials Physics and for the supervision of the project.

Dr. Eva-Maria Steyskal, Institute of Materials Physics, TU Graz
for the co-supervision of the thesis and for all the discussions that provided important scientific insight and understanding throughout the course of the thesis.

Dipl.-Ing. Elisabeth Hengge, Institute of Materials Physics, TU Graz
for giving me the opportunity to be a part of the very interesting research she is conducting and for the patient support and advice during my experimental work in the laboratory and with the analysis of the results.

Dipl.-Ing. Philipp Brunner, Institute of Materials Physics, TU Graz
for introducing me to electrochemical impedance spectroscopy on nanoporous samples and for his help with the analysis of the data.

My colleagues at the Institute of Materials Physics, TU Graz
for the good working environment at the institute and for all the critical remarks and insightful discussions during coffee breaks. Special thanks to Florian Brumbauer BSc. for the company and discussions in the office during many hours of literature research and data analysis.

My family and my friends
for their consistent support throughout my studies.

The work was performed in the framework of the Lead Project (LP-03) Porous Materials @ Work and the sub-project “P10: Application potentials of nanoporous metals in biocatalysis“ at the University of Technology, Graz.